University of the West of England
BRISTOL

AERODYNAMIC DESIGN OF A MULTI-POINT OPERATIONAL HIGH-SPEED INLET

BJÖRN HEINRICH BUANGA

A thesis submitted in partial fulfilment of the requirements of the University of the West of England, Bristol for the degree of Doctor of Philosophy

This research programme was carried out in collaboration with the German Aerospace Centre, Deutsches Zentrum für Luft-und Raumfahrt e. V. (DLR)

Faculty of Environment and Technology, University of the West of England, Bristol,
June 2015

Number of words: 47,823

Abstract

In air-breathing supersonic transport aircraft the efficiency of the engine inlet has a huge influence on the engine and the aircraft performance. Nowadays, variable inlet geometries allow optimised inlet geometries and by this also maximum performance at multiple Mach numbers. The downside of this approach is the high weight fraction of the variable geometry mechanics. Determining and evaluating alternative approaches in computational fluid dynamic (CFD) simulations is the intention of this research.

Discussing state-of-the-art flow control methods leads to the most promising method, shock angle increase by mass flow injection at the beginning of the compression ramp. The concept is found in the literature but no further flow investigations have been acknowledged. Effort to increase the understanding in this particular area is done in this study by CFD simulations. Firstly, a validation of the used axisymmetric-injection and extraction boundary conditions is accomplished. After that, in quasi-three-dimensional simulations a parameter sensitivity study about the injection total pressure and injection angle is performed on a two-ramp axisymmetric configuration and on NASA's Hypersonic Research Engine inlet geometry, which was extensively studied in wind tunnel experiments. With the obtained knowledge of the axisymmetric injection simulations, there follows three-dimensional analyses of the identical inlet to confirm the findings of the preliminary study. In addition, the flow control possibilities and its behaviour are investigated at a small angle of attack. Finally, this dissertation concludes with a summary of the key findings.

Concerning the results chapters, validation of the relevant boundary conditions verifies that the used flow solver, the DLR TAU-Code, ensures correct and accurate results. The validation of the extraction boundary condition shows that the CFD result differs 2 % in total pressure recovery from experimental literature data. In the injection validation, the determined mass flow rate from the simulation differs up to 4.2 % in comparison with the expected mass flow rate. In the preliminary analysis, the influence of the injection angle is analysed. It turns out that best performance can be achieved when injecting with an angle of 45° to the main flow direction. In the following studies, the influence of further injection parameters, total pressure and total density, is evaluated. The injection total pressure is identified as the main parameter influencing the shock angle. In concluding studies, it is shown that the total pressure recovery of a Mach 6 inlet in a Mach 8 freestream flow can be enhanced by 9.5 %, when injecting 0.9 % of the captured

mass flow rate at the centre-body tip, in comparison to the non-controlled case at the same Mach number.

Finally, in asymmetric flow around an inlet at a 3° angle of attack it was investigated, whether the flow control by injection can be used for performance increases. The results were indicating that the applied asymmetric injection is not leading to performance increases in the selected configurations. However, it is shown that asymmetric injection, in the chosen configuration only at the lower inlet side, influences the flow field around the complete inlet, when regarding a position considerably downstream of the injection.

Keywords: supersonic flow control, shock angle control, Hypersonic Research Engine, mass flow injection, injection validation, extraction validation.

Acknowledgments

This thesis is the result of my research during several years in the Spacecraft Department of the Institute of Aerodynamics and Flow Technology of the German Aerospace Centre (DLR), in Braunschweig, Germany. This PhD study was performed at the DLR in Germany in collaboration with the University of the West of England, Bristol.

My special thanks are devoted to my supervisor Dr. Chris Toomer for her continuous support from the first day on. When I needed support, feedback or a discussion of critical points she always found time for me. Additionally, I would like to thank my second supervisor, Prof. Cord-Christian Rossow, also head of the Institute of Aerodynamics and Flow Technology at DLR, who supported me over the whole research period.

My thanks to the heads of my department, Dr. Thino Eggers and Prof. Klaus Hannemann, who believed in me and ensured that I have suitable frame conditions for my research. Thanks to the former head of my section, Dr. José Longo. He played a key-role during the determination of the thesis topic and supported my work in the first period.

I would like to acknowledge the DLR and the University of the West of England, Bristol for offering me the research possibility, allowing this work. Special thanks to the DLR enabling me to use their high-performance cluster for my innumerable numerical simulations.

Finally, thanks to my many colleagues, to Mira, my family and friends for their support and patience during the last years.

Table of Contents

List of Tables

List of Figures

Nomenclature

Roman Symbols

Symbol	Definition	Units
A	area	m^2
a	local speed of sound	m/s
c_p	specific heat capacity at constant pressure	J/(kg·K)
c_v	specific heat capacity at constant volume	J/(kg·K)
D	drag	N
d	diameter	ft or m
E	energy	J
e	specific energy	J/kg
$\overline{\overline{F}}$	convective fluxes tensor	- - - -
F, G, H	convective fluxes tensor fractions	- - - -
H	enthalpy	J
h	specific enthalpy	J/kg
$\vec{\imath}_x, \vec{\imath}_y, \vec{\imath}_z$	Cartesian unit vectors	- - - -
t	time	s
ID	inlet design	- - - -
k	heat conductivity	W/(m·K)
L	lift	N
M	Mach number	- - - -
$\dot{m}$	mass flow rate	kg/s
m	mass	kg
$\vec{n}$	normal vector	- - - -
p	pressure	Pa
$\overline{p}$	mass weighted average pressure	Pa
P_i	cell vertex	- - - -
Pr	Prandtl number	- - - -
Q	sonic flow coefficient	- - - -
$\dot{Q}$	heat flow rate	W
q	dynamic pressure	Pa
$\dot{q}_R$	specific radiation component	W/kg

$\dot{q}_F$	specific heat flow component	W/kg
R	specific gas constant	J/(kg·K)
Re	Reynolds number	- - - -
S	function of the freestream temperature	- - - -
T	temperature	K
t	time	s
u^+	dimensionless velocity	- - - -
u, v, w	velocity components in Cartesian coordinate system	- - - -
V	volume	m³
v	velocity	m/s
W_x	weight	N
$\dot{W}$	power	W
$\overrightarrow{W}$	conservative variable	- - - -
x, y, z	Cartesian coordinate direction	- - - -
y^+	dimensionless wall distance	- - - -

Greek Symbols

Greek Symbol	Definition	Units
α	angle of attack	°
β	shock wave angle measured from upstream flow direction	°
γ	ratio of specific heats	- - - -
Δ	distortion/change	- - - -
δ	boundary layer thickness	m
ζ	wall roughness coefficient	- - - -
η	total pressure recovery	- - - -
θ	flow deflection angle/half-cone angle	°
κ_K	Karman constant	- - - -
λ	material heat conductivity	K m/W
μ	dynamic viscosity	Pa·s
ρ	density	kg/m³
σ	deviation	- - - -
τ	shear stress	Pa
Φ	performance number	- - - -
Ω	geometric boundary of domain or cell	- - - -

Sub- and Superscripts

Script	Definition	Script	Definition
$\perp$	perpendicular case	**L**	lift
0	freestream condition	**max**	maximum
capt	captured	**min**	minimum
CC	combustion chamber	**out**	outflow
D	drag	**plen**	plenum conditions
e	energy	**ref**	reference
extr	extraction	**t**	total condition
i	inviscid	**theo**	theoretical
inj	injection	**v**	viscid
int	internal	**w**	wall

Acronyms and Abbreviations

Abbreviation	Definition
AIAA	American Institute of Aeronautics and Astronautics
AoA	angle of attack
ATTLAS	Aerodynamic and Thermal Load Interactions with Lightweight Advanced Materials for High Speed Flight
CFD	computational fluid dynamics
CFL	Courant-Friedrichs-Lewy
CPU	central processing unit of a computer
DARPA	Defense Advanced Research Projects Agency
DLR	Deutsches Zentrum für Luft- und Raumfahrt, German Aerospace Centre
DNS	Direct Numerical Simulation
EADS	European Aeronautic Defence and Space Company
ESA	European Space Agency
FVM	finite-volume method
HRE	Hypersonic Research Engine
inj	injected
ID	inlet design
JAXA	Japanese Space Agency
L/d	length-to-diameter ratio

LAPCAT	Long Term Advanced Propulsion Concepts and Technologies research programme
LES	Large Eddy Simulation
MHD	magneto-hydrodynamics
n/a	not applicable
nr.	number
NASA	National Aeronautics and Space Administration
RANS	Reynolds Averaged Navier-Stokes equations
RS	reattachment shock
SS	separation bubble
SST	Shear Stress Transport turbulence model
TAU	Triangular Adaptive Upwind (DLR-TAU-Code)
TPR	total pressure recovery
UK	United Kingdom
ZEHST	Zero Emission High Supersonic Transport

1 Research Objectives of this Investigation

The motivation for this research is the search for improvement possibilities in the usage of supersonic inlet flow control methods. From this motivation, the following research objectives can be formulated for the literature survey and the following research efforts:

- Identification and evaluation of traditional and other promising flow control methods in the literature to enhance the performance of supersonic inlet flow.

- Extensive numerical investigation and evaluation of the most promising flow control methods identified in the literature review that offer the widest Mach number range in which the control methods are effective.

- Evaluation of the numerical approach to establish a reliable and accurate numerical aerodynamic simulation for this problem.

2 Introduction

Supersonic flight is attractive. Not only big aerospace companies like EADS (2011) are regularly proposing new high-speed aircraft concepts, also the European Union is financially supporting in the Seventh Framework several European super- and hypersonic fundamental research projects like the Mach 6 “Aerodynamic and Thermal Load Interactions with Lightweight Advanced Materials for High Speed Flight II (ATTLAS)” and the Mach 8 “Long Term Advanced Propulsion Concepts and Technologies II (LAPCAT)” research programme series.

The market potential for supersonic transport aircraft is clearly proven by Liebhardt et al. (2011) who show that even though the demand for large capacity passenger supersonic aircraft is not existing yet; small supersonic transport aircraft with roughly 20 passengers are cost-efficient.

The only civil supersonic transport aircraft in service until 2003 was Concorde. Multiple reasons led to its retirement, whereas its aerodynamic performance played a key role in Concorde’s general not cost-efficient operation (Candel, 2004). Due to its high Mach number range covered in its trajectory, the design presented a trade-off between the subsonic but also the supersonic optimum geometry. When determining the global performance of an aircraft the inlet performance has a major influence on it. Ran and Mavris (2005) and Bräunling (2009) identified the importance of high engine inlet performance as one of the most efficient ways to increase supersonic aircraft performance. As this research study is concentrating on the improvement of supersonic transport systems, the focus is lying on performance enhancements of supersonic engine inlets.

To achieve a high performance, a supersonic or hypersonic inlet has to work efficiently over a range of Mach numbers. An optimised inlet performance for cruise has a high importance, when the cruise duration is appropriately long. However, during the long acceleration phase in civil transport applications, high performance is important at ideally every trajectory point to ensure cost efficient service. Variable inlet geometry is ensuring that the maximum air mass flow is captured and efficiently compressed by the use of translating centre-bodies or variable ramps over various Mach numbers. On the one hand, the variable geometry is increasing the aircraft’s performance. On the other hand, the integration of variable geometry into an inlet is significantly increasing the inlet complexity, its weight fraction and the maintainability effort (Haws et al., 2001).

Amongst other things, variable geometry is controlling the compression shock position, whereas the shock generated at the compression ramp or cone impinges ideally onto the cowl lip. This position is ensuring maximum captured mass flow and minimum adverse pressure gradient effects. To avoid using variable inlet geometry, studies were performed by Tan et al. (2007) and Haws et al. (2001) analysing possible alternative shock control methods in supersonic inlets.

In the most promising method, mass flow from the inlet's inner compression section is led to the inlet tip where it is injected into the flow field. This injection leads to an increase of the boundary layer displacement thickness (compared to the no-injection case), which increases the shock angle. Thus, the flight Mach number can be increased above the Mach number the inlet is designed for, while the shock is maintained through injection at its optimum position. This avoids boundary layer separations at the inlet's inner cowl wall and hence improves the inlet's performance. Thus, when integrating this injection technology into the fixed inlet geometry, higher freestream Mach numbers than the design Mach numbers are possible without the incorporation of variable geometry.

In this research study, flow simulations are performed with the computational fluid dynamics (CFD) flow solver TAU-Code, developed from the German Aerospace Centre, Deutsches Zentrum für Luft- und Raumfahrt (DLR).

The described circumstances lead to this research, with the aim to evaluate possible alternative inlet flow control mechanisms, which avoid the application of variable geometry.

In Chapter 3, a literature survey is presented on supersonic aerodynamics, supersonic engines, their inlets, state-of-the-art and alternative flow control methods. Following on in Chapter 4, the numerical background and the validation of the applied numerical methods are discussed. In Chapter 5, the influence of injection onto the flow field of a generic ramp configuration is investigated in detail, determining the influence of the injection parameters, total pressure and total density. In Chapter 6, the obtained knowledge is applied to the same two-dimensional simulation of an axisymmetric ramjet inlet geometry, investigated in an extensive wind tunnel study at NASA. Additionally, the influence of the injection angle is evaluated. In Chapter 7, the identical inlet is investigated three-dimensionally to confirm the two-dimensional calculations and to perform a sensitivity study around the previously determined optimum injection settings. Up to this point, all previous studies of injection flows used a symmetric arrangement. However, since axisymmetric inlets are very sensitive to angles of attack, a final study is performed in Section 7.2, determining the application of injection to control the shock angles around the inlet with

asymmetric injection. Finally, in Chapter 8, conclusions are drawn and recommendations for further work are given.

Besides the comprehensive literature survey and the extensive validation of the extraction and the injection boundary condition, a research novelty in this thesis is the detailed analysis of the shock angle increasing principle through mass flow injection. Additional to that, this research study is the first publication in which asymmetric shock angle increase through asymmetric injection is investigated which, in the investigated configuration, is not leading to performance increases.

3 Literature Survey

This literature survey starts with an overview on ramjet engines, which are discussed here in detail, including an overview about the history of ramjet propulsion and technology. There follows a detailed analysis of supersonic inlets and of flow control methods, leading to a discussion about the direction this flow control research study will take.

3.1 Ramjets

3.1.1 Introduction

Ramjet engines are simple types of jet engines. A ramjet consists of three main parts: the air inlet, combustion chamber and nozzle, as depicted in Fig. 3.1.

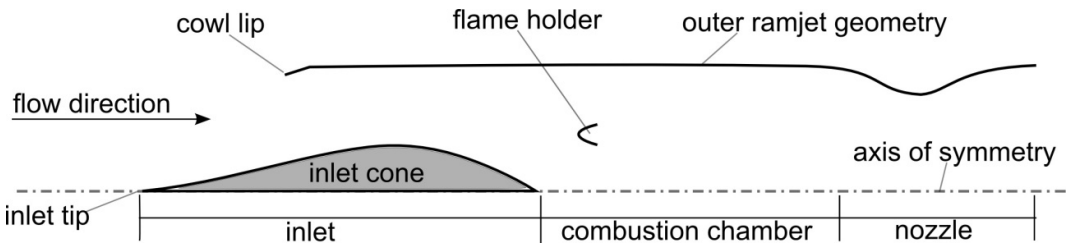

Fig. 3.1: Sketch of a typical axisymmetric ramjet engine

For its operation, no moving parts are necessary, therefore, maintenance costs are low and it has high durability in aircraft applications. Ramjet engines are air-breathing, which means that they use the atmospheric air for their combustion process, like conventional engines such as the Otto-cycle or the turbofan engine. Ramjets have usually a minimum specific impulse of about 1,700 s at Mach numbers between 2 and 6. This is significant higher than the specific impulse of liquid rocket engines (Space Shuttle main engine has 450 s in vacuum) (Wang et al., 2008; Falempin and Kuentzmann, 2009).

For the assessment of engine efficiency, the performance term *specific impulse* is often used as it allows comparing different types and sizes of engines with each other at a given operating speed. The specific impulse is given in newton times seconds per kilogram $\left(\frac{N\,s}{kg}\right)$ and represents the produced thrust per propellant mass. The higher the specific impulse, the better the performance in terms of fuel efficiency, which is crucial in aeronautical civil transport high speed applications. A typical specific impulse for a solid rocket is 250 s. This value is relatively low when compared to air breathing engines, as rockets are carrying besides their fuel also the needed oxidiser on-board. Scramjets usually have a specific impulse of approximately 1,000 s, a ramjet of around 1,700 s,

turbofans with active afterburner 3,000 s (Concorde main engine) and turbofans of about 6,000 s (B747). (Candel, 2004; Fry, 2004).

As ramjet engines use a fixed geometry to compress and decelerate the air for combustion process preparation (e.g. from supersonic freestream velocities to low subsonic speeds of about Mach 0.3), it is not possible to perform a start from a standing position with a ramjet as the sole propulsion system. The minimum velocity from which a ramjet can operate efficiently as the single propulsion system is between Mach 2 to Mach 3. Below that speed, the static pressure within the subsonic combustion chamber is too low for combustion operation. Due to this restriction, ramjet propelled vehicles need another propulsion system to reach their operational velocity. However, for operational speeds greater than Mach 6, ramjets, in which the combustion is happening at subsonic speeds, become inefficient as the value of the stagnation pressure rises, and the mechanical and thermal loads in the combustion chamber exceed the material limit (Fry, 2004; Cain, 2010).

If higher speeds are necessary, supersonic combustion ramjet (i.e. scramjet) engines can be used. In scramjets, the hypersonic freestream flow is not slowed down to subsonic conditions, but to low supersonic conditions. The geometry can also be fixed and the air temperature within scramjets is high enough to ignite the injected fuel thermally, whereas in ramjets flame holders are necessary. Due to the high flow velocity in scramjets, the mixing and combustion process has to take place in a few milliseconds before the flow leaves the combustion chamber and enters the nozzle for expansion and thrust production. Therefore, the combustion chamber and especially the fuel injector design are very critical and affect the complete scramjet efficiency (Falempin and Kuentzmann, 2009).

3.1.2 Inlet

The following chapter gives an overview about the inlet's purpose and function in ramjet engines. As this research study is mainly concerned with the inlet, a more detailed discussion is given in Section 3.2.

In a ramjet engine, the supersonic inlet consists of a supersonic diffuser (in the literature often also named supersonic compressor), a throat section and a subsonic diffuser as depicted in Fig. 3.2.

Supersonic Diffuser

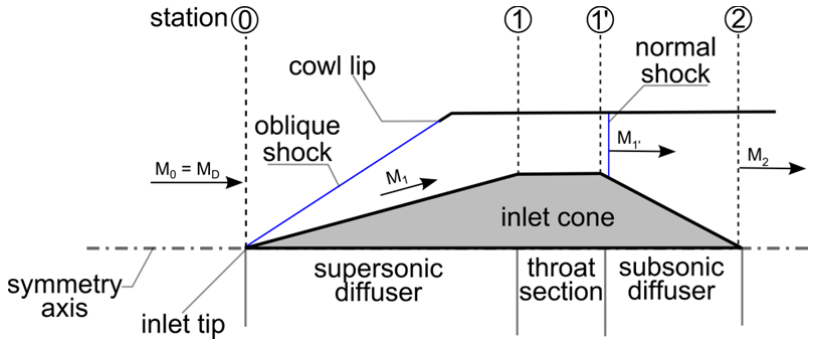

Fig. 3.2: Simplified sketch of a typical ramjet inlet at design Mach number, without depicted expansions and shock reflections. The inlet is comprised of 3 parts: a supersonic diffuser section between positions 0 and 1; between positions 1 and 1' is the throat section, finally a subsonic diffuser starts at position 1' and ends at position 2 where the combustion chamber begins (after Mahoney, 1990)) – From Inlets for Supersonic Missiles, J.J. Mahoney, 1990; reprinted by permission of the American Institute of Aeronautics and Astronautics, Inc.

In a ramjet, the supersonic diffuser has the first contact with the incoming air. The supersonic diffuser is part of the inlet. It compresses and decelerates the incoming freestream air (labelled in Fig. 3.2 as M_0) with compression ramps by a series of oblique and one final normal shock behind which the air velocity is lower than the speed of sound (M_1 upstream of the normal shock to $M_{1'}$ downstream of the shock). In the subsonic diffuser, the flow is slowed down and expanded further, to reach the required combustion chamber inflow conditions (M_2).

At vehicle speeds higher than the speed of sound, a shock wave is created at the tip of the inlet. The angle of the shock wave is dependent on the vehicle's Mach number and the surface geometry angles relative to the inflowing air. To achieve the highest possible performance of the inlet, all externally created shocks, not only the tip created one, should impinge on a predefined point on the geometry. On axisymmetric inlets, this point is usually the cowl lip, which is the tip of the ramjet's outer geometry. Normally this is the case at the cruise design Mach number as in this condition, particularly in civil applications, the aircraft usually spends the longest time flying. At all other speeds, the shock wave misses that point.

For freestream Mach numbers lower than the cruise Mach number, as depicted in Fig. 3.3, the shock wave proceeds upstream of the cowl lip and a large amount of already compressed air mass flow is lost to the atmosphere, which is understood as spillage drag.

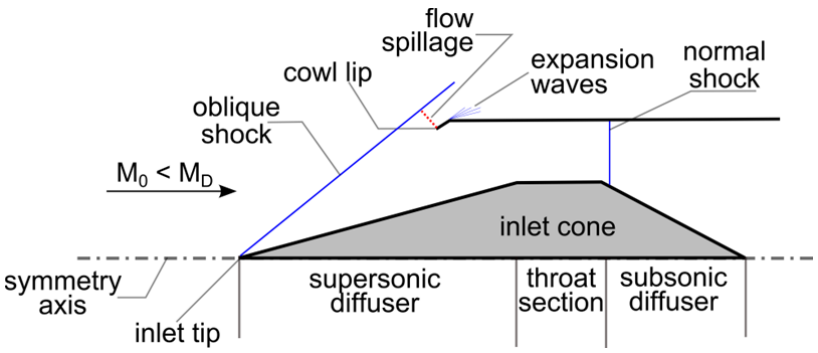

Fig. 3.3: Simplified sketch of a ramjet inlet at a speed lower than the design Mach number

At higher freestream Mach numbers than the design Mach number, shown in Fig. 3.4, the shock wave misses that point downstream and is reflected within the inlet causing a loss of total pressure, due to a rise of the stagnation pressure. Additional to the stagnation pressure rise, the impinging shock at the inside of the inlet can cause a boundary layer separation that can alter the inlet flow significantly, up to a choking of the inlet (Nagashima, 2007; Ran and Mavris, 2005). When the oblique compression shock from the inlet tip misses the cowl tip to the inside of the inlet, additional drag occurs at the inlet due to the formation of an additional shock generated at the cowl tip.

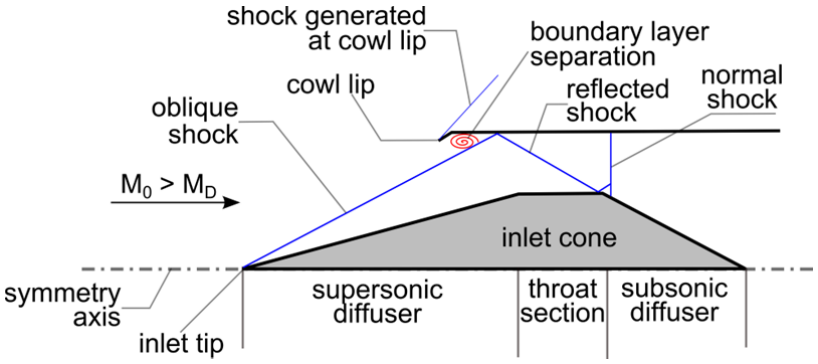

Fig. 3.4: Simplified sketch of a ramjet inlet at a speed higher than the design Mach number

Throat section

In the throat section, the flow Mach number is reduced through one normal shock from a supersonic to a subsonic Mach number. The lower the Mach number changes through the normal shock, the lower are the losses in the pressure recovery. Typically, the Mach number at the upstream side of the normal shock is about 1.2-1.3 and at the downstream side about 0.8 (Goldsmith and Seddon, 1993).

Subsonic diffuser

Downstream of the throat section is the subsonic diffuser. This has the function to slow down the air mass flow from high to low subsonic velocities and provide smooth, homogeneous airflow at the appropriate velocity and pressure values to the combustion chamber. This change is achieved

through the pressure level increases in the diffuser and this reduces the flow velocity to the required combustion chamber intake speed.

3.1.3 Combustion Chamber and Nozzle

Downstream of the subsonic diffuser, the compressed inlet air enters the combustion chamber at a Mach number of around *M=0.3.* The lower the Mach number in the combustion chamber, the higher the losses during the prior deceleration process, but then the combustion chamber can be shorter as mixing and combustion are achieved in a smaller length. Thus, the mission dependent ideal combustion chamber inflow Mach number has to be determined in a trade-off study. Fuel is injected into the airflow in the combustion chamber, or shortly upstream of it. For improved combustion efficiency, turbulence is often created to enhance the mixing of the air-fuel mixture before the mixture is ignited through flame holders, as depicted in Fig. 3.1 (Falempin and Kuentzmann, 2009; Ran and Mavris, 2005). The lower limit of the air-to-fuel ratio is that limit at which combustion is just achieved. As the airtofuel ratio is increased above the lower limit, the combustion efficiency increases. The upper limit depends strongly on the material used for lining the combustion chamber and any wall cooling mechanisms, as a rich air-to-fuel ratio leads to high wall surface temperatures and high pressure loadings.

Increasing the air-to-fuel ratio increases the pressure in the combustion chamber and the combustion chamber back-pressure, too. Making the ratio too rich causes the back-pressure to be so high that the normal shock (in section 1-1' in Fig. 3.2) moves upstream, with the potential to push the normal shock out of the inlet, which would result in an inlet choke. Such a blockage of the inlet can also be caused through a large boundary layer separation.

A Laval nozzle is downstream of the combustion chamber, at the very end of the ramjet engine. It expands and accelerates the hot out-flowing gas mixture from subsonic to supersonic speeds as it passes through the nozzle and is thereby producing thrust (Falempin and Kuentzmann, 2009).

3.1.4 History of Ramjet Technology

In the 1930s, the first ramjet testing began, although the first subsonic ramjet cycle device patent is from the year 1909 and the first scientific publication from 1913, in which the high supersonic or even hypersonic capabilities of the ramjet technology were not mentioned. In World War Two Germany built the first pulsed ramjet powered missile whose technology was later adopted by other countries. This was followed by a period of heightened ramjet research interest that peaked in the early 1960s. In 1980, international ramjet development began mainly by France and the United States of America, whereas in the 1990s many other countries, like the People's Republic

of China, Russia, South Africa, Germany and Israel, started their own missile development programmes. Both, the military and civil industry were strongly interested in ramjet technology, until the turbojet engine design showed a higher performance through lower fuel consumption in the subsonic and low supersonic speed regime. Therefore, the ramjet technology development efforts were reduced in the late 1960s, otherwise this technology would certainly be far more advanced today. The first and so far only ramjet powered aircraft in service was the American SR-71 Blackbird, from 1964 to 1998, which was equipped with a variable-geometry dual-mode turbojet-ramjet engine in which the centre spike was translated to maintain the shock-on-lip condition (see Chapter 3.3) over a Mach number range from M1.6 to M3.2 (Fry, 2004).

Until now, ramjets have mostly been used in ballistic missiles where a booster rocket accelerates the missile up to the ramjet operational velocity. At that point, no longer required rocket components, like the rocket nozzle, are jettisoned to reduce the missile weight.

The main advantage of a ramjet engine in comparison to a rocket engine is that a ramjet uses oxygen from the atmosphere for its combustion processes whereas a rocket uses on-board liquid or solid oxygen. Therefore, a ramjet has a significantly lower engine weight fraction, which is the total propulsion system weight, which includes also the propellant weight, divided by the total vehicle weight, and a lower propellant fraction for the same mission, too. This allows longer powered flights and results in a higher overall efficiency. In ramjets, thrust modulation is also possible; this is the capability, which allows controlling the thrust production of an engine for efficient acceleration and cruise flight. Ramjets also have a significantly shorter turnaround time as they can simply be refuelled and do not have to be refurnished in an expensive and laborious way like rocpropelled vehicles. Fry (2004) indicated that the application of ramjet and scramjet technology for space access has the potential to reduce the cost per kilogramme payload by a factor between 10 and 100.

For flying speeds up to Mach 6, hydrocarbon fuels are often used in ramjets due to their good cooling capability and their higher density, when compared with hydrogen fuel, which is used for even higher Mach number applications (Fry, 2004). Liquid hydrogen has a density of 67.8 kg/m³ and a heat value of 2,360 kWh/m³, whereas hydrocarbon fuel has a density of 796 kg/m³ and a heat value of 9,300 kWh/m³ (Gestis, 2013).

Hydrogen fuel offers a very high-energy content, short reaction times and even better cooling capabilities, for restraining for example the combustion chamber wall temperatures, than hydrocarbon fuel (Fry, 2004). The short reaction times are an especially important factor during

hypersonic Mach numbers as the flow velocity in the combustion chamber increases with increasing freestream Mach number. This is leading to even less time for good mixing and combustion ensuring high combustion efficiency and is increasing the demand for high-reactive fuels.

3.1.5 Different Ramjet Types

Different generic subsonic combustion ramjet types have been developed, more or less, to a high technology readiness level. The conventional ramjet has no thrust producing capabilities from a standing position. However, several ramjet types are able to produce static thrust.

In one type, a rocket booster has been attached to a conventional ramjet – i.e. in a tandem arrangement (Fry, 2004). The booster provides the static and low-speed thrust up to the ramjet operational speed, at which point the ramjet can be activated. However, in most modern missiles, the integral rocket-ramjet type is used where the rocket propellant is stored in the ramjet combustion chamber. This enables a lower take-off weight and a smaller vehicle size can be achieved. The conventional and the integral ramjet can be liquid- or solid-fuelled, whereas the conventional ramjet system can also be gaseous-fuelled as well. The different conditions of aggregation of the fuel have an impact on the usability and the complexity of the ramjet combustion cycle. The thrust of a solid-fuelled ramjet can only be minimally controlled after ignition in the rocket mode by lowering the combustion chamber pressure. This leads to a significantly lower specific impulse and hence a lower performance. Therefore, solid fuel is only used in ramjets when there are few variations in the acceleration phase until the solid fuel is burnt and the ramjet engine continues the propulsion. This makes the solid-fuelled integral ramjet technology useful for military applications but not for civil transport applications. This is because the usage of solid fuel does not satisfy the safety requirements as emergency shut-off and thrust regulation capabilities are not available. In applications where the ramjet engine system has to comply with a high level of safety and controllability requirements, either a liquid-fuelled integral, or gaseous-fuelled ramjet system is chosen due to their significantly higher performance in comparison with the remaining ramjet types. This is true, even when considering the higher weight fraction of the fuel system, as tanks are required in liquid and gaseous fuelled ramjets. These tanks can also be used in pure ramjet mode but add additional weight due to their larger size.

Another type of a ramjet engine is the air-ducted rocket. In it, fuel-rich gas, produced from a gas generator, is mixed and burnt with compressed ram-air from the inlet. The high gas outflow velocities in the gas generator improve the flow mixing and therefore the total pressure recovery,

a value indicating the compression efficiency (see Section 3.2), and this assures full control of the resulting throttle. Besides the rocket-boosted ramjet, other hybrid technologies are also used to provide static and low-speed thrust. A turbojet engine can be integrated into the ramjet within a secondary flow path that can be closed during the transition to ramjet operation as shown in Fig. 3.5, in which the rotating geometry is used to control the mass flow rate entering the turbojet, or the ramjet flow path.

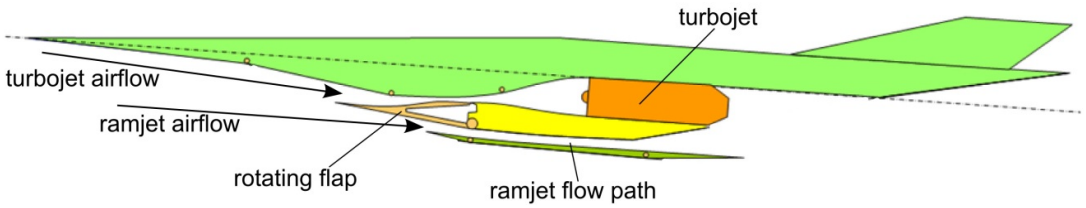

Fig. 3.5: Dual flow channel turbojet/ramjet powered aircraft (Saunders et al., 2008)

A promising concept is the air-turbo-rocket technology in which a gas generator drives a turbine. The turbine drives a compressor allowing combustion and thrust production even in a standing. The ejector ramjet only needs the integration of a gas generator or rocket motor that produces usually fuel-rich high-pressure supersonic flow, leading to thrust generation at standing position, due to secondary airflow through the engine (Waltrup et al., 1997; Fry, 2004).

As detailed literature is not available about most of the presented dual-mode ramjet technologies, a rating about their technology readiness level is not possible. However, in civil transport applications within the atmosphere, the dual flow channel principle seems promising, as it is favoured in the European LAPCAT II project. (Dittrich, 2010).

3.2 Supersonic Inlets

According to Ran and Mavris (2005), the engine's air inlet is seen as the most critical part of a ramjet engine as it should work efficiently over the whole trajectory. The quality of the airflow, in terms of turbulence and flow distortion, affects the performance of the whole engine; as 1 % in total pressure loss leads to at least 1 % loss in thrust. This opinion is also supported by Bräunling (2009) who has indicated that a 1 % loss in inlet efficiency at take-off leads to a loss of about 5 % in the payload capacity of an aircraft.

The total pressure recovery (TPR) η of the inlet is defined as the ratio of the total pressure of the airflow at the combustion chamber entrance plane ($p_{t,CC}$) to the total pressure of the freestream air ($p_{t,0}$) as described by Eq. 3.1.

$$TPR = \eta = \frac{p_{t,CC}}{p_{t,0}} \qquad \textbf{Eq. 3.1}$$

Through losses during compression, the total pressure at the inlet exit is lower than in the freestream. The lower the losses are, the higher is the value of the TPR, and the more efficient is the inlet. The maximum possible total pressure recovery is 1.

The values given mostly in the literature for the total pressure recovery (TPR), described by Eq. 3.1, do not take any friction losses between the airflow and the boundary layer and disturbances into account. Therefore, the values from literature represent the theoretically possible maximum pressure recovery, which only includes the pressure losses due to compression shocks (Wang et al., 2008).

Fig. 3.6 shows typical values for the inlet total pressure recovery against the freestream Mach number. It is also taking into account the usually occurring losses, which lead, for example at a Mach number of 2, to an overall total pressure recovery of about 0.91, highlighted in Fig. 3.6. In that figure, the total pressure recovery is shown against the freestream Mach number. The solid lines represent different TPR developments over the Mach number due to considered losses; these are in this case the "shock loss", the "duct loss" and the "extra to shock loss". Without any losses, the TPR would always be 1, but with increased number of the regarded loss types the TPR is reduced. The lowest solid line represents the TPR over the Mach number where all losses are considered. When incorporating boundary layer bleed into the inlet the losses can be reduced and the TPR is increased, highlighted in Fig. 3.6 through the dashed line.

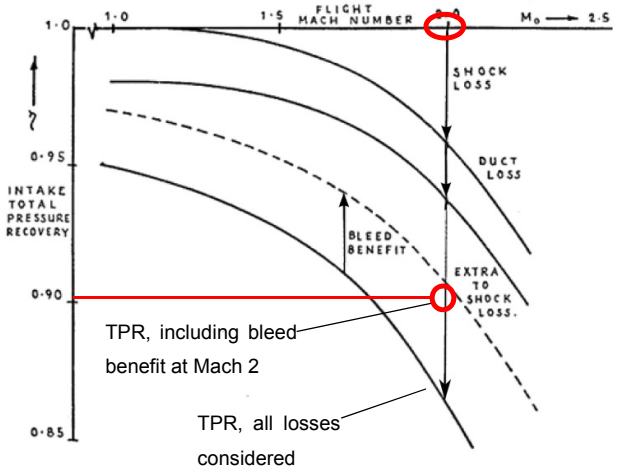

Fig. 3.6: Typical total pressure recovery vs. flight Mach number in supersonic intakes, adapted (Hermann, 1956)

It is possible to generalise that the losses increase with increasing freestream Mach number, which leads to lower recovery ratio values. The indicated "extra to shock loss" region, in Fig. 3.6, results from viscous effects and non-uniform flow arriving at the combustion chamber entrance. As seen at lower Mach numbers, the losses can be reduced through the incorporation of boundary layer bleed into the inlet, which reduces the boundary layer height at the separation and improves the flow stability within the inlet (Hermann, 1956).

Design of the Supersonic Diffuser

During the design of a supersonic intake, many factors have a major influence on the overall design and the final performance. Many design trade-offs need to be made, beginning with the general shapes of the supersonic and subsonic diffusers. Three geometries are common: the axisymmetric (annular) inlet, the quasi-two-dimensional and the three-dimensional compression rectangular inlet geometries.

The main differences in the flow topologies occur in the subsonic diffusers due to the different external and internal shapes. The axisymmetric subsonic diffuser geometry leads to a higher pressure recovery than with a rectangular geometry but only when the incoming flow is in line with the inlet's centrebody axis. At any other incoming flow angle the developing flow distortion causes performance losses due the formation of boundary layer separations leading to a reduction in the mass flow rate.

On the other hand, the rectangular topology is clearly less sensitive to non-symmetric flow. Rectangular inlets are also less sensitive to other sources of flow distortion and are also less complex to design (Ran and Mavris, 2005). The main difference between two- and three-dimensional inlets is the geometry section in which the compression of the air mass flow takes place.

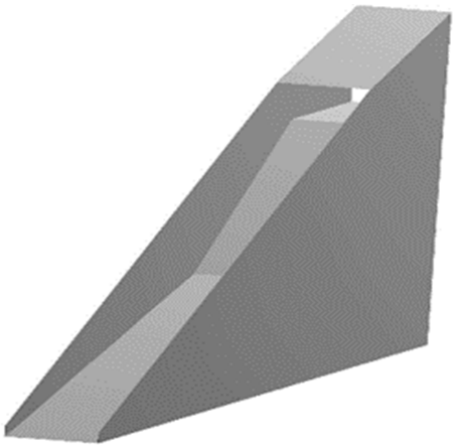

Fig. 3.7: Quasi-2D inlet with side walls (Krause and Ballmann, 2007)- - Springer, p. 589, fig. 1, with kind permission from Springer Science and Business Media

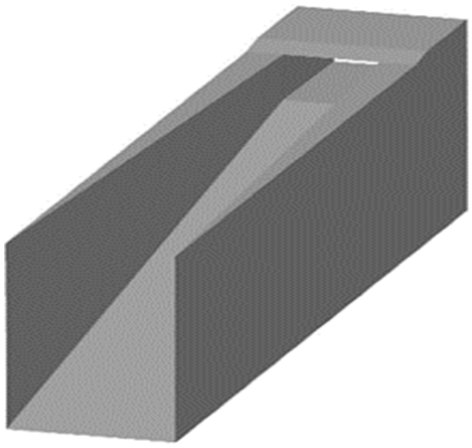

Fig. 3.8: 3D inlet with converging side walls (Krause and Ballmann, 2007) - - Springer, p. 589, fig. 1, with kind permission from Springer Science and Business Media

To clarify this, it is possible to simplify rectangular subsonic diffusers, so that in two-dimensional inlets only the distance between the upper and lower walls decreases with increasing downstream position, as pictured in Fig. 3.7 whilst the side walls run parallel to each other, thus one can say that compression is effected in one direction (Krause and Ballmann, 2007).

As shown in Fig. 3.8, in three-dimensional compression inlets the sidewalls are converging too, thus the flow is compressed in two directions.

Three-dimensional inlets lead to a higher degree of flow complexity but can also achieve higher performance than two-dimensional inlets. However, in terms of the design process, two-dimensional inlets are preferred as the lower flow complexity and their nearly identical flow properties over the full inlet span, at any angle of attack, allow a simpler and faster design process with shorter design cycles (Bräunling, 2009).

Depending on the inlet geometry and its integration into the aircraft, the inlet produces up to 40 % of the vehicle's overall lift, when assuming a large size rectangular inlet at which the aircraft's fore-body acts as compression ramp, but therefore, it could also cause a high drag. Due to its potential large size, its weight fraction must be duly considered during design. These factors show that the ramjet inlet has a high influence on the overall vehicle performance. Therefore, its design and optimisation are one of the key points during vehicle development and design. Axisymmetric inlets lead normally not to a significant increase in the lift compared to a rectangular inlet (Falempin, 2009).

Downstream of the supersonic diffuser follows the throat section, in which a normal shock is positioned to reduce the flow Mach number from supersonic to subsonic. The normal shock wave position in ramjets depends on multiple factors like the flight speed, the captured air mass flow rate, the back-pressure from the combustion chamber, the inflowing boundary layer and also on the flow distortion. Its position can be controlled through boundary layer bleed at the intended normal shock position and through the regulation of the back-pressure acting from the combustion chamber towards the inlet throat (Fry, 2004).

Design of the subsonic diffuser

Wang et al. (2008) numerically simulated with inviscid walls in four different subsonic diffuser geometries depicted in Fig. 3.9, where the "equal pressure gradient" diffuser led to the highest total pressure recovery at one chosen Mach number and the smoothest flow, in comparison with the "equal area ratio", "equal divergence angle" and the "equal Mach number" diffuser geometries. In the equal area ratio diffuser, the area is increased at a constant rate between stations I and II, highlighted in the individual diffuser plots. In the equal Mach number diffuser, the Mach number is constantly reduced and in the equal pressure gradient diffuser, the pressure is constantly reduced between station I and II.

Wang et al. (2008) found that the equal pressure gradient diffuser gave the best total pressure recovery, and this agrees well with the findings of Oswatitsch (1947) who stated that for highest total pressure recovery in a supersonic diffuser all shock waves created at the inlet compression ramps and the final normal shock wave should be equal in strength. This shows that for maximum performance it is important that the compression happens in subsonic and supersonic flow, while ensuring equal pressure gradients.

In Section 3.3.3 a closer look at a selection of existent and to some extent flown supersonic inlets is given.

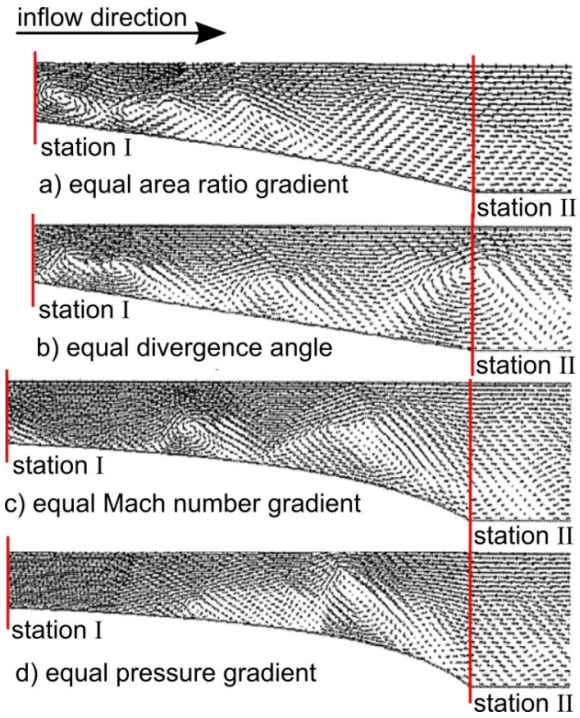

Fig. 3.9: Four subsonic diffuser geometries with velocity vectors (adopted from Hermann, 1956)

3.2.1 Compression Methods

In Figure 3.10, different compression approaches at different types of inlets are shown. The compression and reduction of the flow velocity in the inlet can be effected through applying one of various approaches during the design phase for the inlet. It has to be decided if compression is performed by only one external normal shock, which is the full external compression method, or by a series of oblique and then one final normal shock denoted as the full internal or mixed compression methods. Each of the compression methods has its advantages and disadvantages depending on the freestream velocity so that there exists a proper type for every Mach number range.

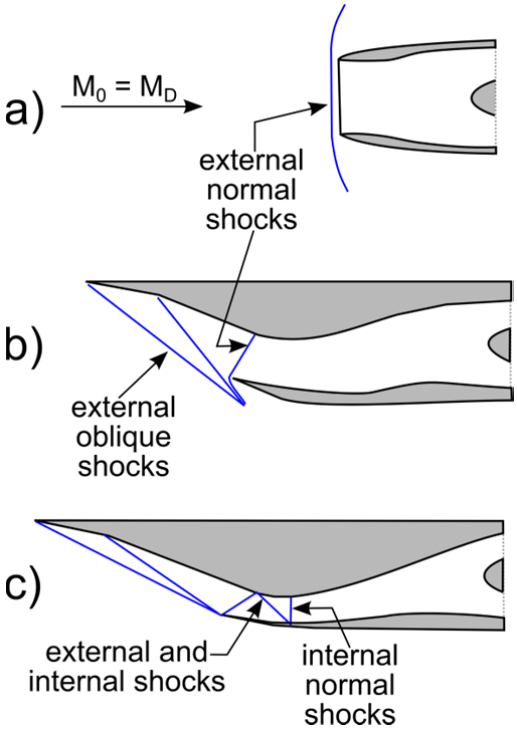

Fig. 3.10: Different compression approaches in different inlet types (simplified after Mahoney, 1990) - From Inlets for Supersonic Missiles, J.J. Mahoney, 1990; reprinted by permission of the American Institute of Aeronautics and Astronautics, Inc.

1. Single Normal Shock External Compression (Fig. 3.10a)

In principle it is possible to slow down the flow with only one strong normal shock in front of the inlet from a high supersonic to a subsonic Mach number. However, this method leads to high pressure losses making it very inefficient. One sole normal shock in front of the inlet would lead to a maximum total pressure recovery of no more than 0.32, depending on the freestream Mach number.

2. Multiple Shock External Compression (Fig. 3.10b)

In contrast to a single normal shock wave, the use of multiple shock external compression is often preferred. It offers better performance and guarantees the identical good starting and reliable operation characteristics of the inlet as for the single normal shock external inlet. This multiple shock external compression approach is also used when designing a supersonic wind tunnel (Hermann, 1956; Anderson, 2004). During the external compression, the resulting shocks, externally generated at the compression ramps, should focus on the cowl lip. Otherwise a boundary layer separation could occur - if not avoided by flow control methods. With increasing Mach number, a higher degree of compression is required to slow down the incoming air to the required properties for combustion. A higher degree of compression results with increased total flow turning angle, and it is leading to lower total pressure recoveries. Therefore, pure external compression becomes inefficient above a Mach number of about 2.5 as the cowl angle and cowl drag increase significantly.

3. Mixed Compression inlets (Fig. 3.10c)

At Mach numbers higher than $M=2.5$ mixed compression inlets should be used as they offer better performance in terms of the total pressure recovery, as shown in Fig. 3.10c. Not depicted is a variable geometry mixed compression inlet which allows possible performance gain due to an adopted inlet geometry fitting to the inflow Mach number and the flow topology . Mixed compression inlets complicate the inlet geometry design and weaken their operational stability as an inlet-starting problem can arise, i.e. the inlet can “choke”. In a choked inlet, a large amount of mass flow (which would ideally go through the engine in normal operation) is not able to enter the inlet. Inlet choking problems are important as the consequential flow distortions within the initial parts of the engine are caused by the current approaching air mass flow being too big to pass into the smallest section of the inlet, which is (most of the times) the geometric throat. However, in practical terms the aerodynamic throat can also be at any other position due to flow-channel size-reductions because of boundary layer separations. The engine starting capability depends mostly on the degree of the internal compression and the flow-turning angle, as described by Hermann (1956). With increasing degree of internal compression, the air inlet

becomes longer and heavier but with a decrease of the produced external drag at the same time. At higher angles of attack, the internal compression inlets tend to a higher level of flow distortion resulting from viscosity effects, mainly separated boundary layers due to shock/boundary layer interactions.

Assessing advantages and disadvantages, mixed compression is mostly used for high Mach number applications, because it offers for these cases the best trade-off between high total pressure recovery and low drag. External and mixed compression inlets have a much better performance at supersonic freestream speeds, but a significantly worse one at subsonic freestream speeds, than an inlet with only one normal shock wave in front of the inlet. Therefore, the choice of the inlet geometry depends strongly on the flight trajectory and the vehicle's purpose (Mattingly, 1996). This was seen in exactly the same manner in the recent extensive *M=6* European vehicle study in the ATLLAS project ("Aerodynamic and Thermal Load Interactions with Lightweight Advanced Materials for High Speed Flight"). There was a mixed compression inlet with three external, one internal and a final normal internal shock chosen, as it offered a good trade-off between high subsonic efficiency and low cowl drag for the long Mach 6 cruise velocity trajectory. In ATTLAS project, only fully turbulent CFD simulations were performed using finite volume Reynolds averaged Navier-Stokes equations and the Shear Stress Transport turbulence model to determine the flow behaviour (Dittrich, 2010).

It is possible to relate the number of shocks with the total pressure recovery. The higher the number of oblique shocks during compression, the higher is the total pressure recovery. This is because the inlet losses are reduced due to fewer losses arising from the (lower intensity) oblique shocks. In contrast, increasing the number of oblique shocks, lowers the flow quality (assuming no flow control methods are applied). In general, the presence of more shocks produces more viscous boundary layer effects, including larger boundary layer heights and their separation. Theoretically, at an inviscid surface, compression performed by an infinite number of weak external shocks leads to isentropic compression without any losses. In real applications, this theoretical prediction is too simplistic, as an inlet, containing infinite weak shocks, would need to be infinite in length with an infinitesimally thin leading edge (Goldsmith and Seddon, 1993).

It was mentioned in Section 3.2 that for super- and hypersonic inlets the total pressure recovery is a good performance indicator. The total pressure recovery value is the product of the individual pressure recoveries of the supersonic and subsonic diffuser and, if integrated into the inlet, of the isolator. Therefore, one common design aim of a ramjet or a scramjet inlet is the method to maximise the total pressure recovery by ensuring equal shock strengths. This method was

proposed by Oswatitsch (1947) stating that for optimised total pressure recovery the generated shocks have to be equal in their strength, in the form given in Eq. 3.2:

$$M_1 * \sin\beta_1 = M_2 * \sin\beta_2 \qquad \textbf{Eq. 3.2}$$

Where M_i is the Mach number before a shock, and

β_i is the shock wave angle measured from the upstream flow direction.

3.2.2 Inlet Working Conditions

Ramjet air inlets can work in three different conditions, defined by the normal shock position relative to the throat position (which is the smallest geometric height or area section in the inlet). If the final normal shock, which reduces the supersonic airflow to subsonic velocities, is positioned right at the throat point, the inlet is working in the critical condition. The critical condition is very sensitive to flow and pressure distortions, which are occurring due to gusts or changes in the angle of the inlet relative to the freestream flow. Nonetheless, in this condition the inlet has its maximum efficiency as the spillage of the air, which misses the intake, is at its minimum and the air mass flow and the total pressure recovery have their maximum values.

In Fig. 3.11, different normal shock positions at three operating Mach numbers are shown. In the sub-critical condition the normal shock sits upstream of the throat as the intake delivers a higher air mass flow rate than the engine can use or as the throat can pass. In this condition, mass flow spillage through the inlet opening increases, resulting in pressure losses and spillage drag.

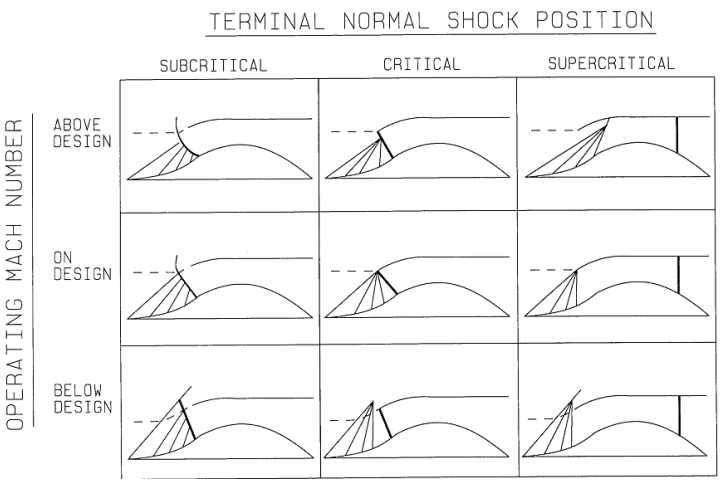

Fig. 3.11: Different normal shock positions in a ramjet inlet (Mahoney, 1990) - From Inlets for Supersonic Missiles, J.J. Mahoney, 1990; reprinted by permission of the American Institute of Aeronautics and Astronautics, Inc.

In the critical case, the shock positions itself at the throat. This is the best position for minimising losses and hence operating the engine at its greatest thrust level with minimum fuel consumption.

If the engine has a higher air mass flow demand, than the inlet delivers, the normal shock moves from the throat downstream to a position within the diverging section, called the super-critical condition. This condition leads to slightly stronger shocks and therefore, a higher pressure loss than the critical position which results in a reduced thrust level and increased fuel consumption. Therefore, the super-critical condition should be avoided, in accordance to Bräunling (2009).

However, to allow a safe and reliable inlet operation in real conditions, the normal shock should be positioned not at the throat but just downstream of the critical position. In this slightly super-critical position the final normal shock remains relatively stable, whereas a shock positioned right in the throat would leave this position when small disturbances occur. Then the shock would move upstream and block the flow. This would cause higher losses and worse problems, resulting in spillage and could result in a complete choking of the inlet. This leads to enormous pressure losses, consequently, the super-critical inlet working condition is always preferred for real cases (Hermann, 1956; Mahoney, 1990).

Another air intake problem is air inlet buzzing, described by Bräunling (2009) as a time dependent effect, with strong pressure variations within the inlet. The reason for this behaviour is caused by shock wave/boundary layer interactions in the sub-critical condition, where the normal shock sits in front of the inlet lip inducing a large boundary layer separation. This separation reduces the effective flow channel height and thus the flow velocity increases until the inlet chokes when the maximum possible mass flow rate is reached. At this condition, the normal shock moves upstream with the effect that the boundary layer separation thickness is reduced, as the existing boundary layer is smaller at the point of interaction, which increases the flow velocity. With increasing velocity, the normal shock moves again downstream closer to the inlet opening until the inlet chokes due to the bigger separation again. This process occurs periodically, multiple times per second, resulting in a characteristic buzzing noise. In experiments and with time-dependent computational fluid dynamics simulations it is possible to reproduce the oscillations with a high degree of correlation in terms of frequency and surface pressures, which includes the shock movement and its amplitude. Tan et al. (2009) found in their viscous CFD study that the oscillation frequency was in the investigated inlet up to 116 Hz at a freestream Mach number of 5. Park et al. (2011) developed further the existing standard approach into a low-order model predicting inlet buzz and its behaviour in variable-area nozzle throats. This model allowed changing the back-pressure and through this, controlling the sensitive inlet buzzing. With the purpose of avoiding both any inlet buzzing and too super-critical operation conditions, the intake shall be operated close to the critical but still in the super-critical condition.

3.2.3 Flow Phenomena occurring in Supersonic Inlets

The most dominating flow phenomena in ramjet air inlets are identified by Schulte (2001). These are compression shocks, boundary layer formation on the walls and the interaction between the boundary layer and the shock waves, which can cause, for example, boundary layer separation.

Boundary layer separation can lead to the formation of a separation bubble: a low-speed recirculation area lowering the effective aerodynamic channel height. Dujardin et al. (2001) explain the formation of the separation bubble "as the result of the combination of the adverse pressure induced by the shock and the adverse pressure induced by the wedge". In Fig. 3.12 a Schlieren image of a wind tunnel experiment of a flat plate/ramp configuration is shown, visualising the formation of a separation bubble at the ramp's foot. The freestream Mach number is 5.3, the freestream Reynolds number is 4.2 million and the ramp angle is 15°.

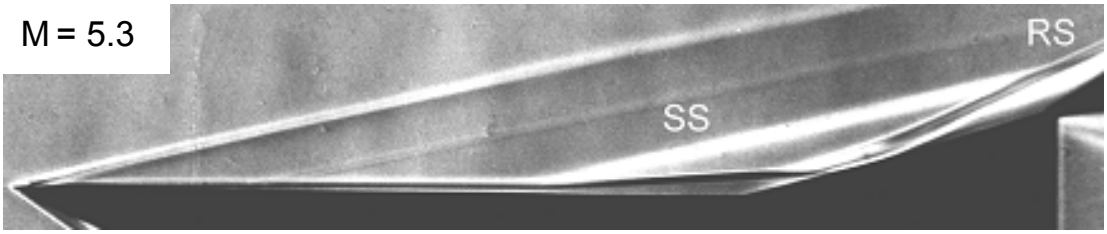

Fig. 3.12: Schlieren image of a separation bubble inducing two shocks on a flat plate-ramp configuration (Schulte, 2001)

To the incoming flow, the separation bubble acts as a ramp and an additional compression shock appears at the front of the bubble due to the existence of this separation. This separation-induced shock (SS on Fig. 3.9) is formed due to the change in the flow direction at its base point.

A second, a reattachment shock (RS on Fig. 3.9) is formed at the end of the bubble where the boundary layer reattaches to the wall surface. Without viscosity, only one oblique shock would be formed, induced by the compression wedge, right at the base point of the wedge. The formation of the additional shocks lowers the total pressure recovery. Consequently, it is unfavourable as it could also lower the air intake mass flow and could even result in a choking of the inlet with an extremely reduced mass flow rate when a substantial part of the inlet is blockedd by the separation bubble.

3.2.4 Starting Behaviour of Supersonic Inlets

The already aforementioned choking of the inlet depends strongly on the internal contraction ratio, the area ratio between the engine inlet area, measured perpendicular from the compression ramp surface to the cowl, and the area of the throat, i.e. the minimum area between the compression walls within the inlet:

$$I = 1 - \frac{A_{throat}}{A_{lip}} \qquad \textbf{Eq. 3.3}$$

with I the internal contraction ratio.

Kantrowitz formulated in 1945 an equation that should predict a safe starting of a supersonic inlet, when designed in accordance to this internal contraction ratio limit (Kantrowitz and Donaldson, 1945). To ensure a self-start of an inlet, which is un-choked supersonic flow through the inlet, the maximum internal compression, which can be understood as the maximum flow channel reduction between the lip and the throat, I_{max} , is determined with Eq. 3.4:

$$I_{max} = 1 - \left[\left[\frac{2 + (\gamma - 1)M_{lip}^2}{2\gamma M_{lip}^2 - (\gamma - 1)}\right]^{0.5}\left[\frac{2}{\gamma + 1}\left[1 + \frac{\gamma - 1}{2}\left(\frac{2 + (\gamma - 1)M_{lip}^2}{2\gamma M_{lip}^2 - (\gamma - 1)}\right)\right]\right]^{-\frac{\gamma+1}{2(\gamma-1)}}\right] \qquad \textbf{Eq. 3.4}$$

Where M_{lip} is the Mach number at the cowl lip.

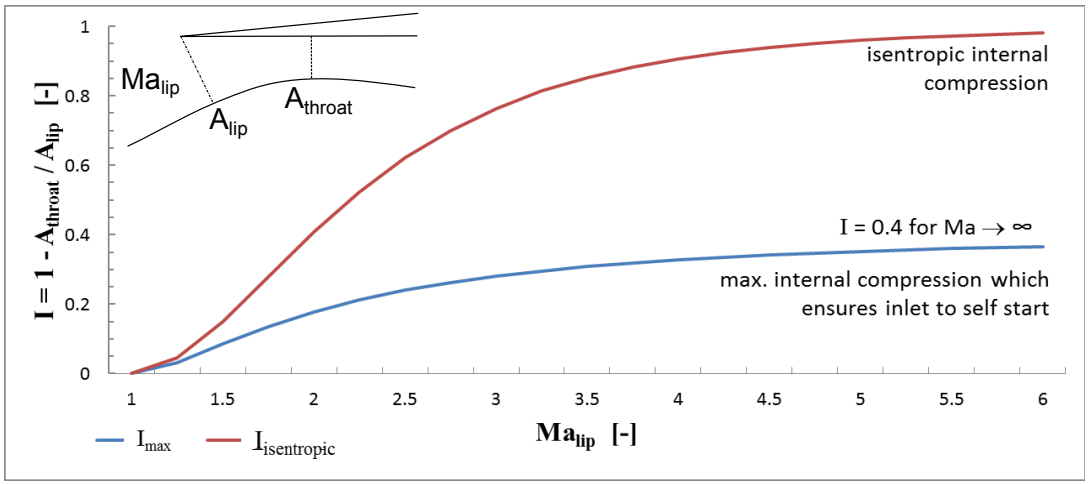

Fig. 3.13: Presentation of the inlet self-starting Kantrowitz limit (after Kantrowitz and Donaldson, 1945), showing the maximum allowed internal compression starting and the theoretical maximum isentropic compression after inlet start

In Fig. 3.13 a diagram is shown, depicting the maximum internal compression (blue line), determined by Eq. 3.4, and the isentropic internal compression (red line), Eq. 3.5, over the Mach number.

Even if the compliance of this limit allows starting of the inlet, it allows mostly only a fraction of the possible engine performance. After starting, the so called Kantrowitz-limit has no longer to be considered, as from that point on it is possible to increase the internal contraction up to the isentropic limit, $I_{max,isetropic}$, which can be determined with Eq. 3.5:

$$I_{max,isetropic} = 1 - M_{lip}\left[\frac{2}{\gamma + 1}\left(1 + \frac{\gamma - 1}{2}M_{lip}^2\right)\right]^{-\frac{\gamma+1}{2(\gamma-1)}} \qquad \textbf{Eq. 3.5}$$

Concluding, the aim of designing an air inlet is to produce an inlet geometry where the reduction of the flow velocity is achieved with the least possible pressure and mass flow losses, whilst ensuring a high compression ratio of the incoming ram-air at all operating conditions. According to Schulte (2001), the quality of an air inlet can be measured by the total pressure recovery, which should be as high as possible, and the distortion of the flow at the engine face should be as low as possible ensuring good mixing and combustion processes. In this study, the total pressure recovery ratio will be used to rate and compare the performance of the traditional with the alternative flow control method, as it best reflects the performance of the flow control methods used.

3.3 Flow Control Methods

External compression shocks do not necessarily impinge exactly on the cowl lip. This leads to spillage and losses in total pressure recovery, as most inlets work only efficiently at their design Mach number and at all other Mach numbers performance losses have to be accepted. With flow control methods like variable geometry, the inlet can have an optimal geometry at multiple speeds. However, the larger the range is in which an inlet is able to maintain shock-on-lip condition the higher is the weight of the variable-geometry system. Therefore, a trade-off between a stable working of the engine and its performance, compared to its weight and complexity has to be found. Studies published by Bowditch (1973) and Bangert et al. (1982) indicate two effects: that the airframe exerts a high influence on the efficiency of the propulsion system and that spillage drag should be reduced during subsonic overland flight. Otherwise, poor subsonic performance significantly downgrades the overall efficiency of a high Mach number cruise vehicle. The subsonic overland flight is a requirement for all civil aircraft due to noise issues produced through the sonic boom.

To improve the efficiency of the inlet, its performance and to assure stable operation (which includes the inlet start-up behaviour), the use of flow control methods becomes necessary. The interaction between shock waves and the boundary layer was examined for the first time in the mid-1940s where the influence of the interactions on the performance was shown at transonic speeds. Also in later pure supersonic flow studies, in the 1950s, flows over the same generic geometries were used, which are still in use for fundamental studies, like the flat plate, or the flat plate/flat ramp configuration. In these studies, the fundamental knowledge was built about flow control methods.

In high-speed applications, high pressure and temperature loadings are generally present in areas with strong shock wave/boundary layer interactions, which have a great impact on important design areas, like the overall vehicle design leading to larger intakes to counter possible effective flow channel reductions through low-speed separations bubbles. Especially the engine design, the thermal protection system but also other important factors like the weight and cost are affected by the effects of such interactions (Dolling, 2001).

3.3.1 Passive Flow Control

In general, it is possible to differentiate between passive and active methods. Passive methods have the capability to influence the flow just through their geometry and their positions where they are installed. They are working continuously without any control mechanisms, therefore, without any possibility of control on their influence on the flow during operation, when they are in contact to the flow. Thus, there is no opportunity for a pilot or computer algorithm to exert control. Schulte (2001) examined the following most promising passive flow control methods that are:

- Passive cavity, as sketched in Fig. 3.14, where an incoming shock wave impinges on an open cavity, compresses the air in it and loses strength by this process. At the design flow condition, the shock is then reflected from the surface of the compressed air that is in the identical height as the surrounding wall. This method can be applied as often as wished within the inlet. The most positive effect it would have is at positions close to the throat as then this would remove the separations which otherwise occur. Since flow separations degrade the flow quality at these positions the most, the cavity action is particularly beneficial. For the effective use of this method, a large volume below the cavity is necessary. However, cavity inclusion in an air inlet is hardly possible as the required volume would be too large for efficient integration into a ramjet inlet, as proven by Schulte (2001). This comes clear, when thinking about the reduction of the boundary layer separation of the inside of the usually thin cowl by this method, where the thickness of the passive cavity would be bigger than the thickness of the cowl, making an integration of this method impossible.

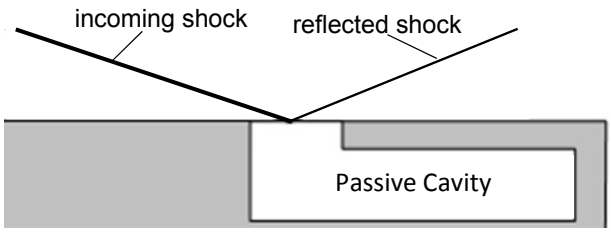

Fig. 3.14: Effects of shock impingement weakened by a passive cavity (Schulte, 2001)

- Inverse contour, where a separation bubble is formed in an extra cavity, instead of on the surface. This method is too sensitive as it works only for exactly one Mach number and produces in all off-design cases a much larger separation bubble and causes high thermal

loadings, therefore, it is not further considered as its disadvantages during off-design flight condition are too high. Thermal shape memory alloys could improve the performance at off-design flight Mach numbers, as at higher Mach numbers the surface temperature increases in an ideal case.

- Shock erasure, as shown in Fig. 3.15, where a shock impinges on the beginning of a ramp that is at the same angle as the incoming flow. Thus, there is no change in flow direction and no reflected or created shock. This method is promising as it is less sensitive than the other passive methods, as in off-condition the shock is striking onto the ramp from which it is then reflected, without great disadvantages on the flow topology. This control method is already implemented in a number of supersonic vehicles and is seen on cowl lips of ramjet inlets. For optimum erasure of the impinging shock, at every Mach number, the ramp needs to be variable in its ramp angle, otherwise the shock is not erased fully but weakened at any other incoming shock angles. Stream wise slots can be orientated in an array and are positioned under a shock wave-boundary layer interaction to weaken shocks by altering the flow structure and creating a bifurcated lambda-shock structure. This method, which is successfully used in the engine inlet of the Lockheed SR-71 Blackbird, is promising in shock weakening and fixing it at one position. However, it is not as efficient in terms of increasing the total pressure recovery as the shock erasure method (Holden and Babinsky, 2005).

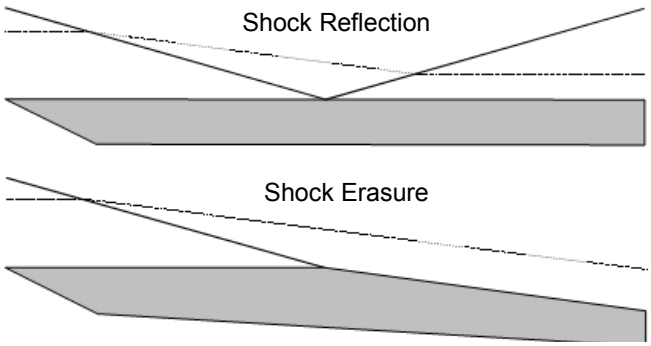

Fig. 3.15: Shock erasure principle (Schulte, 2001)

3.3.2 Active Flow Control Methods

Active methods are usually controlled by sensors or by the material itself and work in a controlled way to obtain the best possible effect over the whole trajectory. One of the most common active boundary layer control method is mass flow extraction, also known as bleed. As in this dissertation, flow control by boundary layer extraction and injection play an important role, these methods are explained in detail in the next sub-sections 3.3.2.1 and 3.3.2.2. In this sub-section, a few additional active boundary layer control methods are briefly discussed.

The development from Boeing and NASA of smart mesoflaps for aeroelastic transpiration are promising in terms of improving the aircraft performance significantly and have led to a patent of Loth et al. (2000). These flaps are only a few millimetres to ten millimetres long and are installed with one end at the leading edge of an air intake. The flaps are either flapping out through the

pressure gradient acting on them, created by a generated or incoming shock or, if manufactured out of smart materials, actively controlled by heating elements in a closed control loop. The resulting pay-off is estimated by Dolling (2001) to be around 18 % in weight and cost savings for a Mach 3.5 vehicle at an altitude of 12 km. It is also stated that the author believes the analysis is too optimistic, but even a pay-off of one half would be promising for future applications and more detailed studies.

With magneto-hydrodynamics (MHD), it is possible to control ionised flow with a generated strong magnetic field. MHD is being used to increase the distance between the aircraft surface and the bow shock and to alter shock angles. During the re-entry phase, higher distances to the bow shock lead to a lower surface heat load. Additionally, MHD allows to control the shape of shock waves, even their strength can be reduced. The downside of this method is the enormous amount of required energy, which is required for its effective application. This energy cannot be provided in an efficient way as batteries or generators with the required performance would increase the aircraft mass stronger than the MHD benefits would be (Petit et al., 2009).

3.3.2.1 *Boundary Layer Suction / Mass Flow Extraction*

Flow control through boundary layer suction is often seen as a very promising control method as it has the potential to increase the total pressure recovery, enhance the flow stability and to allow, to some extent, the stabilisation of the normal shock position near the throat. However, it also has the disadvantage that the hot compressed extracted boundary layer mass flow has to be transported away. If it is just spilled out to the atmosphere, energy is lost as energy was used to compress the air in that form and so drag was produced during compression. This loss of energy can be seen as it produces additional drag. Therefore, the already compressed, and due to the compression heated, air can be diverted from the main flow and fed direct to the nozzle where at least a portion of the total energy in the compressed air is transformed into thrust during expansion in the nozzle. However, the additional pipes linking the inlet to the nozzle cause additional weight and also increase design and operational complexity. It is also possible to use the extracted air for cooling purposes of the combustion chamber, an afterburner or the nozzle.

Since boundary layer suction has its disadvantages, it has to be the aim to take the smallest possible amount of air mass flow out of the boundary layer with the highest possible efficiency of the suction configuration (Bräunling, 2009; Schulte, 2001). The extracted mass flow is usually no longer available for thrust production in terms of combustion and following expansion. Therefore, when the application of mass flow extraction is planned, it has to be considered during the inlet design, as the inlet capture area has to be enlarged to capture a higher mass flow, compensating for the mass loss due to its extraction. At subsonic flight conditions, the suction geometry can

cause additional drag due to flow disturbances in the main flow close to the walls caused by the suction system. The suction geometry in the flow channel wall can be seen as higher surface roughness when the suction is performed through a permeable wall. This permeable wall has usually a high porosity with an increased surface roughness, when compared to a non-permeable wall.

Schulte and Henckels (1996) and Schulte (2001) undertook fundamental experiments, examining the effects of different wall geometries on boundary layer separations. They examined not only passive contours but also active boundary layer suction through a slot perpendicular to the flow direction. The main experiments were focused on the formation, reduction and avoidance of boundary layer separation downstream of a shock. The shock, generated by an external shock generator, interacts with the boundary layer on a flat plate surface. Schulte also showed that his results are transferable to the case of a compression ramp behind a flat plate or first compression ramp. In Fig. 3.16a, the boundary layer separation on a flat plate/ramp configuration is visualised in a Schlieren image. It shows the separation and the formed separation (sep.) shock, generated at the upstream foot-point of the separation shock. At the reattachment point, the re-attachment (re-att.) shock is generated due to a redirection of the flow. The results indicated that it is possible to reduce the boundary layer separation dramatically and hence, the reattachment shock at the end of the separation bubble was erased, as shown in Fig. 3.16b. A suction slot was placed right upstream of a compression ramp as it was proven that it has there the greatest efficiency.

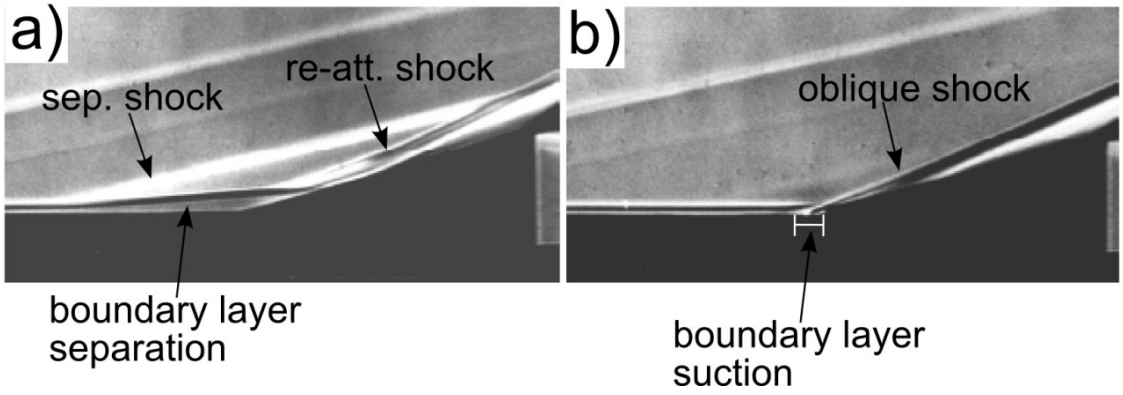

Fig. 3.16: a) Cut-out of a Schlieren image showing a boundary layer separation upstream of a ramp b) Avoided separation due to boundary layer suction upstream of a ramp (Schulte, 2001)

The experiment showed that it is possible to influence and improve the performance of an air inlet by sucking a small portion of the total air mass flow out of the boundary layer. In recirculation areas Görtler-vortices, small contra-rotating vortices, often increase the thermal loads due to high heat transfer to the walls. This effect is proven by the high heat transfer measured between the fluid and the wall. The Görtler-vortices are created because of the concave shape of the reattaching boundary layer, so a secondary flow effect. If a suction force is

applied to the flow, the heat transfer from the fluid onto the wall is significantly lowered, either because the Görtler-vortices do not exist or they are reduced both in size and strength. The thermal loads are about forty per cent higher in the case of existing Görtler-vortices which makes a meaningful difference in the inlet's thermal design process.

Dujardin et al. (2001) produced corresponding results as they examined the effect of boundary layer suction through a slot of different widths in front of the wedge of a flat plate/flat ramp configuration. In their wind tunnel investigations, the flat plate had a length of 140 mm and the following ramp had a 20° angle. At a flow velocity of *M=5.3* the effect of a 2 mm slot compared to a 4 mm slot width was examined with the result that the lower width is not efficient in avoiding the formation of boundary layer separation, even if the separation size was decreased. However, the 4 mm slot width configuration was shown to be sufficient to avoid the formation of the additional shock by taking a sufficiently high mass flow out of the boundary layer. Due to the experimental set-up, it was possible to use the pressure gradient between the concave corner, where the suction slots were installed, and the ramp's base flow downstream of it. As the pressure gradient was given, the slot sizes were varied to achieve different mass flow rates.

The effect of sharp and round injection-slot edge geometries onto the flow was also examined, with the result that the flow topology is in both cases comparable without any significant change. To evaluate the impact of an even higher Mach number flow, Dujardin studied a Mach number *M=10* configuration with boundary layer suction. Again, there was also no significant change to the *M=5.3* flow topology except for the lower oblique shock angle and a slightly higher heat loading at the rear slot edge, both results coming from the higher freestream Mach number case.

Schulte (2001) performed numerical and experimental simulations investigating a further active flow control method by extraction in a hypersonic inlet (for further reference, please refer to 'DLR hypersonic inlet S02A' in Schulte, 2001). The inlet allowed to set different back-pressures and vary the extraction mass flows. The numerical studies were two-dimensional with viscous walls as it was sufficient to simulate the central flow region of the three-dimensional flow, as in the central flow the occurring effects were two-dimensional. In his experiments, he had losses in the air mass flow of about 10 % but increased the total pressure recovery from 10 % to 20 %, where a higher air mass flow had to be extracted through a slot geometry rather than through an aperture plate. The extraction mass flow varied with the pressure in the combustion chamber, as it affects the shape of the flow in the air inlet. A higher combustion chamber pressure leads not only to a higher extraction mass flow but also to a higher total pressure recovery. If the pressure in the combustion chamber rises, over an inlet geometry and flight condition dependent limit, the inlet

chokes and the air mass flow rate decreases significantly. The limit is reached when the back-pressure is increased over the limit of the pressure at the inlet's lip, reached due to ram compression. Even the flow in the inlet is supersonic and no information is moving through the supersonic flow upstream, flow disturbances and other information can be transported upstream in the subsonic boundary layer. Upstream it can cause changes in the flow, which then can degrade the operation stability of the whole engine.

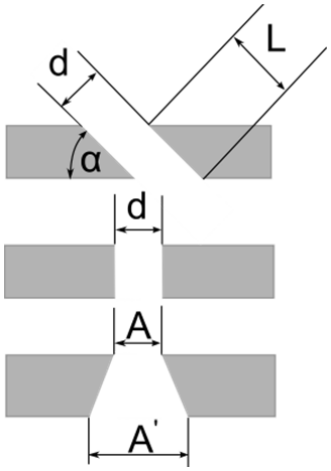

Fig. 3.17: Three bleed hole geometries (after Willis and Davis, 1996) – From Boundary Layer Development Down-stream of a Bleed Mass Flow Removal Region, B.P. Willis and D.O. Davis, 1996; reprinted by permission of the American Institute of Aeronautics and Astronautics, Inc.

According to Bräunling (2009), boundary layer mass flow extraction cannot only be used in the supersonic part of the inlet, but also in the subsonic part, to influence the development of the boundary layer and reduce with it the inlet losses. Mass flow extraction also prevents information transport in the upstream direction from the subsonic to the supersonic diffuser. The high performance increases, due to applied extraction, result from a smoother flow topology, less reductions in the flow channel height and most importantly the avoidance of boundary layer separations.

Willis and Davis (1996) experimentally investigated seven different multiple-hole and two slot geometries at a supersonic freestream Mach number. A hole can be understood as separate drill-hole, with a certain diameter, at a certain angle to the surface, whereas a slot is a groove of a certain length, which runs normally parallel or perpendicular to the flow. Example geometries, which were investigated, are shown in Fig. 3.17. The results favour clearly the usage of multiple bleed holes instead of slots but also they indicate the strong effect of the hole-length-to-diameter ratio (L/d).

Another CFD and experimentally boundary layer removal study was performed by Schulte (2001). He studied the influence of the bleed angle and bleed slot lengths, indicating that bleed angles of about 45° give the best compromise, in terms of a small boundary layer separation downstream of the bleed, between a smooth change in flow direction and a short bleed slot length. Additionally, he also highlights the negative effect on the flow when the slot length is increased.

3.3.2.2 *Mass Flow Injection*

Not many studies about flow control by mass flow injection in supersonic flow exist. However, in the available studies three different approaches have been investigated. Please note, flow injection is understood in this section in respect of its abilities to influence the flow topology by changing shock wave angles or creating shock waves. It is, however, also used in other applications like low mass flow rate effusion for film cooling at the surface of high speed vehicles; within combustion chambers and nozzles to separate the hot and high speed core flow by the injected cold mass flow from the walls, and also to cool turbine blades. These mechanisms will not be discussed here any further but more information is given by Bogard and Thole (2006), Landis and Bowman (1996) and by Schindel and Driftmyer (1992).

Farrukh applied in 2009 for the patent on the creation and control of shock waves due the mass flow injection through microjets. In this concept, depicted in Fig. 3.18, flow at a Mach number of 2.0 is injected perpendicular to the surface through one or multiple 0.4 mm diameter nozzles into a supersonic flow field creating one or a set of shock waves. Several active microjets placed upstream of a perturbance, such as the inlet of an engine, would cause several weaker oblique shock waves compared to only a single shock without any active microjets where a significantly stronger shock wave is created at the inlet. With this method, it is possible to create and control shock wave angles to some extent but the effect reduces with increasing distance from the microjet. The angle of the produced shock wave can be altered by controlling the pressure and temperature of the injected fluid. The ideal number of implemented microjets depends on the size of the perturbance and has to be determined by simulations or experiments.

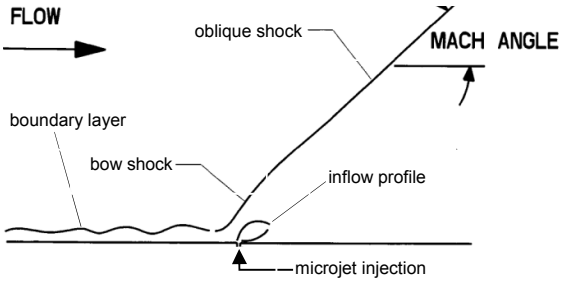

Fig. 3.18: Microjet shock creation (adapted from Farrukh, 2009)

Because of its reduced effectiveness with increasing distance from the microjet, its application for active shock angle control applications is only limited. For example, either to small-scale applications or within the inner section of an inlet, where the distance is shorter between the microjet and the shock impinging point (usually the cowl lip tip for external shock waves). This is more effective than being used in the external section of the inlet where potential large compression ramps are used and the microjet effect would not be noticeable as the distance between microjet and cowl lip is too large.

Haws et al. (2001) of NASA performed CFD studies to control a shock angle by applying a low-speed highly compressed jet stream in freestream Mach numbers of 4.7 to 9.2. In Fig. 3.19, a schematic of the numerical set up is shown. The aim was to ensure shock-on-lip condition at freestream velocities lower and higher than the design Mach number of 6. The compression jet was active at all Mach numbers to ensure shock-on-lip condition and was variable in the mass flow rate. With increasing freestream Mach number, the compression jet mass flow rate and its pressure were increased. The upper surface of the injected compressed mass flow acts as a contact surface for the freestream air that is diverted nearly in the same way as an inviscid solid surface would divert it. When a large amount of low-speed flow is injected, a splitter plate is required to ensure that the low-speed low-energy flow is not flowing into the combustion chamber, causing significantly lower mixing, and combustion efficiencies. Besides the need for a splitter plate (which causes additional weight and viscous drag), the biggest drawback of this principle is the injection mass flow ratio required to influence the shock angle – 30%, which is too much to allow efficient use of this technique. The injection mass flow ratio is the ratio of the injected air mass flow rate to the air mass flow rate at the combustion chamber inlet plane.

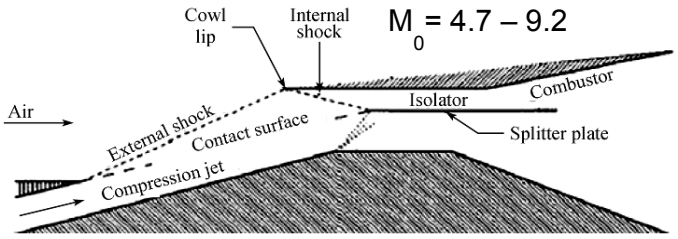

Fig. 3.19: Shock angle increase by compression jet injection (Haws et al., 2001) - with kind permission from Russel Daines

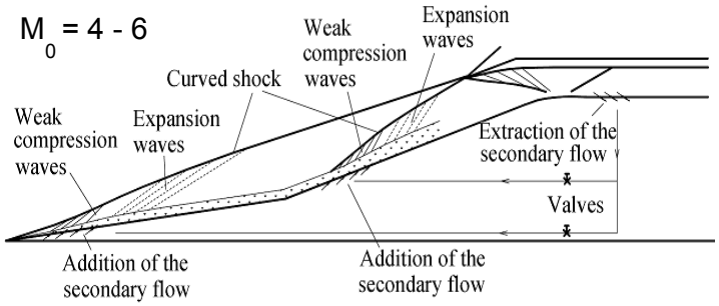

Fig. 3.20: Shock angle increase by low mass flow rate injection (Tan et al., 2007) – Springer, p. 647, fig. 3, with kind permission from Springer Science and Business Media

In 2007, Tan et al. presented in their experimental work a further development of the concept of Haws et al. without the need for the disadvantageous splitter plate and with a lower mass flow rate required to change a shock angle. The principle (Fig. 3.20) involves injecting secondary flow at the foot points of the compression ramps, forming a larger low-speed boundary layer than without injection. This results in an increased shock angle. The steady injection of the secondary flow causes a permanent increase of the boundary layer thickness, as long as the injection is active. The thickened boundary layer acts as the contact surface for the incoming air, which induces an effect of increasing the ramp angle and with it the shock wave angle.

Tan et al. (2007) extracted the secondary flow near the throat area with the aim to stabilise the flow and to avoid the low-speed low-energy mass flow entering the combustion chamber, as this would lower the combustion efficiency. At the same time, the flow extraction near the throat provides the mass flow for the injection at the ramp's foot points. The pressure ratio between the extraction and injection positions is sufficiently high in the investigated case. In this case, the ratio was 25 times the freestream pressure, ensuring a steady mass flow rate from the extraction to the injection. The injection mass flow rate, thus the boundary layer thickness increase can be controlled by controlling the injection pressure of the individual ramps.

Tan et al. (2007) proved their concept in several numerical simulations with viscous walls and one experimental study in a generic setting before its application to a numerical inlet geometry study. Fig. 3.21 shows a pressure plot of a two dimensional two-ramp simulation with applied injection at the first ramp. The injection geometry was modelled by eight slots angled 20° to the surface normal with a pressure stabilization chamber below. The width of the first and last slot was smaller than the middle slots to ensure a smooth start and end of the injection. The aim of that study was to determine the needed reservoir pressure in the stabilization chamber to change the shock angle, measured in this case as the distance of the shock/shock interaction point (labelled as A) to the wall (labelled as B). In this study, with a freestream Mach number of 6, the required pressure was 2.9 times the freestream pressure in order to increase the interaction point distance by 30 %. In Fig. 3.21, the flow phenomena caused by the injection are labelled, which are the boundary layer effects of the secondary flow that increases over the injection geometry. There, also the formation of weak compression waves can be seen. Downstream of the injection, expansion waves are formed. One experimental study confirms the obtained numerical results in a quantitative way, as the identical reservoir-pressure leads to comparable shock angle increases.

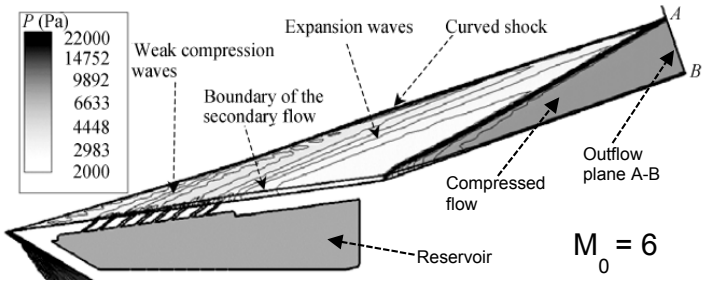

Fig. 3.21: Double ramp shock angle increase with mass flow injection from low-pressure reservoir (Tan et al., 2007) - Springer, p. 652, fig. 7, with kind permission from Springer Science and Business Media

Using the experience obtained, Tan et al. (2007) designed three inlet geometries for a starting Mach number of *M=4* and investigated them in two-dimensional simulations. They choose the starting Mach number of *M=4* as the intention of that investigation was to show the performance

improvements of inlets at higher speeds than the design Mach number, with and without applied mass flow injection.

Even when the starting Mach numbers were identical, the design Mach numbers were not. One inlet had a design Mach number of Mach 6 , denoted as Inlet Design 6 (ID6) and the two other inlets had design Mach numbers of Mach 5 (Inlet Design 5 (ID5)) had no injection, whereas Inlet another inlet was constructed with incorporated injection geometry, described as Inlet Design 5 Injection (ID5J). The flow through each of the three inlets was simulated at three different Mach numbers, which were Mach 4, 5 and 6.

The most important findings were that only 1.8 % of secondary flow was required to maintain the important shock-on-lip condition at the ID5J in a freestream Mach number of 6 which was leading to a significant performance increase, when compared with ID5.

In Table 3.1 the simulation results of the three investigated inlets are presented. Inlets ID5 and ID5J had a 25 % larger throat area and a 10 % lower inlet forebody length when compared with ID6. As shown, at lower Mach numbers (*M=4* and *M=5*) 20% more flow was captured with geometries ID5 and ID5J, in comparison with geometry ID6. In addition, these two inlets had significantly lower forebody drag coefficients than inlet ID6. For example running both geometries ID5 and ID6 at a freestream value of Mach 5 produced 11.6 % less drag in geometry ID5 compared to ID6. Running these two geometries at freestream *M=4* yielded to 8.5 % less drag in geometry ID5 compared to ID6.

Table 3.1: Performance of three inlets (ID6, ID5, ID5J) (adopted from Tan et al., 2007)

	Performance	Inlet Design 6 (ID6) (absolute value)	Inlet Design 5 (ID5) (relative performance gain)	Inlet Design 5 Injection (ID5J) (relative performance gain)
	Air-capture ratio	1	0.0 %	0.0 %
M_0=6	Total pressure recovery	0.435	−19.9%, strong slip layer goes into the engine and possibly leads to unstable operation of the engine	−7.5 %
	Forebody drag coefficient	0.317	−2.0 %	−13.7 %
	Air-capture ratio	0.808	+21.8 %	
M_0=5	Total pressure recovery	0.583	+1.4 %	
	Forebody drag coefficient	0.33	−11.6 %	
	Air-capture ratio	0.639	+20.2 %	
M_0=4	Total pressure recovery	0.683	+2 %	
	Forebody drag coefficient	0.363	−8.5 %	

When simulating the three geometries in *M=6* freestream flow, a 20 % lower total pressure recovery is found with inlet ID5 compared to ID6. This is because the shocks are not impinging on the lip in ID5. Instead, they cause shock/shock interactions and impinge on the cowl further downstream. This results in a different flow and shock structure within the inlet and in stronger boundary layer separations. The large separations have the potential to cause a blockage of the flow channel leading to unacceptably big spillage, therefore, they are often avoided by using bleed. The forebody drag coefficient for the ID5 geometry is 2.0 % lower than for the ID6 inlet. The actively controlled Mach 5 geometry (ID5J) simulated at freestream Mach 6 leads to only a 7.5 % lower total pressure recovery than with geometry ID6, as the shock are impinging on the cowl lip. In addition, the forebody drag coefficient is reducing by 13.7 % in comparison with configuration ID6.

The injected mass flow is extracted at the throat of the inlet and is injected at the foot points of each individual compression ramp. The secondary flow is extracted fully and can be understood as it is in a circular flow. In the throat section upstream of the extraction position, the secondary flow accounts for a height of 15 % of the channel height. During design this channel height reduction has to be considered, so the inlet height must to be enlarged allowing the main mass flow to move through the inlet otherwise spillage will occur.

3.3.3 Existing Ramjet Engines / Supersonic Inlets

The Aérospatiale-BAC Concorde and the Tupolev Tu-144, similar in design and performance, are the only civil used supersonic transport aircraft so far but both are no longer in airline service, mainly due to economic reasons. According to Cain (2010), Concorde used four Rolls-Royce/Snecma Olympus 593 turbojets with afterburners to propel the aeroplane to its design Mach number of 2.2. The two-dimensional inlet geometry was designed that the shock-on-lip condition was fulfilled from Mach 1.3 to a Mach number of 2.2 by the variation of the compression ramp angles.

The Lockheed SR-71 Blackbird has been the only aircraft in service using ramjet technology. It was equipped with two Pratt & Whitney J58 dual mode turbojet/ramjets, which were designed to operate permanently with afterburners to accelerate the vehicle as fast as possible to its most efficient design Mach number, Mach 3.2. The shock-on-lip condition within the axisymmetric inlet with one external compression ramp at an angle of 26° was met by the incorporation of a variable-geometry mechanism that covered a Mach number range from 1.6 to Mach 3.2. To accomplish this high Mach number variation capability, the inlet's spike was engineered to allow up to 0.66 m of cowl translation.

With applied bleed, it is also possible to control the normal shock position in the inlets as it ensures that the shocks stay relatively stable at the bleed positions and are not moving further upstream when the back-pressure from the combustion chambers rise, as in the Lockheed SR-71 Blackbird.

At NASA, various super- and hypersonic inlet studies have been performed. The advantage of these NASA studies over industrial studies is the nearly complete and comprehensive public availability of data. This includes not only the inlet's performance data at various conditions, but also, and not less important, the detailed geometry information. These sets of information allow the validation of CFD codes, including numerical boundary conditions for the simulation of mass flow injection and extraction.

Two interesting and well-documented NASA studies are published by Anderson and Wong (1970) and by Sorensen and Smeltzer (1968). The studies investigated experimentally a large scale, two-dimensional, mixed-compression inlet and an axisymmetric inlet. The axisymmetric inlet study by Anderson and Wong (1970) was used during various CFD validation processes as the bleed rates and the bleed geometry are given in addition to the combustion chamber inflow pressure distribution and the inlet surface pressures. The most comprehensive study of that axisymmetric inlet was performed by Slater and Saunders (2008), who implemented in the NASA CFD code, Wind-CFD, a new porous bleed boundary condition and validated it successfully against the experimental study. Using the same bleed plenum pressures and the same flow rate through their porous boundary condition, they produced results that gave comparable wall surface pressures and comparable normal shock positions, when setting the respective back-pressures measured by experiment.

3.3.4 Importance of Design Mach Number vs. Lowest Shock-on-lip Mach Number

As mentioned above in Section 3.3.3, the inlets of Concorde and the SR-71 Blackbird both had a certain range at which the shock-on-lip condition is fulfilled. Table 3.2 summarises the Mach number range at which the shock-on-lip condition is fulfilled, for Concorde, the SR-71 and an Airbus concept named ZEHST (described later in this section). From the table, it can be seen that a higher design Mach number, which is usually the upper shock-on-lip condition Mach number, leads to an increase in the value of the lowest Mach number at which the compression shock waves can be made to impinge on the lip.

Table 3.2: Shock-on-lip Mach number range for various supersonic inlets

	Concorde	SR-71 Blackbird	Airbus ZEHST
Lowest Mach number for shock-on-lip condition	1.3	1.6	2.5
Highest Mach number for shock-on-lip condition (design Mach number)	2.2	3.2	4
Inlet geometry	two-dimensional	axisymmetric	axisymmetric

This trend can be explained by the required variable geometry for maintaining the shock on the lip. Most inlets need the best performance at their design points as the biggest portion of the trajectory is flown at these conditions. Therefore, the shock-on-lip condition has to be met at the design Mach number. The lowest supersonic Mach number at which the compression shock impinges on the cowl lip depends mainly on a trade-off analysis at which the whole vehicle configuration, its estimated performance and the typical trajectory have to be considered. A lower designed shock-on-lip Mach number results in better performance as less spillage occurs at lower supersonic Mach numbers, whereas higher Mach number flows reduce the weight fraction of the variable geometry. Unfortunately, the trade-off studies of Concorde and the SR-71 Blackbird cannot be reconstructed simply as there are no published studies about such trade-offs (and the technologies and materials used are not as up-to-date as can be achieved today). Hence, the choice of the lowest Mach number for a new inlet design has to be done with reference to the few available inlets or by performing a new trade-off analysis where the vehicle's efficiency over the lowest shock-on-lip Mach number is analysed. In such a trade-off analysis the minimum variable geometry weight and spillage drag have to be considered to obtain meaningful results.

At the Le Bourget air show in Paris 2011, Airbus presented its concept Zero Emission High Supersonic Transport (ZEHST) system. ZEHST is a design for a Mach 4 transport aircraft for 50 to 100 persons satisfying the market wish for a Concorde successor (EADS, 2011). The largest passenger fraction would be business passengers who need to fly over the Atlantic for business meetings and want to be back home in the evening of the same day.

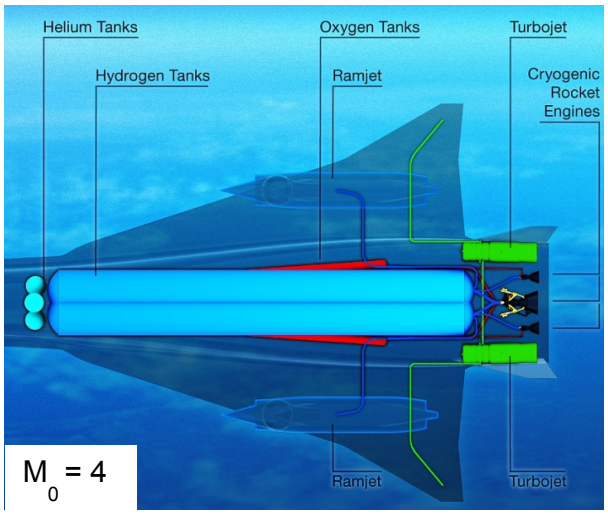

Fig. 3.22: Propulsion system of EADS' ZEHST aircraft (Brändle, 2011)

In accordance to EADS (2011), ZEHST is equipped with a turbojet, a rocket engine and a ramjet engine system, as depicted in Fig. 3.22 showing the propulsion system of ZEHST. The low-bypass turbojet propels the vehicle up to a velocity of Mach 0.8 without the use of afterburners. Then, at Mach 0.8, two small liquid rocket boosters take over, followed by a larger rocket engine, a modification from the commercial Ariane 5 launch vehicle, to the starting Mach number of the ramjet at Mach 2.5. The hydrogen-fuelled ramjets start operation at an altitude of 23 km and accelerate ZEHST up to a velocity of Mach 4 at the cruise altitude of 32 km. The system is planned to cause no emissions during operation. This would be achieved by the use of biological fuel for the turbojets and liquid hydrogen as fuel and liquid oxygen as oxidiser for the rocket engines and the ramjet.

For the ramjet to cover the Mach number range of 2.5 to 4.0, the ramjet inlet has to be variable in geometry to ensure high performance with maintaining shock-on-lip condition.
Several years of work have been done to produce this vehicle concept and a demonstrator vehicle will not be flown before the end of the year 2019 with service operation unlikely before 2040 or 2050.

Skylon is another promising high-speed vehicle in development by Reaction Engines Ltd. (2011). The European Space Agency (ESA) announced in July 2013 that the UK government is investing £60 million for the construction of the powerful hybrid main engine, SABRE (ESA, 2013). Skylon's main purpose is to deliver cargo into orbit unpiloted and thus serve as a cost efficient alternative in comparison to rocket systems for satellite transportation. Once in operation, cargo with a mass of 12 tonnes could be taken up to an altitude of 300 km or 9.5 t to 460 km altitude when launched at the equator to benefit from the Earth's rotation. Skylon is designed to be propelled by the SABRE engine, which is a rocket engine with an additional pre-cooled turbo-compressor allowing operation from zero velocity up to a Mach number of 5.5 by using the air breathing turbo-compressor mechanism. When the air density is too low, for efficient air breathing mode, the rocket mode is switched-on with its liquid oxidiser. SABRE's axisymmetric inlet maintains the shock-on-lip condition with a translating cowl but unfortunately, detailed information is proprietary and thus not available at this stage.

3.3.5 Conclusions about Shock Angle Control

The previous literature survey shows that there are several methods to change shock wave angles. The most promising shock wave changing methods are the shock angle increase by mass flow injection or angle decrease by mass flow extraction. In Section 4.10, after the validation of

the numerical tools, it is investigated which of the two methods is the more promising option and will be used for the development of an alternative shock angle control system.

For the shock wave angle increase only one method is worthy of closer consideration, as it shows the most promising flow controlling capabilities. This is the method of Tan et al. (2007), where fluid is extracted at the throat and injected at the foot points of the compression ramps. Although the method shows potential, there are no further studies, neither of the authors of that study, nor of others, intensifying the research on that topic. In particular, the potential to produce good performance of the engine at lower supersonic Mach numbers using this method is of great interest, since it could lower or remove the need to use variable geometry in an inlet.

As pure ramjets are not able to produce any static thrust, an additional thrust producing system has to be used. The turbojet, whether with or without an afterburner, is widely used for the first acceleration phase up to the ramjet operational speed. The ideal would be an engine, consisting of a turbojet/ramjet-dual-mode engine where the ramjet mode would start its operation at the upper operational limit of the turbojet. As there are so far no high Mach number ramjets in commercial usage, the focus has to lie on lower Mach number applications to ease and broaden possible fields of application, especially since there already exists the Mach 6 study of Tan et al. (2007), which could act as a fundamental source for this study. If shock angle variation at low supersonic Mach numbers, like $M = 1.6$, is inefficient, the shock angle variation could also start at a velocity of Mach 2.5 or even higher when considering EADS' latest high speed transport aircraft, ZEHST, ramjet speed regime.

The active EADS' development on ZEHST and the UK financial investment into Skylon is proving that high performance supersonic inlets are still in the research focus. In both cases, the shock-on-lip condition across a Mach number range is ensured with variable geometry. As the fulfilment of the shock-on-lip condition is a major requirement in future ramjet development, this study is concerned with an alternative method to alter the shock wave angle without the incorporation of variable geometry.

To sum up this chapter, firstly ramjet engines are discussed concentrating on the inlet. The high importance that the oblique shock should impinge on the cowl lip is illustrated, as otherwise performance losses have to be expected. Various compression methods are discussed, showing that rectangular quasi-2D inlets are simple to design but suffer from the boundary layer formation on the side walls. Due to their design, axisymmetric inlets do not have side walls, leading to higher maximum performance. Furthermore, different alternative passive and active flow control

methods are analysed. The focus is on active methods as their usage implies the achievement of flow control with a higher accuracy at a higher Mach number range than passive methods. Identified, as the most promising methods, were the extraction or injection of mass flow right upstream of a compression ramp. Whereas injection allowed in the investigation of Tan et al. (2007) to increase the shock angle by 5° whilst injecting 0.2 % of main flow to control the shock angle. To gain a deeper understanding about this, so far only superficially investigated, mass flow injecting shock angle increasing method, this study continues first with a numerical background, including the validation of the boundary conditions in Chapter 4. In the following, it is than concentrating on the identification of the most important injection parameters in Chapter 5, before their application is investigated in Chapters 6 and 7.

4 Validation of Applied Numerical Methods

Computational Fluid Dynamics, CFD, is the main method used in this study for the simulation of the flow, the determination of its properties and the analysis of the occurring flow phenomena. To ensure the reliability of the results, an extensive validation will be performed. For validation, well-documented wind tunnel studies are numerically reproduced. The aim of this is to reproduce almost identical results, ensuring that future results and predictions obtained from the used CFD tool: the DLR developed flow solver, TAU-Code, are reliable and accurate. The TAU-Code flow solver can compute solutions from three-dimensional and hybrid meshes by solving, for example Euler (inviscid) or Reynolds-averaged Navier-Stokes (RANS) equations. Due to its good code parallelisation on multiple computer processing unit cores, the required time for solving a given problem becomes a quasi-linear relationship with an increasing number of cores when solving a sufficiently complex calculation.

Most parts of the DLR TAU-Code are already validated against wind tunnel and free flight test data, and are used in industrial research, but also in the development of major European aerospace companies like EADS and especially widely by its subsidiary enterprise Airbus. The DLR TAU-Code enables the simulation of fluid flow in a perfect gas, in chemical and thermal equilibrium and in non-equilibrium real gas. The solver uses a vertex-centred scheme and in this study, an Upwind scheme is used for spatial discretisation in second order. For the time integration, explicit multistep Runge-Kutta schemes are used. For convergence acceleration a multigrid method, a local time-stepping concept and residual smoothing algorithms are implemented. In all simulations, three multigrid levels are used for the calculations. Switching between the multigrid levels is done in predefined W-cycles. The subsonic validation of the code is described by Schwamborn et al. (2006), Widhalm and Rossow (2002), Melber et al. (2000), Galle (1999) and Gerhold et al. (1999). The supersonic and hypersonic speed regime validation of the solver, up to a Mach number of 25, is discussed by Mack and Hannemann (2002), Gerhold et al. (1999) and Hannemann et al. (1999).

Since this study is concerned about flow control by the extraction and injection of mass flow into the main airflow in the inside of super- and hypersonic inlets, a particular focus lies on the extraction and injection boundary condition and their validation which have not been not validated so far. These aspects are described below in Sections 4.8 and 4.9 respectively.

To ensure that the numerical methods, which are applied to the problems, lead to sufficiently accurate results, this validation process is obligatory.

An overview about the equations used within the TAU-Code is given. With them, the TAU-Code is determining the flow behaviour in an iterative way. The equations are presented below in the conservative form, which is the integral form, allowing the capture of discontinuities, like shocks, in the solution, where appropriate. In the conservative form, the equations are given in a system of the mass, momentum and energy conservation laws. The governing equations for fluid flow as a viscous and compressible ideal gas are shown first as they serve as the basis for the following equations. All succeeding equations are from Galle (1999) who developed at DLR the major part of the first DLR TAU-Code version, but also from Versteeg and Malalasekera (2007), Oertel jr. and Laurien (2003), Zucker and Biblarz (2002), Anderson (2011) and Anderson (1995). The time-integral form, i.e. the Reynolds-averaged Navier-Stokes (RANS) approach is based on the conservation of mass, momentum and energy in a chosen control volume.

4.1 Governing Equations

The motion of a Newtonian fluid can be described by the Navier-Stokes equations. To enable the description of discontinuities like shock waves, the integral forms of these equations are used. When considering a control volume of a flow, the conservative Navier-Stokes equations that govern the movement of such flow can be expressed as:

$$\iiint_V \frac{\partial}{\partial t} \vec{W} \, \mathrm{d}V = \iint_\Omega \bar{\bar{F}} \cdot \vec{n} \, \mathrm{d}\Omega \, . \qquad \textbf{Eq. 4.1}$$

with the chosen volume V, the time t, the conservative state variables $\vec{W}$, the convective fluxes $\bar{\bar{F}}$, the outer normal vector $\vec{n}$ and the geometric boundary of the control volume Ω. The conservative state variables can be given by:

$$\vec{W} = \begin{bmatrix} \rho \\ \rho u \\ \rho v \\ \rho w \\ \rho E \end{bmatrix}, \qquad \textbf{Eq. 4.2}$$

with the specific total energy E.

The flux density tensor $\bar{\bar{F}}$ can be split into an inviscid $\vec{F}^i, \vec{G}^i, \vec{H}^i$ and a viscid $\vec{F}^v, \vec{G}^v, \vec{H}^v$ contribution:

$$\bar{\bar{F}} = \left(\vec{F}^i + \vec{F}^v\right) \cdot \vec{\imath}_x + \left(\vec{G}^i + \vec{G}^v\right) \cdot \vec{\imath}_y + \left(\vec{H}^i + \vec{H}^v\right) \cdot \vec{\imath}_z \qquad \textbf{Eq. 4.3}$$

with the Cartesian unit vectors $\vec{i}_x, \vec{i}_y, \vec{i}_z$ and:

$$\vec{F}^i = \begin{bmatrix} \rho u \\ \rho u^2 + p \\ \rho uv \\ \rho uw \\ \rho Hu \end{bmatrix}, \quad \vec{F}^v = -\begin{bmatrix} 0 \\ \tau_{xx} \\ \tau_{xy} \\ \tau_{xz} \\ u\tau_{xx} + v\tau_{xy} + w\tau_{xz} + k\dfrac{\partial T}{\partial x} \end{bmatrix},$$

$$\vec{G}^i = \begin{bmatrix} \rho v \\ \rho uv \\ \rho v^2 + p \\ \rho vw \\ \rho Hv \end{bmatrix}, \quad \vec{G}^v = -\begin{bmatrix} 0 \\ \tau_{xy} \\ \tau_{yy} \\ \tau_{yz} \\ u\tau_{xy} + v\tau_{yy} + w\tau_{yz} + k\dfrac{\partial T}{\partial y} \end{bmatrix}, \qquad \textbf{Eq. 4.4}$$

$$\vec{H}^i = \begin{bmatrix} \rho w \\ \rho uw \\ \rho vw \\ \rho w^2 + p \\ \rho Hw \end{bmatrix}, \quad \vec{H}^v = -\begin{bmatrix} 0 \\ \tau_{xx} \\ \tau_{xy} \\ \tau_{xz} \\ u\tau_{xz} + v\tau_{yz} + w\tau_{zz} + k\dfrac{\partial T}{\partial z} \end{bmatrix},$$

with the shear stress τ and the thermal heat coefficient k .

When regarding flow through a duct one can assume a quasi-one-dimensional flow through it, as stated by Anderson (2004). This assumption approximates the actual occurring flow and allows the formulation of the governing equations in the integral form of the conservation equations. Illustrated in Fig. 4.1 is a diverging duct with uniform flow at stations 1 and 2. The variable indices 1 and 2 are indicating the inflow (1) and outflow (2) conditions.

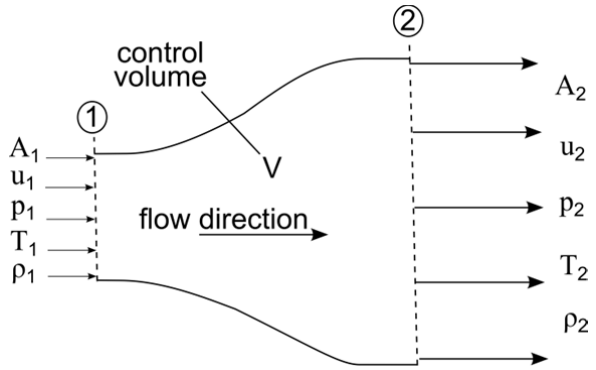

Fig. 4.1: Control volume illustrating quasi-one-dimensional-flow through a diverging duct

Based on Fig. 4.1, the quasi-one-dimensional continuity equation can be determined, for the Euler and Navier-Stokes equations in the conservation form, that states that the mass flow rate through a duct is constant at the inflow and at the outflow and can be given by:

$$\rho_1 A_1 u_1 = \rho_2 A_2 u_2 \qquad \text{Eq. 4.5}$$

The identical conservation leads to the momentum equation that is defined by:

$$\rho_1 A_1 + \rho_1 u_1^2 A_1 + \int_{A_1}^{A_2} p\, dA = p_2 A_2 + \rho_2 u_2^2 A_2 \qquad \text{Eq. 4.6}$$

The energy equation for steady, adiabatic inviscid quasi-one-dimensional flow is defined by:

$$h_1 + \frac{u_1^2}{2} = h_2 + \frac{u_2^2}{2}, \qquad \textbf{Eq. 4.7}$$

with the specific enthalpy h:

$$h = c_p T\,, \qquad \textbf{Eq. 4.8}$$

where c_p is the specific heat capacity at constant pressure.

The pressure can be determined with the equation of state:

$$p = (\gamma - 1)\rho\left(E - \frac{u^2}{2}\right) \qquad \textbf{Eq. 4.9}$$

where γ is the ratio of specific heats and the energy E:

$$E = e + \frac{u^2 + v^2 + w^2}{2} \qquad \textbf{Eq. 4.10}$$

with the specific energy:

$$e = c_V T\,, \qquad \textbf{Eq. 4.11}$$

where c_v is the specific heat capacity at constant volume.

4.2 Perfect Gas Equation Simplifications – Equations of State

When simulating a gas at relatively low pressure (about 50,000 Pa to 500,000 Pa) in which no high temperature effects are occurring, leading to the presence of thermodynamic non-equilibrium flow, then a perfect gas can be assumed. This assumption reduces significantly the numerical complexity of a given problem, as the ideal gas law can be applied. To regard a fluid as an ideal gas, it is assumed that the considered molecules are moving frictionless through the fluid and that the intermolecular forces between the molecules are so small that they can be neglected. The above stated requirements will be fulfilled in all simulations in this work, therefore, the perfect gas assumption is presumed in all performed simulations. The ideal gas law is only valid if the pressure is low and the temperature is high.

When a perfect gas is assumed in a calculation, Eq. 4.12 and Eq. 4.13 present a simplification of the general valid real gas equations. The simplified thermal equation of state is then given by:

$$p = \rho R T\,, \qquad \textbf{Eq. 4.12}$$

whereas the specific gas constant, R, is determined by the following equations:

$$R = c_p - c_v \,, \qquad \textbf{Eq. 4.13}$$

with the specific heat capacity at a constant pressure c_p = 1.01 kJ/(kg·K) and the specific heat capacity at a constant volume c_v = 0.718 kJ/(kg·K) for dry air.

The enthalpy H of the system is defined with the internal energy E_{int} as:

$$H = E_{int} + pV \,. \qquad \textbf{Eq. 4.14}$$

The mentioned Navier-Stokes equations are formulated based on the four equations of the conservation of mass, momentum, energy and state in Eq. 4.5, Eq. 4.6, Eq. 4.7 and Eq. 4.9.

With the given explanations, equations and the background of the equations used, the DLR TAU-Code is described. That follows in the next section a discussion of the turbulence modelling.

4.3 Turbulence Modelling

In this section, the fundamentals of numerical turbulence modelling are presented in accordance to Oertel jr. (2008), Versteeg and Malalasekera (2007) and Wilcox (2006). First, the different numerical approaches are illustrated and finally the adopted approach is discussed in detail.

When regarding a flow field, in which the Reynolds number is always under the critical Reynolds number Re_{crit}, the flow is smooth, without the formation of turbulent vortices. The complete flow is then called laminar. The critical Reynolds number is the maximum Reynolds number at which the complete considered flow is laminar; therefore, no turbulent flow features occur even the flow is mostly three-dimensional and non-stationary.

If the Reynolds number is increased above the critical Reynolds number by changing flow field properties, the flow changes from its regular order to a random nature with the formation of vortices. This flow is then described as turbulent and turbulence models have to be used during numerical computation, for capturing these flow features. In turbulent flow, the flow layers close to each other are not nearly stationary and clearly three-dimensional movements of the flow particles occur.

Various types of numerical turbulence determination methods are available. They differ from each other in the accuracy and in the required numerical effort to solve a given problem. Detailed and accurate time-dependent three-dimensional results can be obtained using the method of direct numerical simulation (DNS). This method requires a very fine mesh and time resolution,

which is thus able to resolve even the smallest vortices. However, the use of such high-resolution meshes requires a significantly higher numerical effort for solving DNS calculations, therefore it is not being used for the simulation of many large scale problems.

A smaller numerical effort to DNS, is large eddy simulations (LES) for which a mesh with a lower resolution is sufficient. By the use of LES more complex cases can be simulated, but still a large numerical effort has to be invested for solving all simulations with that method.

An even further simplification of the turbulence determination is the time- and location-averaging Reynolds method (Anderson, 2006). It is breaking up the location- and time-dependent flow quantities into the averaged quantities and into a fluctuation fraction. The fluctuation quantities are averaged over the given time period. That period needs to be long enough to ensure independence between the averaged quantities and the selected period. When applied to the Navier-Stokes equations, this approach produces the Reynolds averaged Navier-Stokes (RANS) equations.

With each of the above-described methods, the influence of three-dimensional turbulence can be calculated. Combined with the equations of conservation of mass, momentum and energy it becomes feasible to simulate turbulent flows in a time independent way. In this research study RANS is used.

The flow close to a wall is influenced by viscous effects. Its velocity depends mainly on its distance to the wall y, the fluid density ρ, the viscosity μ and the wall shear stress τ_w.
From the so-called law of the wall the dimensionless values of the velocity u^+ and the wall distance y^+ can be determined. The distance between the surface and the first mesh node in the boundary layer is set close to the wall distance y^+:

$$u^+ = \frac{u}{u_\tau} = f\left(\frac{\rho u_\tau y}{\mu}\right) = f(y^+)\,, \qquad \textbf{Eq. 4.15}$$

the following general valid functions can be derived:

$$y^+ = \frac{u_\tau y}{v}\,, \qquad \textbf{Eq. 4.16}$$

With the friction velocity u_τ and the local dynamic viscosity τ_w:

$$u_\tau = \sqrt{\frac{|\tau_w|}{\rho}}, \qquad \textbf{Eq. 4.17}$$

$$\tau_w = \mu_w \frac{\partial u}{\partial y}. \qquad \textbf{Eq. 4.18}$$

The viscosity μ is dependant of the temperature and can be calculated for air with Sutherland's law:

$$\mu = \mu_0 \left(\frac{T}{T_0}\right)^{3/2} \frac{T_0 + 110}{T + 110}. \qquad \textbf{Eq. 4.19}$$

The flow over a viscous wall can be split up in three regions. These are:

- The layer, in contact with the wall, where the velocity profile shows a linear behaviour. In this layer, Eq. 4.15 can be simplified for $y^+ < 10$ to $u^+ = y^+$.
- The region between the contact layer and the freestream flow shows a logarithmic profile of the velocity over the wall distance, therefore it is called log-layer:

  $$u^+ = \frac{1}{\kappa_K} \ln(y^+) + B = \frac{1}{\kappa_K} \ln(E y^+), \qquad \textbf{Eq. 4.20}$$

  with the Karman constant $\kappa_K \approx 0.41$ and the additive constants for smooth walls $B \approx 5.5$ and $E \approx 9.8$, with increasing wall roughness the value of *B* decreases.
- The freestream flow outside of the boundary layer can be characterised by a constant velocity. The boundary layer height is often determined by the height at which the velocity over a surface is 99 % of the freestream velocity. The transition from freestream to the boundary layer can be calculated with:

  $$\frac{u_{max} - u}{u_\tau} = g\left(\frac{y}{\delta}\right), \qquad \textbf{Eq. 4.21}$$

  where the wall shear stress u_τ can be understood as cause for a velocity reduction with decreasing distance to the boundary layer. The log-layer equation is valid in the region between $0.02 < \frac{y}{\delta} < 0.2$. For larger values Eq. 4.21 is correct. In the overlapping region, both equations have to lead to the same results. Therefore, Eq. 4.22 is introduced:

  $$\frac{u_{max} - u}{u_\tau} = \frac{1}{\kappa} \ln\left(\frac{y}{\delta}\right) + A, \qquad \textbf{Eq. 4.22}$$

  where *A* is a constant, required to find the explicit solution in the overlapping region.

With Eq. 4.15 to Eq. 4.22 the influence of a viscous wall onto a flow can be determined for every position normal to the surface.

In the current study, the first structured boundary layer height is always set that a y^+ value close to $y^+ = 1$ results. This ensures a good capturing of the created turbulence effects from the surface. In addition, it ensures that the whole boundary layer can be resolved with a sufficiently fine resolution, at acceptable numerical costs.

It remains to mention that the different turbulence prediction methods are not working in a deterministic way. This means that it is not possible to predict the explicit position of each flow molecule that is affected by any turbulence.

4.3.1 Turbulence Model Applied

The two-equation Wilcox *k-ω* turbulence model with the Shear Stress Transport (SST) correction is used during all simulations as Slater and Saunders (2008) and Tan et al. (2007) used it during their validation and numerical study. In these two referenced studies, mass flow extraction and injection studies were undertaken. In both cases, the SST turbulence model was leading to reliable results as the simulations predicted well the experimental behaviour. Therefore, it is documented that the SST turbulence model is leading to the most accurate boundary layer separation and shock/shock interaction results of the available RANS turbulence models. According to Bardina et al. (1997) and Nichols (2008), the SST turbulence model is combining the advantages of the *k-ε* model in the freestream flow and near boundary layer edges and in free-shear layers with the advantages of the *k-ω* model near solid walls. A zonal weighing for the model coefficients is used for the determination whether the *k-ε* or the *k-ω* model is applied. A blending function ensures a smooth switching between them.

The turbulent eddy viscosity function is also modified, leading to a better prediction of the boundary layer separations caused by adverse pressure gradients. Without this modification, the separations would be under-predicted in terms of their sizes and their occurrence, leading to too optimistic performances. More details on the used model equations, constants and parameters, the blending function and the modification on the turbulent eddy viscosity function is given by Menter (1993) and Bardina et al. (1997).

Concluding, due to the possibility to use a turbulence model that was successfully applied to comparable problems, the SST turbulence model presents the best option and will be used for this study.

4.4 Discretisation

The equations that have to be solved in computational fluid dynamics are based on partial differential equations. In general, these equations contain first order differentials and are difficult if not impossible to solve accurately at all flow points theoretically and so numerical methods are used to solve these equations. If it is accepted that the flow variables are defined only at discrete times and only at discrete positions, the approximate solution of such differential equations becomes possible at the expense of the numerical accuracy of the solution. The conversion from the continuous into the discrete description of a flow problem is called discretisation. Whenever possible in this study, the equations are solved with second order accuracy. Across shocks second order accuracy is difficult to maintain and so first order equations are used to enhance the numerical stability in that physically discontinuous area. This approach allows the continuous determination of the changes of the variables in space and time at every position in the flow field. In this partial differential equation method, the changes in velocity over time are solved with first order equations. Changes in displacement over time are resolved, mainly, with second order accuracy. However, this is numerically very resource consuming and not applicable for most engineering problems. Current research projects are focussing the application of third and fourth order solutions enhancing the accuracy of the results but also the computational resources to solve the equations (Andren, 2011).

However, as in this study, sub-, super-, and hypersonic flows are investigated, discontinuities, i.e. shock waves, occur. To solve the flow equations, the TAU-Code is used, which is a time-step based solver, solving the hyperbolic equations. This means that the impact of the local discontinuity and its influence onto a flow region around the discontinuity can be determined. For this local discretisation, the second-order Upwind-method is used. In this study, the AUSMDV-scheme is the chosen Upwind-method, which is based on the combined splitting of flux differentials and flux vectors, as described by Wada and Liou (1997).

As the TAU-code is time-step based, derivations of the time $\left(\frac{\partial}{\partial t}\right)$ are determined even for stationary flow fields. Through the time dependent calculation, different flow equation solving methods for subsonic (elliptic equations) and supersonic flow fields (hyperbolic equations) are not necessary.

For the discretisation of the flow field, the TAU-code is using a finite-volume method (FVM). For this, the flow field is divided into non-overlapping control volumes that are forming the primary mesh. The calculation of the flow variables is performed for the cell vertices (P_i). In Fig. 4.2

primary and secondary mesh cells and a cell vertex (P_i) are illustrated. As the cell vertices are not enclosed by a defined volume, auxiliary volumes are created which are enclosing each vertex of the primary mesh, forming a so called secondary mesh. The cell centred points of the secondary mesh are corresponding to the cell vertices (P_i) of the primary mesh - thus this approach is also called cell vertex-centred grid.

For solving these differential equations, the initial values have to be given or chosen at every discrete point within the flow field and the surrounding boundaries. CFD codes always solve time marching equations for time dependent and steady state problems (but there is a difference

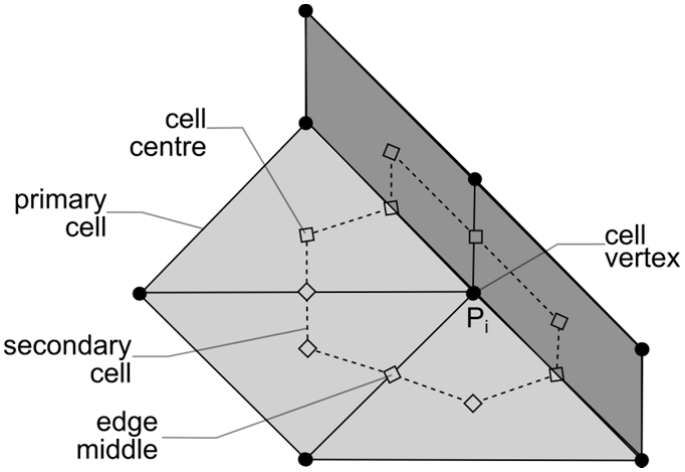

Fig. 4.2: Sketch of the primary and secondary mesh (adopted from DLR, 2012)

between the inner convergence loop and the outer time accurate loop), even if a stationary problem is investigated. A stationary problem is describing a flow field, in which the flow properties at every individual position are constant over time, when a converged solution is achieved. By this, only parabolic-hyperbolic equations have to be solved for all problems. This is mainly done by a time-marching technique. Another reason for the application of the time-marching equations is that the non-linearity of the Navier-Stokes equations can lead to more than one solution; the physically correct solution and other numerical possible solutions for a specific problem. The flow solver can converge to a non-stationary solution in which boundary layer separations lead to oscillations in the solution. Time-marching methods are able to capture such phenomena. The usage of time-marching methods also allows the solution of non-time-dependent flow problems and finds also application in the TAU-code.

For the discretisation of time and space, different implicit and explicit methods are available. In the TAU-Code, mainly the explicit Runge-Kutta scheme and the implicit Backward-Euler methods are used. Their usage depends mostly on the stability of the calculation as the implicit method allows higher Courant-Friedrichs-Lewy (CFL) numbers. This means that larger time steps can be

used, quickening the calculation. Note that the CFL number is a measure of the stability of the scheme and thus the time step should not be increased if the corresponding increase in the CFL number reduces the ability of the numerical schemes to ensure stability and converge to the correct answer. Normally, second order differentials are solved to gain precise solutions. However, in areas with high gradients (near shocks, near the stagnation point, etc.), a switch is used to reduce from second order accuracy to first order. A limiter function is used to avoid local overshooting of the flow variables near shocks by a minimum/maximum clipping strategy. For further information on the time and space discretisation, please refer to Anderson et al. (2012), Oertel jr. and Laurien (2003) and Haselbacher and Blazek (1999).

4.5 Numerical Errors and Uncertainties

When investigating physical effects in research studies, the error sources have to be as small as possible, ensuring results that are as reliable as possible. In a wind tunnel, errors occur due to disturbances in the freestream flow, inexact alignment of the model to the freestream flow, errors in the measurement instrumentation and inexact freestream flow conditions.

When regarding numerical simulations, the errors arise from different sources. As described above in Section 4.3 the TAU-Code is using RANS equations for solving the given flow problems. As time-averaged RANS is a simplification of the time-dependent DES and LES approaches, deviations of the exact solution are the consequence. As the application of RANS equations could lead to convergence to non-physical solutions, the final solutions have to be checked for their physical correctness.

In the guidelines from the AIAA's CFD Standards committee, uncertainty is defined as *"a potential deficiency in any phase or activity of the modelling process that is due to the lack of knowledge"* (AIAA, 1998, p.4) whereas errors are *"a recognisable deficiency in any phase or activity of modelling and simulation that is not due to lack of knowledge"* (AIAA, 1999, p.5).

Different types of errors exist. Some are caused due to local factors, like the local mesh quality. Others are influencing the complete calculation, such as round-off errors and discretization errors which count both as acknowledged errors. Unacknowledged errors have the potential of influencing the whole flow domain as well and cannot be quantified as precisely as the acknowledged errors. Computer programming errors and errors in the flow solver usage belong to the category of unacknowledged errors and their influence on the results quality is not assessable before undertaking the simulation (Slater, 2008). For further information on numerical errors and

uncertainties and their effect on the quality of flow simulations, please refer to Slater (2008) and AIAA (1998).

4.6 Boundary Conditions Applied

In this section, the different boundary conditions that are used in this study are described (DLR, 2012 and Hannemann, 1997):

- The *exit-pressure outflow* boundary condition allows an outflow of a mass flow from the inside of a regarded numerical domain to the outside of it. Outside of the numerical domain, the flow and its properties cannot be considered, and its behaviour cannot be predicted anymore. The opposite of outflow is inflow, where mass flow is flowing from the outside of a domain (i.e. a region which is not simulated) to the inside of the prescribed domain (which is simulated). The *exit-pressure outflow* boundary condition is setting an outflow boundary with only prescribed static pressure. All remaining variables are then extrapolated from the mesh cells in contact with the outflowing flow. In this study, this boundary condition is used to simulate, within the inlet, occurring back-pressure, acting from the combustion chamber upstream in the direction of the inlet. It is used to position the normal shock close to the inlet throat.

- The *actuation* boundary condition allows injection and extraction (i.e. inflow and outflow) of flow or a combination of both. In this study, it is used as an extraction condition, as it allows outflow when the pressure inside the domain is higher than the defined pressure of the boundary condition, see Section 4.8. The *actuation* boundary condition allows the prescription of every possible parameter, therefore it allows also injection, mass flow transfer from the outside of the chosen computational domain into the domain, when the pressure at the domain-inside is lower than the prescribed pressure of the boundary condition (simulating the pressure at the domain-outside). The *actuation* boundary condition is numerically very stable and allows both subsonic and supersonic out-going flow.

- The boundary condition *symmetry plane* is projecting the momentum flow variables onto the symmetry boundary condition. It can only be used in symmetric computations and it is essential that the *symmetry plane* is lying on a geometrical symmetry plane, which goes through the geometry's centre. In one simulation not more than two *symmetry planes* are allowed, which permits to model and simulate only a segment of a symmetric case. By this, the computational effort is reduced significantly as only the chosen segment of the original

domain of interest is simulated. Once the results are obtained for the segment, the results for the whole domain can be pieced together using the knowledge of the symmetry boundary positions.

- The boundary condition *axisymmetric axis* is needed for quasi-three-dimensional simulations. It is important that the mesh, at this boundary, is one cell wide to allow proper transformation from the 2D mesh to the quasi-3D mesh.

- The *supersonic outflow* boundary condition only allows outflow. It is numerically very robust as it can deal with e.g. outflowing subsonic boundary layers without any difficulty. All flow variables are extrapolated from the mesh cells in contact with the *supersonic outflow* boundary condition. Therefore, it has no influence on the inside of the domain as information is only allowed to travel downstream in supersonic flows.

- The *reservoir-pressure inflow* boundary condition is defining an inflow into a computational domain. With the user prescribed total pressure and total density values the TAU-Code determines the velocity at the boundary condition through an isentropic expansion from the reservoir condition. If the total pressure in the reservoir is set to a lower value than the total pressure prevailing on the flow side, then the flow is directed out of the domain. In this extraction case, the *reservoir-pressure inflow* boundary condition is working in a similar way as the *exit-pressure outflow* boundary condition.

- Most physical solid surfaces of the investigated domains are set as a *viscous wall*. This boundary condition ensures that a wall behaves as no-slip wall (i.e. generating a boundary layer) without any normal flow velocity to it. Because all investigated flow test cases are wind tunnel experiments, the walls are set as isothermal with a prescribed wall temperature, which are in heat radiation equilibrium.

- The boundary condition *Euler wall* is set under some cases when the behaviour of a slip wall has to be simulated. It ensures that no boundary layer is generated over this surface and that there is no flow velocity normal to it. Similar to the *viscous wall* boundary condition, the wall temperatures can be prescribed.

- In most aerospace CFD cases the computational domain is framed to most sides of the investigated volume from the boundary *farfield* which allows the in- and outflow of mass flow. The *farfield* boundary should be far away from the investigated subject and should not

be influenced by the investigated subject to obtain a fast converged and correct solution. In simulations in which a free flying object is analysed, the farfield boundary condition is usually used for the outer surrounding boundaries. At the *farfield* boundary, the pre-defined fixed freestream conditions are present.

Most simulations in this dissertation are performed in quasi-three-dimensions. For the generation of the quasi-three-dimensional mesh, a two-dimensional mesh is rotated for 0.1° about the axisymmetric axis to obtain a mesh with a depth of 1 cell. With this mesh, the flow simulation, in which quasi-three-dimensional code terms are activated, is performed. Thus, results comparable with three-dimensional results can be obtained for axisymmetric simulations at 0° angle of attack, while reducing the computational effort significantly, by a factor of at least 22.5, when otherwise at three-dimensional sixteenth part of an axisymmetric geometry would have been simulated, with a resolution of one cell per degree in radial direction. Thus in all cases a finite volume approach is used to solving all cases at all parts of the domain.

4.7 Tools Used

In this section, the software tools used during this research study, besides the above outlined TAU-Code flow solver, are described. This includes the mesh generation, the mesh and solution adaptation and the visualisation processes.

4.7.1 Mesh Generation

For the application of the finite-volume method, the flow domain has to be partitioned into non-overlapping cells with nodes at each cell corner. The flow field is the geometric negative of the investigated body including the surrounding area, to resolve all flow phenomena, which may influence the flow in focus. For the numerical computation of a fluid flow, the considered flow field is divided in small cells, which together form a mesh. In other words, the mesh cells occupy the volume of the flow, but stop at the solid surfaces, i.e. no mesh cells are created within a solid. Hence the flow region and its corresponding mesh looks like a photographic negative of the original CAD model.

Three different mesh types exist, which are the structured, unstructured and the hybrid mesh. Structured meshes comprise quadrilaterals in two-dimensions and hexahedra in three-dimensions. Their main advantages are the fast mesh generation; stretching a mesh so that small cells are present near a boundary and larger cells further away in the far-field; sometimes a good Cartesian alignment with the flow direction; and that the cell nodes can be numbered ordinary by the counter *i* and *j*, when regarding a two-dimensional case, the neighbouring nodes differ from

each other by only one value. Their disadvantages are that complex geometries cannot be meshed in an efficient way and adding a single additional point to the mesh later for refinement is not allowed.

Unstructured meshes allow an efficient and flexible method to mesh complex geometries. Furthermore, they offer good stretching mesh algorithms and efficient local mesh refinement, i.e. variable mesh resolutions, which is the node spacing. This allows having a fine resolution close to the geometry surface or at key areas, but also coarser resolution with increasing distance to such spots. The disadvantages of this approach is that the cells cannot be labelled in a simple way, resulting in a more memory-intensive data structure (a connectivity file) , in which the neighbouring relationships are stored (Ierotheou et al., 1995) and alignment of the mesh cells with a dominant flow direction is not possible.

In hybrid meshes the advantages of the structured and unstructured meshes are combined, leading to a structured mesh in the boundary layer region above solid surfaces and an unstructured mesh in the remaining flow domain. This leads to a good and efficient resolution of the boundary layer flow and in addition to a reduced number of cells with increasing distance to the surfaces of the geometry.

The cell sizes have to be created, on the one hand small enough, which is case dependent, to capture all flow phenomena with a sufficient fine resolution, but on the other hand, as large as possible to ensure cost efficient computations. The CFL number and y+ values are valuable aids to ensuring sufficient mesh quality is attained.

4.7.1.1 *Mesh Generator Tool: CentaurSoft - Centaur*

For this research, all meshes were generated with the commercial software package Centaur from CentaurSoft (2013) in the respective latest versions 8.6 – 9.5. Centaur allows the efficient generation of unstructured and hybrid meshes using CAD-files for the underlying mesh structure. With various settings the mesh quality and resolution can be controlled. Geometrical and CAD sources can be introduced to increase the resolution in specific areas in the flow field or directly on and with it close to surfaces. When the values for all of the settings are chosen, the mesh generation process is automatically performed and can be separated into three different stages. These are the generation of the surface mesh, the structured mesh on top of the surface mesh and finally the unstructured mesh which starts usually at the surface of the relatively highly resolved structured mesh.

Due to its graphical user interface, the naming of the individual geometry surfaces is achievable in a fast and simple way. Additional to that, the boundary-mapping file is stored within the mesh file and is extracted when converting the mesh file to the Network Common Data Form (netcdf)-format that is required for the flow simulation in the TAU-Code.

4.7.1.2 *Mesh Adaptation*

It is hardly possible to resolve an initial mesh ideally in a cost efficient way to sustain a converged simulation result. Therefore, a relatively coarse initial mesh is then adapted several times until it is suitable to obtain a converged, accurate physical solution. During the adaptation process the latest computed solution is used together with the mesh to determine the gradients of one or multiple user defined variables, like the gradient of the density, Mach number or the pressure, to name a few. In areas of high gradients, the node resolution is increased by adding additional cell nodes leading to additional cells. In areas with low gradients between cells, the resolution is reduced by reducing the cell number. In both cases, the old solution is interpolated on the newly generated mesh leading to a new solution that is used as re-starting basis for further computations.

Every mesh was adapted until an additional mesh adaptation was not leading to significant changes in the result. Because of the aforementioned reason, a separate mesh convergence study with different cell sizes and numbers is not needed and was not performed as each simulation was performed with the smallest necessary cell sizes.

4.7.1.3 *Graphical Visualization and Analysis Tool: Genias Graphics – Tecplot 360*

The DLR TAU-Code delivers coefficients, moments and acting forces at the end of each solution. To get an insight about the flow phenomena within the flow field, the simulation solution is displayed in a graphical way, within the powerful commercial depiction and analysis software, Tecplot 360 2010 from Genias Graphics (2013).

Tecplot allows the detailed visualisation of all computed variables that are displayed on the surface of the geometry or on extracted slices through the flow field. Additionally, values from surfaces and slices can be extracted allowing the creation of "*XY*-plots", to depict the behaviour of variables to each other. With the integration analysis function, values can be integrated over surfaces in different ways, allowing the determination of various values, like the total pressure recovery at specific slices.

4.8 CFD Mass Flow Extraction Validation

For the extraction boundary condition validation, mainly the NASA wind tunnel studies by Willis et al. performed in 1995 and by Sorensen and Smeltzer from 1968 are used. On the one side, the authors of the mentioned studies investigated the aerodynamic influence of controlled mass flow extraction on the interaction of a generated shock wave with a boundary layer. This can be understood as a fundamental validation, as boundary layer properties like its downstream height and pressure distribution are examined.

On the other side, the extraction boundary condition validation is performed against a more complex case. An axisymmetric inlet is experimentally investigated with a detailed analysis of the overall performance in terms of the compression performance, determined by the total pressure recovery, and the captured mass flow fraction.

The validation of the mass flow extraction function of the TAU-Code is also performed, to prove that the normal shock downstream of the inlet's throat can be modelled in a stabilised fashion. Additional to that, the chosen validation case shows which mass flow rate has to be extracted in the throat area, close to the required normal shock position, down- and upstream of it. That extraction stabilizes the normal shock in the flow at one position. During the stabilization process, the back-pressure, acting to the inside of the domain, from the *exit-pressure outflow* boundary condition, is increased slowly with increasing simulation time steps up to the value where the normal shock is positioned close to the throat. With this information, for future runs, it can be estimated what shock angle change can be achieved, when applying mass flow extraction. The extracted mass flow can be injected into the domain, downstream of the shock, preserving the original mass flow in the domain (instead of bleeding this extracted flow straight into the atmosphere and increasing by this the spillage mass flow).

The two validation steps performed in this section ensure that the flow phenomena close to the extraction position can be forecasted correctly. In addition, the influence of the small extraction area is measured correctly when regarding a larger geometrical setup in which the extraction boundary condition size is only a small fraction of the overall geometry dimension.

4.8.1 Flat Plate / Shock Interaction with applied Extraction

In this section, the validation of the extraction boundary condition is presented. For this, a flat plate with an extraction surface is modelled two-dimensionally with a length of 0.095 m. A shock wave is generated by a shock generator, impinging at the middle of the extraction surface (see Fig. 4.3). The position of the extraction surface is given in relation to a boundary layer thickness in the study of Willis et al. (1995). To determine the longitudinal position in the considered case, a flow over a flat plate is simulated with the flow conditions used by Willis et al. (1995), and is given in Table 4.1. The given boundary layer thickness δ is measured at 0.3 m upstream of the start of the extraction surface.

Table 4.1: Flow conditions from Willis et al. (1995)

Parameter	Value
M_{ref} [-]	2.46
v_{ref} [m/s]	726
$p_{t,0}$ [kPa]	172.4
$T_{t,0}$ [K]	292
$Re \cdot 10^{-7}$/m	1.81
δ [mm]	26.3
Extraction length [mm]	95.2

Important to note is that the extraction in the experiment is performed through a hole perforation plate with eight rows times twelve columns of holes each with a diameter of 6.35 mm with an inclination normal to the surface. If the flow through each hole would be modelled, the required mesh resolution would be very fine and detailed. This would make the computational modelling of the flow overly expensive in both time and cost. Therefore, the *actuation* boundary condition is used in the TAU-Code. It allows the setting of the velocity, density and pressure values. By these, the precise extraction mass flow rate is defined. Although holes in a plate increase the surface friction, it is not possible to define a specific skin friction value for the extraction boundary condition, which is treated as frictionless surface.

In Fig. 4.3, a schematic through the symmetry plane of the experimental setup is given. It shows the flate plate, ramp and bleed area, the shock generator above the plate and the boundary layer fence, which is 0.09 m outside of the extraction area centre (see Fig. 4.4). This ensures quasi two-dimensional flow at the middle of the bleed area by avoiding wind tunnel side wall effects falsifying the results. In region I, labelled in Fig. 4.3, the flow over the flat plate is clean, not disturbed through a shock, therefore the boundary layer is building up normally. In region II, the shock, produced by the shock generator, is disturbing the flow, leading to a redirection of the flow. The boundary layer profiles are changed by the shock. In a case without extraction a boundary layer separation upstream of the shock impinging point would be created, wheras extraction would reduce the formation of a separation. In region III, downstream of the shock impingment point and the extraction area, a measured boundary layer profile would show clearly the differences between active extraction and thus avoidance of a separation, as the boundary layer height would be smaller than in the case without extraction.

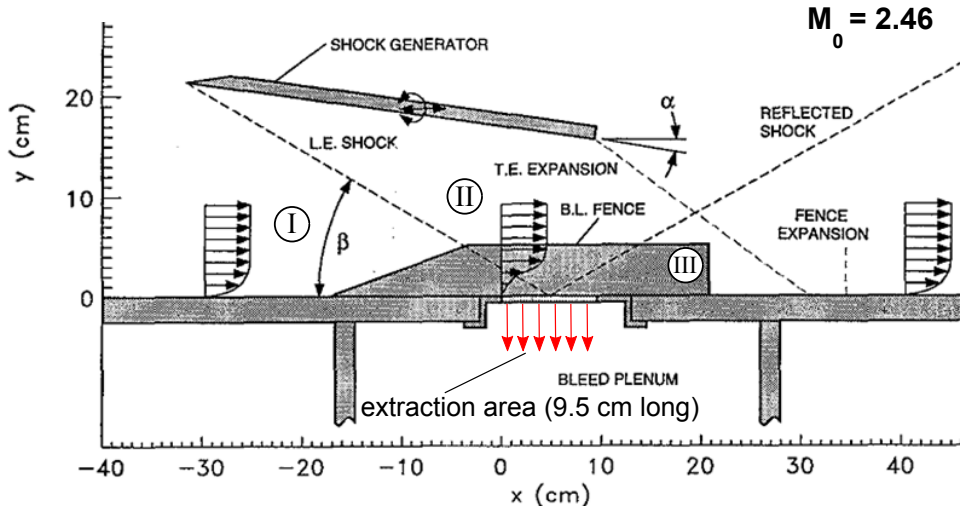

Fig. 4.3: Schematic of the experimental setup, side view (adopted from Willis et al., 1995)

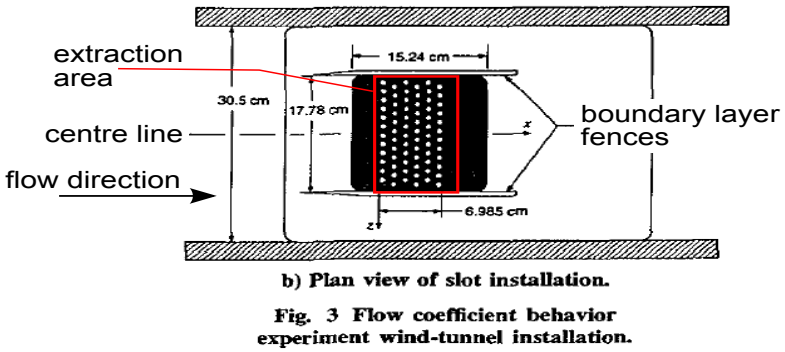

b) Plan view of slot installation.

Fig. 3 Flow coefficient behavior experiment wind-tunnel installation.

Fig. 4.4: Schematic of the experimental setup, top view of the extraction area (adopted from Willis et al., 1995)

Fig. 4.4 shows a top view close-up of the extraction area, illustrating the position of the two boundary layer fences at the side of the extraction area. As discussed above shortly, the boundary layer fences are ensuring clean flow at the centre line, where the measurements are taken, as they prevent disturbances, created at the wind tunnel sides, from falsifying the results.

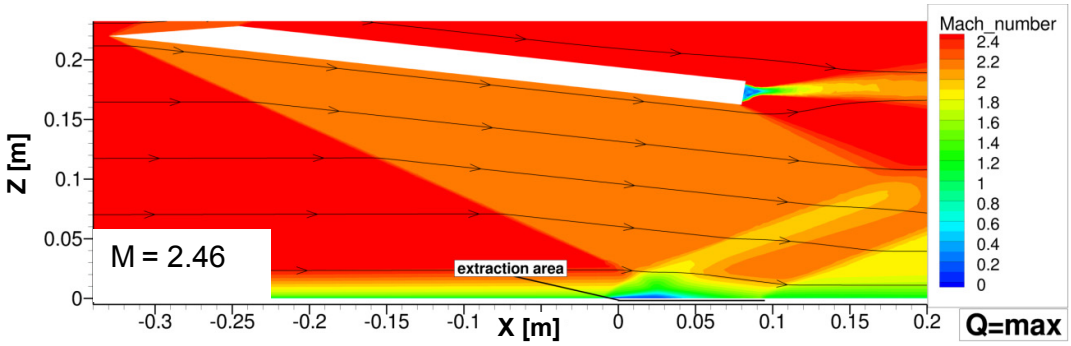

Fig. 4.5: Mach number plot of a shock wave/boundary layer interaction

The Mach number plot in Fig. 4.5 (from the TAU code) gives an overview about the two-dimensional geometrical set-up at a freestream Mach number of 2.46 and at maximum extraction settings, $Q = max$. The three different extraction settings used in the experiment and this validation are listed in Table 4.2

Table 4.2: Extraction pressure settings

Notation	Q [-]	$P_{plen}/P_{t,0}$ [-]	$\dot{m}$[kg/s]
Q=0	0	0.132	0
Q=half	0.0342	0.101	0.0442
Q=max.	0.0685	0.0321	0.0885

The dimensionless sonic flow coefficient *Q* is defined as:

$$\mathrm{Q} = \frac{\dot{\mathrm{m}}_{\mathrm{extraction}}}{\dot{\mathrm{m}}_{\mathrm{ideal,choked}}} \qquad \textbf{Eq. 4.23}$$

Where $\dot{\mathrm{m}}_{\mathrm{ideal,choked}}$ can be determined with the cross-sectional area A as:

$$\dot{\mathrm{m}}_{\mathrm{ideal,choked}} = \mathrm{A}\sqrt{\frac{\gamma}{\mathrm{R}}}\frac{\mathrm{p}_0}{\sqrt{\mathrm{T}_0}}\left(\frac{2}{\gamma+1}\right)^{\frac{\gamma+1}{\gamma-1}} \qquad \textbf{Eq. 4.24}$$

To reduce the computational complexity the 100 holes from the experiment are not modelled. Furthermore, a constant extraction is assumed for which the extraction settings have to be determined *flow coefficient Q*. The experimental cross-sectional area A is given by Willis et al. (1995) with 3.167 mm², corresponding to a porosity of the extraction area of 20 %. As p_0 and T_0 are also given (see Table 4.1), the maximum mass flow rate through the holes until choking can be calculated with Eq. 4.24, resulting in $\dot{m}_{ideal,choked} = 1.29\ kg/s$. With this knowledge, the wished flow coefficient Q and the required mass flows can be calculated. From this, the extraction pressure and density can be derived with Eq. 4.9 and Eq. 4.12 as settings for the extraction boundary condition leading to the calculated mass flow. The boundary layer at the bottom flat plate and its interaction with the impinging shock created by the shock generator can be clearly seen. As it can be gathered from the lack of a boundary layer on the shock generator, there is no need to set the shock generator wall as a viscous wall in order to obtain the simulation outcome. This is because the shock, created in the experiment at the generator is clear, without any interfering induced shocks or expansions. Therefore, the shock generator walls are allowed to be set as *Euler walls* to reduce the computational effort (as fewer cells are needed there than for viscous walls). A more detailed discussion of the occurring flow features is now given.

The shock wave generator has an inclination angle of 8° to the freestream. From the numerical solution, it is possible to measure the oblique shock wave angle, which correlates with 23.1°, to

the shock generator surface, corresponding well with the prediction given by the AMES research staff (1953). This good correlation results from the non-existing boundary layer, which would increase the oblique shock wave angle, generated at a surface with an existing boundary layer. Ames research staff (1953) published a collection of theoretically determined equations, tables and charts, which are still in use during research and design. These cover, for a perfect gas, the subsonic speed region and also predict for supersonic speeds compressible flow phenomena (like compression shock angles) with a high degree of accuracy. In all cases, continuous flow of an inviscid non-heat-conducting gas is assumed.

Fig. 4.6 highlights the good correlation of the wind tunnel study reference boundary layer upstream of the extraction surface with the boundary layer at the same position from the numerical CFD solution. The progression of the boundary layer normalised total pressure is shown versus the distance to the wall. A good correlation of the upstream boundary layers is the fundamental requirement ensuring comparability between the wind tunnel study and the numerical simulation. The difference between the experimental results, labelled as reference, and the CFD results are less than 3 %, thus the two boundary layers can be regarded as comparable, especially as the boundary layer heights are having a comparable size.

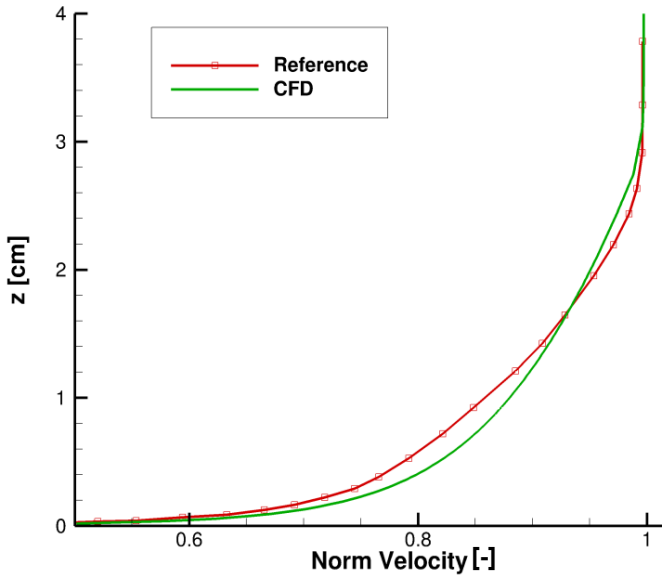

Fig. 4.6: Upstream of the interaction boundary layer height vs. normalised velocity diagram

In Fig. 4.7, the extraction boundary condition surface pressures of the experiment and the simulation are compared at three different extraction mass flows. These are the zero extraction condition, referred in the future to as $Q = 0$, the maximum possible flow, at which the experimental extraction surface choked, $Q = max$, and the third, the half of the maximum condition, $Q = half$.

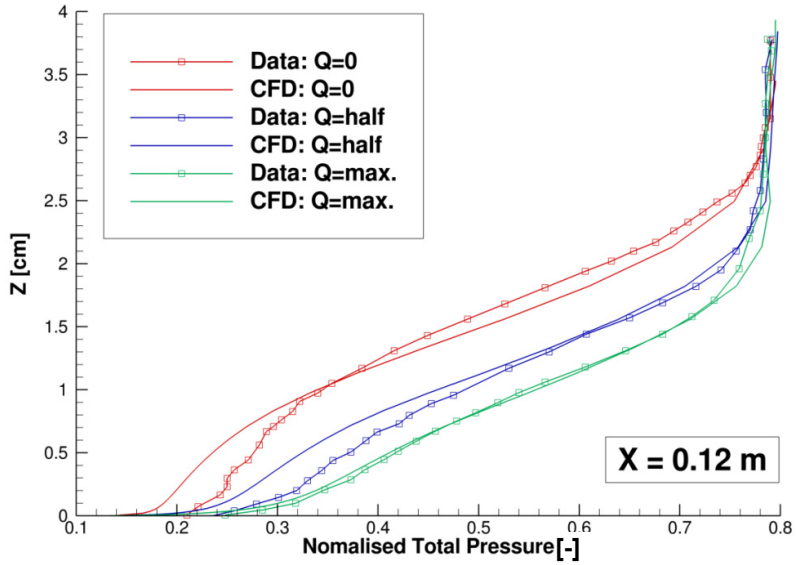

Fig. 4.7: Downstream of the interaction total pressure comparison vs. the boundary layer at different extraction mass flows

When comparing the surface pressure graphs in Fig. 4.8 with each other, a good correlation of the CFD and experimental (referred to as Data) pressure graphs can be observed. At the zero flow extraction condition, $Q = 0$, the boundary layer development of the simulation correlates well in the lower boundary layer height up to 17 mm. Whereas, there is a difference of about 3 % in the upper part but the total boundary layer height can be regarded as identical. These results document that the boundary layer height is reduced by almost 50 %, when applying mass flow extraction, in comparison to the non-controlled reference case.

Both boundary layer developments of the $Q = max$ and the $Q = half$ cases show a significantly worse correlation in the lower first ten millimetres of the boundary layer but also a lower difference in the upper heights than in the $Q = 0$ configuration. Even if the total pressure progressions in the lower boundary layer section are deviating by an error of about 20 %, the boundary layer heights of the simulation and the experiment are identical.

The difference of 20 % in the lower boundary layer may evolve from the zero surface friction of the extraction surface boundary condition, leading to a higher speed of the flow close to the surface, when comparing with the experiment, in which the extraction is done over a perforated surface. According to Eq. 4.25, the higher flow velocity leads at constant pressure to higher total pressures, which is the reason for the observed and mentioned higher pressure:

$$\mathrm{p_t} = \mathrm{p}\left(1 + \frac{\gamma - 1}{2}\,\mathrm{M}^2\right)^{\frac{\gamma}{\gamma-1}} \qquad \textbf{Eq. 4.25}$$

The surface pressure diagram in Fig. 4.8 gives a clear picture of the local influence of the extraction onto the surface pressure. In the diagram, the normalised wall surface pressure, which

is the local surface pressure divided by the static pressure at the edge of the reference boundary layer is shown against the flow direction of the simulation case with continuous data and of the experiment with single data points. The comparison between these two different sets of data can lead to misinterpretations, as the surface pressure progression between the measured data points is not clear. The extraction surface ranges from *X = 0 m* to *X = 0.095 m.*

The wall surface pressures of the $Q = 0$ cases have slightly different gradients as in the simulation the pressure starts rising with a high gradient at 5 millimetres upstream of the extraction surface. The available data does not allow the precise determination of the position where the pressure starts rising in the experiment. It is possible to determine that the pressure progressions over the surface have comparable characteristics, as the corresponding data points on the graph are approximately parallel to each other. However, in the region *X = [-0.015, 0.11]* the experimental pressure values are shifted upstream by 15 mm.

The more upstream pressure rise originates from the boundary layer separation, due to the impinging compression shock on the perforated plate further downstream. In the experimental case, the flow close to the wall is slower than in the simulation, which allows the upstream flowing flow within the separation to flow further upstream than in the numerical case.

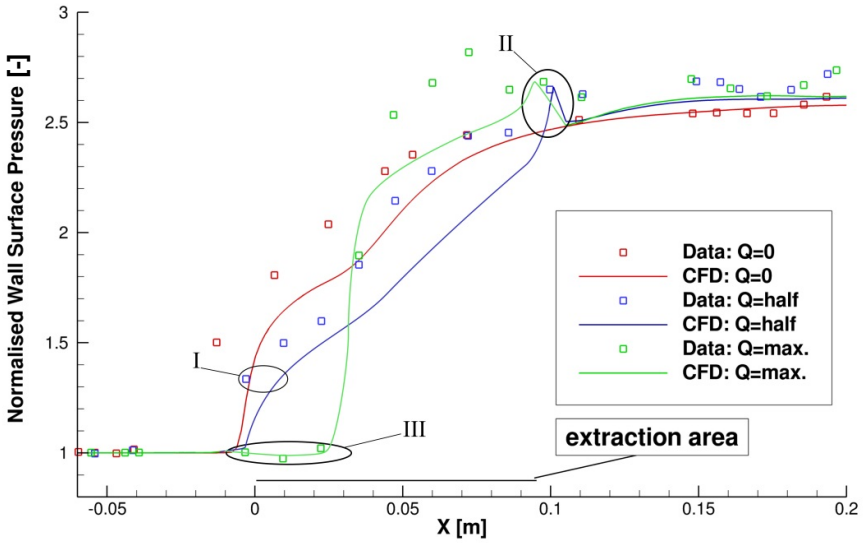

Fig. 4.8: Surface pressure plots of three different extraction mass flows

The maximum surface pressure downstream from 0.1 m is identical up to the point at *X = 0.16 m* where the influence of the reflected shock and the impinging expansion wave leads to a further increase of the pressure. This expansion wave is not existent in the simulation at the same position as the geometrical dimensions of the shock generator were not provided in detail,

therefore, assumptions have been made in the CFD run and deviances in the result cannot be avoided.

As it can be seen in the surface pressure diagram in Fig. 4.8, the progression of the simulation results for $Q = half$ and $Q = max$ are in a higher agreement with the experimental values as the $Q = 0$ case. When comparing the results of the $Q = half$ setting, the surface pressure of the numerical prediction is between *X = -0.01 m* and *X = 0.09 m* nearly 20 % lower as the value from the experiment. In the experiment, the pressure jump slightly upstream of the beginning of the extraction surface at *X = -0.03 m* is being predicted by the CFD to be 16 mm further downstream at *X = -0.19 m*, the corresponding area is highlighted in region I. CFD predicts the pressure to rise with a weaker gradient, than the experiment. Over the complete extraction surface, the numerically determined surface pressure is lower than the experimental one. The explanation for this behaviour of the graph is that the CFD is predicting a smaller boundary layer separation size, which is leading to a lower surface pressure. The surface pressure peaks of the CFD results, highlighted in region II (Fig. 4.8), are resulting from the flow that is flowing in the direction of the wall, while close to the extraction surface. Slightly downstream of the extraction surface, the flow is still flowing nearly in the direction of the wall, before it turns again parallel to it. This flow direction causes the wall pressure peaks in the cases with active extraction. In the non-regulated reference case, a pressure peak is not observed (as expected). The experimental data indicate a similar behavior.

In the case of $Q = max$, the boundary condition used is *actuation* and this leads to a good comparability of the results up to an *X*-position of 0.04 m. In region III in Fig. 4.8, the pressure values of the mass flow injection area are highlighted (see the lower plot in Fig. 4.9). At this position, the results are in good accord with each other. However, the experimental data indicates a slightly lower wall pressure at its minimum, indicating a higher mass flow injection at that point. In the experiment, the values are taken directly from the surface, which differ to the numerical values, when they are taken from shortly above the computational surface.

The Q=max case is particularly interesting, as in the CFD results there appears for the part of the extraction region, that flow coming into the domain rather than leaving it . This can be seen in the bottom of the lower picture in Fig. 4.9. Between *X = 0 m* and *X = 0.028 m* the flow vectors point inwards whereas for *X = [0.028, 0.1]* the flow is outward.

The upper plot, in Fig. 4.9, shows the flow near the extraction region for the case without any extraction. It can be seen that the speed over the plate is low, particularly around *X=0.015m*. In

the lower diagram the flow is of low speed for part of the extraction region but increases along the extraction zone, reaching sonic Mach number values around *X=0.05 m*. The velocity vectors indicate the inflow/outflow *Z*-direction-velocity (the *Z*-direction is normal to the extraction wall) and show the length of the extraction surface.

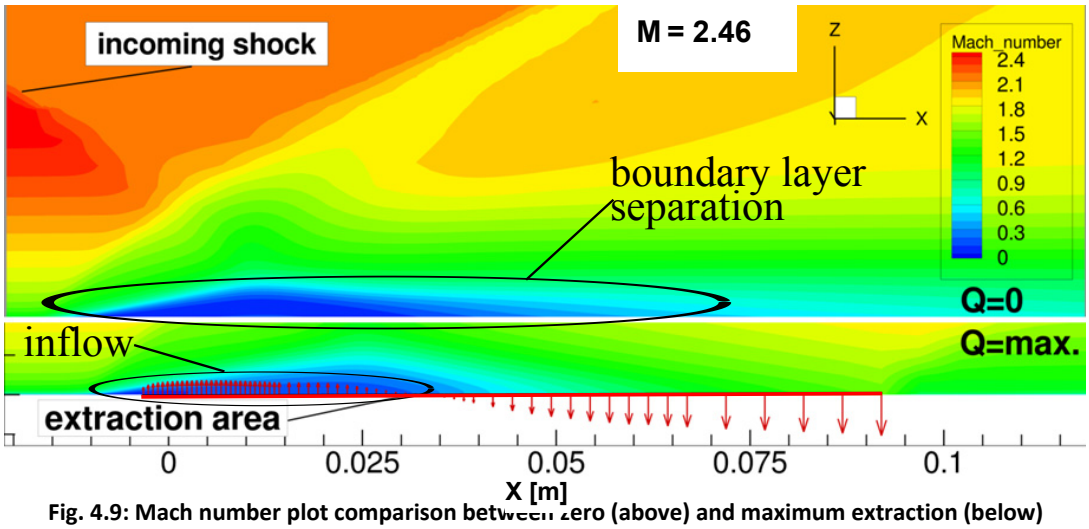

Fig. 4.9: Mach number plot comparison between zero (above) and maximum extraction (below)

The normalised surface pressure with values lower than one (see region III in Fig. 4.8) indicates that the pressure on the flow side (domain inside) is lower than the pressure on the extraction side (domain outside) leading to flow moving in the opposite direction to that intended. In the experiment both extraction set-ups lead to an overshoot of the surface pressure level with regard to the level slightly downstream of the extraction plate end. As shortly discussed above, the overshoot at the end of the extraction surface is likely to be caused by the flow that is flowing in the direction towards the extraction region, due to the flow extraction. Just downstream of the extraction region, the flow is not turning instantly parallel to the wall, therefore, as the flow is still directed towards the wall, the surface pressure downstream of the extraction region has a peak. The flow just downstream of the extraction surface end is turning away from the direction leading to the wall, parallel to the wall. The pressure maximum is located just downstream of the extraction surface but then quickly falls to a constant value. With a higher resolution of the pressure probes in the experiment, a similar behaviour would be expected to have been observed, too.

The final constant surface pressure values downstream of the extraction surface are lower in value in the simulations than in the experiments but only by 4 %. A comparable difference was also experienced by Slater and Saunders (2008) who used a different numerical extraction method in a different flow solver but achieved a well-validated method in the end. However, the differences between the experiments and the simulations can have countless reasons originating from both sides. For example, on the experimental side, small inaccuracies in the experimental

set-up, errors of measurement of the used measuring equipment and inaccuracies in the inflow conditions could lead to misinterpreted results. On the simulation side, the main sources for deviations and uncertainties in CFD are discussed in Section 4.5, but also from errors originating from the turbulence model used and from the discretization.

Despite the differences in the surface pressure diagram in Fig. 4.8, the extraction influence on the flow behaviour in the experiment and CFD are comparable. With identical pressure settings, they both lead to injection where the surface pressure is lower as the set pressure of the extraction boundary condition, thus there is injection even if it is a extraction boundary condition. Additional to that, the surface pressures downstream of the extraction region are comparable, proving equivalent influence of the numerical extraction boundary condition and the experimental perforated plate. Thus, the extraction boundary condition *actuation* is used in the following investigations for mass flow extraction.

4.8.2 Inlet-1507

It has been shown above that, the surface pressure and the boundary layer downstream of the extraction surface of the simulation and the experiment are comparable. It has to be proven that the performance parameters such as the mass flow rate and the total pressure recovery are reasonable, too. For this purpose, the 0.508 metre diameter axisymmetric Mach 3.0 inlet is numerically analysed, which was extensively investigated at NASA by Sorensen and Smeltzer in 1968. As the inlet is named in the literature after its technical memorandum number, it will be referred here also as to inlet-1507.

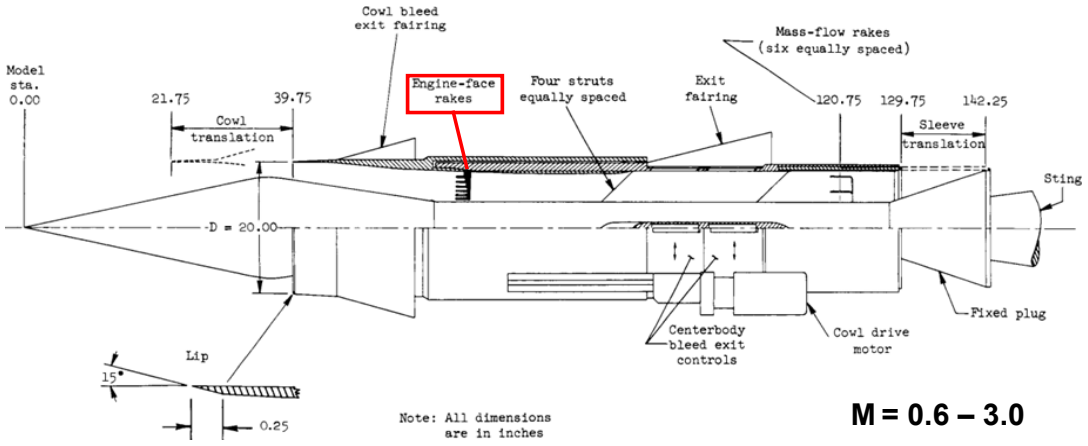

Fig. 4.10: Schematic of axisymmetric engine 1507 - view onto the symmetry plane cut (Sorensen and Smeltzer, 1968)

A schematic cut-through of the symmetry plane of engine-1507 is shown in Fig. 4.10, giving an overview of the complete engine design, the cowl translation capabilities and the individual

dimensions. However, this study is concentrating on the inlet section upstream of the highlighted engine-face rakes.

Inlet 1507 was designed to be used to investigate a relatively short high performance mixed compression inlet at different configurations and at various Mach numbers between Mach 0.6 to 3.0. In the study, bleed flow was used to reduce separation areas and to stabilise the normal shock position. Without extraction, the shock would change its position depending on perturbations in the incoming flow or through back-pressure variances in the combustion chamber. The extraction is reducing the sensitivity of the shock to such disturbances; additionally it ensures a stable normal shock position. For this validation process, the shorter of the two subsonic diffusers is chosen. Even in the experiment, vortex generators were introduced downstream of the normal shock to increase the flow uniformity at the combustor inflow plane, they are not taken into account during the quasi-three-dimensional CFD analysis as experimental performance values are also available for a configuration without vortex generators.

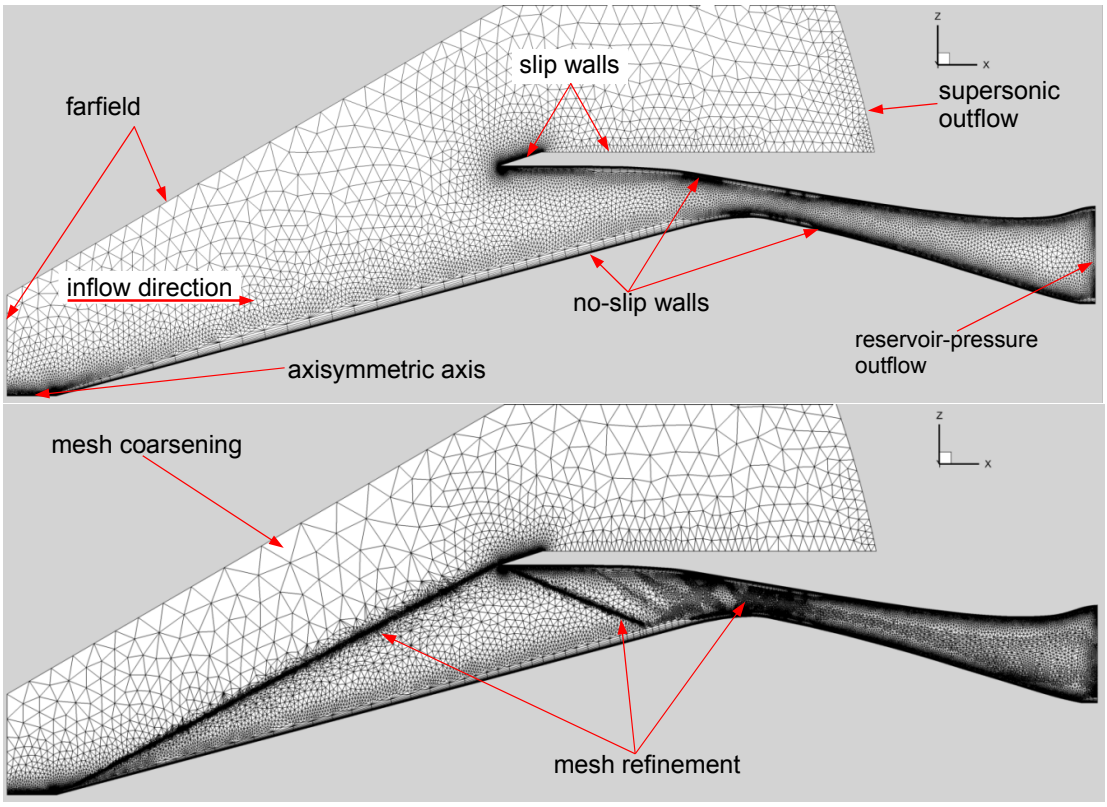

Fig. 4.11: top: initial mesh without any adaptations with 145 thousand vertices
bottom: final mesh after six adaptations with 213 thousand vertices

In Fig. 4.11, the initial mesh (top) with 140 thousand cell vertices and the final mesh (bottom) after six adaptations with 213 thousand vertices are shown. In the initial mesh, the inflow direction and the set boundary conditions are marked. In the adapted mesh, the mesh refinement

and coarsening are highlighted. In the refined areas, large density and Mach number gradients were used to identify the cells where a higher resolution would be advantageous.

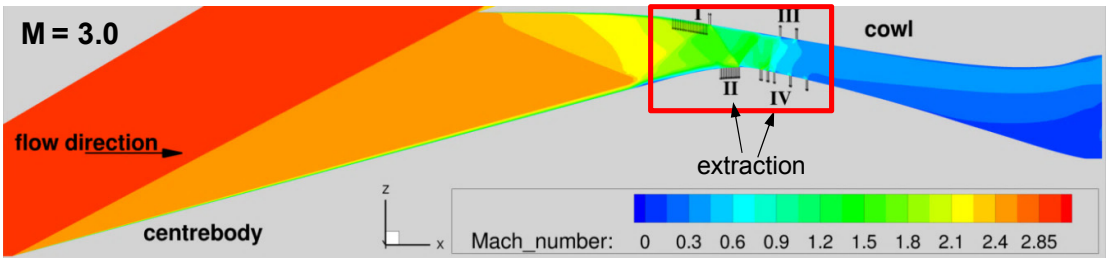

Fig. 4.12: Mach number plot of inlet-1507 with highlighted extraction surfaces and final normal shock behind throat; freestream Mach no.: M_0=3; Close-up of the indicated red box is presented in Fig. 4.13

Fig. 4.12 shows a Mach number plot of inlet-1507 at a freestream Mach number of 3.0. Additionally, in Fig. 4.13 an enlargement of the extraction and normal shock area is shown. In the three-shock inlet the cowl has an angle of 0° to the freestream flow direction and a half-cone angle of 12.5° to ensure low transonic and low cowl drag and to allow the starting of the inlet due to a low internal contraction ratio (see Section 3.2.4). The extraction surfaces I to IV are highlighted, showing every 15th uniform length vector in the *Z*-direction. Please note that only the *Z*-direction of the velocity fraction is shown at uniform length allowing to highlight the injection and extraction at extraction surface At extraction surfaces II, III and IV the flow direction is completely outward, whereas at extraction surface I the flow is mainly directed inward and only a small downstream section is directed outward, due to the low local pressure upstream of the reflected compression shock wave.

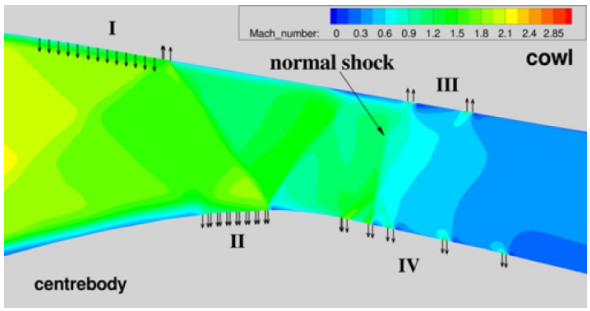

Fig. 4.13: Enlargement of the extraction and normal shock area of Fig. 4.12Fig. 4.12: Mach number plot of

The simulation is set-up as a quasi-three-dimensional axisymmetric calculation. The walls of the inlet are viscous, whereas the left and top boundaries are set as farfield. The domain right boundary is an outflow, which in the initial part of the calculation is set as a *supersonic outflow* until the simulation converges to a stable solution. Then the *exit-pressure outflow* boundary condition is applied which allows the controlling of the back-pressure and the corresponding adjustment of the normal shock position. The freestream conditions used for both inlet-1507 simulations are given in Table 4.3.

Table 4.3: Inlet-1507 free-stream conditions

Parameter	Value
M_0 [-]	3.0
v_0[m/s]	1,125
$P_{t,0}$ [kPa]	103
$T_{t,0}$ [K]	293
Re · 10^{-6}/m	6.561

The four bleed regions, which were individually controlled, are indicated with the Roman numerals I to IV (in Fig. 4.12 and Fig. 4.13). With bleed setting B, given in Table 4.4, and at a backpressure ratio of 31.76 the inlet operates in the supercritical mode with the normal shock located downstream of, but still close to, the throat. All bleed holes were circular normal to the surface with an equal porosity of 41.5 %. In bleed region I the holes had a diameter of 6.35 mm with a length-to-diameter ratio of 2.5. The holes in bleed regions II, III and IV had a diameter of 3.175 mm with a length-to-diameter ratio of 0.5. As indicated in Fig. 4.13 by the plotted flow vectors, bleed regions I and II are a continuous series of many rows of holes, whereas bleed region III and IV consist of two and five separated bleed rows respectively. Further information about the detailed geometry and experimental setup and the results is given by Sorensen and Smeltzer (1968).

Fig. 4.14 shows the normalised surface pressure against the normalised *X*-position (*X*-position divided by the inlet diameter, R). The simulation results are depicted as continuous lines whereas the experimental values are marked with the square and triangular symbols. The data show the progression in the pressure values for the centrebody (red data) and the cowl (blue data), respectively. Additionally, the geometry of the inlet is sketched on the diagram. The flow extraction positions are marked also in Fig. 4.14 (red & green straight lines, and light & dark blue dots).

When comparing the experimental with the numerical results, one can observe that the surface pressures in the regions upstream of the first bleed area on the cowl or the centrebody are in good agreement with each other. However, when comparing the values over the extraction surfaces (see the label 'cowl bleed region I'), differences become clear as the simulation values are rising more upstream than the experimental data indicates. The overshooting behaviour, which was observed above in the first part of this extraction validation (see Section 4.8.1, Fig. 4.8, region II), cannot be seen in this diagram.

The high number of shock reflections within the inlet could be the reason that the surface pressure overshoots, due to the flow directing to the wall, are being overlain by pressure increases from shock waves impinging on the surface. Another reason for the higher numerical surface pressure could lie in the implementation of the surface pressure determination over the extraction boundary condition which could lead to higher surface pressure calculations than they are in the experiment. It is noticeable that the numerical pressure over-predictions occur mainly at the continuous extraction surfaces (bleed regions I and II) and less at the pointwise extraction positions (bleed regions III and IV). Even there is a larger difference at the highlighted 'cowl bleed

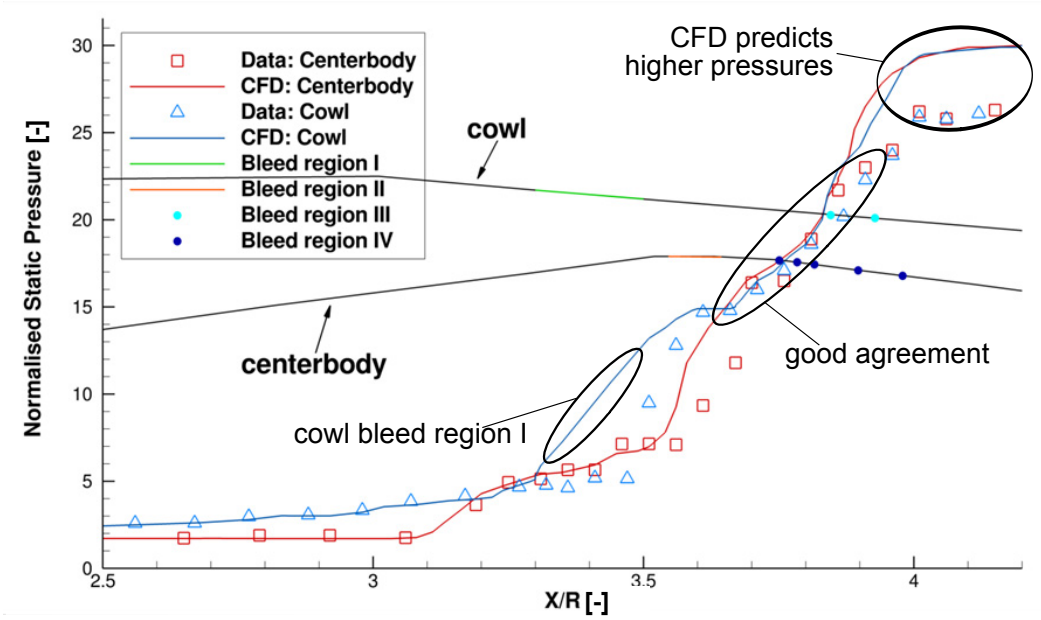

Fig. 4.14: Surface pressure plot of inlet-1507 with normalised pressure over the downstream position normalised by the cowl lip radius *X/R*

region I', the numerical prediction of the cowl surface pressure accords well with the experimental results shortly downstream of the extraction positon at an position of *X/R=3.6*. This accordance could lead to the opinion, that the presumption from above is correct, supposing that the numerical prediction of the indicated surface pressure is too high, which is not negatively influencing the CFD prediction precision of the downstream flow. In further studies, this behaviour of the extraction boundary condition should be investigated. In this study, it will be kept in mind when dealing with surface pressures.

The identical surface pressure differences, occurring at the cowl in the region *X/R=[3.3, 3.5],* occur also at the centrebody in the region *X/R=[3.5, 3.65]* leading to surface pressure over-predictions up to 45 %, which is also accepted due to the identical reasons as above discussed.

Downstream from a position of *X/R=3.9*, the CFD data is predicting 10 % higher surface pressure values than measured in the experiment. The source of this difference cannot be determined clearly with the available experimental data. However, it can be assumed that slight differences in the normal shock position and in the freestream conditions have the potential to cause such pressure differences, which occur in the comparison between these experimental and numerical data. A significant higher mesh resolution close to the normal shock position might improve the agreement between both data sets.

Table 4.4 presents experimental and CFD results for two separate configurations. In the first configuration, the bleed setting B is given with exact values by the literature and in the experiment, the inlet was equipped with a vortex generator.

In contrast to this, for the second configuration, bleed setting A was not defined with values, thus they were interpolated from the bleed setting B configuration. The second configuration was not equipped with a vortex generator. The reason for examining these two slightly different configurations is that for the first configuration surface pressure data are available, whereas the second configuration was analysed to compare the numerical results with the experimental performance values of a configuration, which was not equipped with vortex generators.

The experimental performance results are compared with the corresponding numerical results, showing that the CFD solutions (in columns 3 and 6) are close to the experimental data (in columns 2 and 4). Also the individual back-pressure ratios, $\mathbf{P_2/P_0}$, are stated.

Table 4.4: Comparison of inlet-1507 performance values at different extraction settings

Configuration	$\frac{\mathbf{p_2}}{\mathbf{p_0}}$	$\left[\frac{\dot{m}_{bl}}{\dot{m}_0}\right]_{\mathbf{data}}$	$\left[\frac{\dot{m}_{bl}}{\dot{m}_0}\right]_{\mathbf{CFD}}$	$\left[\frac{\mathbf{p_{t,2}}}{\mathbf{p_{t,0}}}\right]_{\mathbf{data}}$	$\mathbf{p_{t,2}}_{\mathbf{CFD}}$	$\left[\frac{\mathbf{p_{t,2}}}{\mathbf{p_{t,0}}}\right]_{\mathbf{CFD}}$
Exit setting: B with vortex generators	31.76	0.109	0.109	0.91	93,148	0.901
Exit setting: A without vortex generators	31.29	0.137	0.137	0.907	91,902	0.889

In the first configuration (with bleed exit setting B) the back-pressure was 31.76 times the freestream pressure so as to adjust the normal shock into the supercritical position. The extraction flow rate of each extraction surface was adjusted to the identical value as in the experiment as shown in Table 4.5 for both configurations. With the given plenum pressure ratio, the required density value, as input for the simulation setup, is calculated. With the density, a chosen temperature and velocity, the mass weighted average total pressure at the combustion chamber inflow plane, $p_{t,2}$, was 93,148 Pa, giving a total pressure recovery ratio, $\mathrm{p_{t,2}/p_{t,0}}$, of 0.901 which is 1 % lower than the experimental result.

Table 4.5: Detailed extraction surface mass flow rates and pressures

Bleed region	Bleed setting B				Bleed setting A			
	Experiment		CFD		Experiment		CFD	
	$\frac{\dot{m}_{bl}}{\dot{m}_0}$	$\frac{p_{plenum}}{p_{t,0}}$	$\frac{\dot{m}_{bl}}{\dot{m}_0}$	$\frac{p_{plenum}}{p_{t,0}}$	$\frac{\dot{m}_{bl}}{\dot{m}_0}$	$\frac{p_{plenum}}{p_{t,0}}$	$\frac{\dot{m}_{bl}}{\dot{m}_0}$	$\frac{p_{plenum}}{p_{t,0}}$
I. cowl forward	0.021	0.119	0.021	n/a	0.021	n/a	0.021	n/a
II. centrebody forward	0.018	0.15	0.018	n/a	0.018	n/a	0.018	n/a
III. cowl throat	0.023	0.105	0.023	n/a	0.033	n/a	0.033	n/a
IV. centrebody throat	0.047	0.188	0.047	n/a	0.065	n/a	0.065	n/a

In the second configuration, with extraction setting A, the back-pressure ratio was set to 31.29 for the normal shock to be supercritical positioned. With a higher total extraction mass flow rate, as in the first configuration, the total pressure recovery ratio of the simulation is with 0.889 about 2 % lower than the experimental result. As no vortex generators were present, the pressure distortions $\Delta p_{t,2}$ at the outflow plane could be compared directly with each other. The pressure distortion is often regarded as another performance parameter, which indicates how non-uniform the flow is. Uniform pressure distributions at combustion chamber inflow planes are ideal for ensuring well combustion efficiencies. With Eq. 4.26 the dimensionless quantity pressure distortion, $\Delta p_{t,2}$, can be determined:

$$\Delta p_{t,2} = \frac{p_{t,2_{max}} - p_{t,2_{min}}}{\overline{p}_{t,2}} \qquad \textbf{Eq. 4.26}$$

with $\overline{p}_{t,2}$ as the mass weighted average pressure at the combustion chamber inflow plane the pressure distortion for the second configuration is 0.1137 with is a -15 % deviation to the 0.134 distortion value of the experiment. The reason for the variation between the numerical and the experimental distortion results could lie in the numerical setup being not a three-dimensional but only a quasi-three-dimensional inlet simulation. However, the inaccuracy by 15 % has to be kept in mind when dealing with this parameter and the variation source has to be also subject to further studies in which the identical configuration has to be simulated three-dimensionally, with a significantly finer resolution, ideally in an LES simulation to resolve time-dependent vortices. The experimental pressure distortion in the first configuration with the vortex generators is reduced, in comparison to the configuration without generators, by more than the half to 0.062.

The simulation of the flat plate with the shock wave/boundary layer interaction and the axisymmetric inlet-1507 showed that the applied actuation boundary condition leads to comparable results. This is the case, when judging on the downstream boundary layer profile, the extracted mass flow rate and the total pressure recovery at the downstream end of the inlet, where the combustion chamber inflow plane is. Due to this, the *actuation* boundary condition can be regarded as validated with the mentioned restrictions in terms of the 2 % deviation in the total

pressure recovery and, with even more precaution, the 15 % in the pressure distortion. However, the sources of the deviations should be identified to understand the physics and the simulation effects fully. For this additional research is necessary, which would go beyond the scope of this project and should be done in further projects.

4.9 CFD Mass Flow Injection Validation

After the extensive validation of the mass flow extraction boundary condition, the injection boundary condition is validated. The extraction validation was undertaken by the simulation of two test cases, producing numerical results to compare with the corresponding experiments. In contrast, the following validation is of an analytical nature. This is due to the possibility to predict the exact mass flow rate when knowing or prescribing the inflow parameters. The exact mass flow rate is only met when injecting into a vacuum as the pressure is acting against the injection direction, reducing the injected mass flow. In addition, the injector sidewalls would have to be non-viscous, as the developing boundary layer would reduce the flow velocity close to the walls with the effect of reducing the overall mass flow rate. As the level of back-pressure and the thickness of the blocking boundary layer cannot be predicted exactly, one has to examine the difference between the actual and the desired injection mass flow rate.

The available boundary condition reservoir pressure inflow, allows only subsonic injection by predefining the total density, ρ_t, and the total pressure, p_t. The remaining injection parameters are determined from these independent of the flow properties on the other side of the boundary condition. If supersonic injection is required, the injector geometry has to be modelled ensuring subsonic speeds at the injection boundary condition. That follows an acceleration of the flow due to a flow-channel size-reduction, resulting in a supersonic injection speed at the throat. When using convergent-divergent nozzle geometries, injection speeds even higher than the speed of sound are possible.

In the European Union founded Sixth Framework Programmes for Research and Technological Development study, LAPCAT II, the author was investigating the ignition and combustion behaviour of supersonically injected hydrogen into a small-scale combustion chamber. As in the LAPCAT II simulations the identical injection boundary condition is used, comparable perfect gas simulations are performed and are used for the injection boundary condition validation.

The numerical and experimentally investigated combustion chamber, shown in Fig. 4.15, consisted of a rectangular flow area. The chamber walls have a width of 35.5 mm and are, for the

following 250 mm downstream of the nozzle, parallel to each other. Downstream of that section the top and bottom walls diverge with an angle of one degree. In the diverging section at an *X*-position of 275 mm, two injectors are arranged normal to the wall and located at the top and bottom walls ensuring sonic injection.

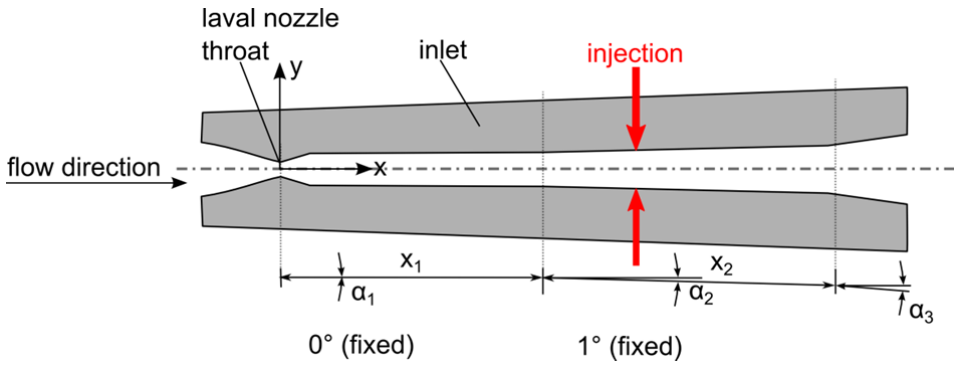

Fig. 4.15: ITLR combustion chamber geometry

For this validation, Eq. 4.27 from Karl (2011), derived from convergent-divergent nozzle theory is used to predict the flow properties. The theoretical mass flow rate, $\dot{m}_{theo}$, for flow that is injected at sonic speed, (with A^* being the throat area at which sonic conditions prevail) is determined by:

$$\dot{m}_{theo} = \left(\frac{2}{\gamma+1}\right)^{\frac{\gamma+1}{2(\gamma-1)}} p_0 A^* \sqrt{\frac{\gamma}{RT_0}} \qquad \textbf{Eq. 4.27}$$

In Fig. 4.16, the combustion chamber flow domain is shown with view onto the symmetry plane of the flat plate with a sonic normal wall injector with a radius of 5 mm. The injector geometry was modelled, as advised by the TAU-Code User Guide (DLR, 2011). A Mach number plot is shown in the figure, giving an overview about the occurring flow phenomena. Due to the symmetric flow properties along two geometric symmetry planes, it is sufficient to model and simulate only one quarter of the full geometry. The symmetry planes are defined as *axisymmetric axis* boundary condition. In Table 4.6, the freestream and the reservoir conditions used are shown.

Table 4.6: Combustion chamber freestream and reservoir conditions

Parameter	Value
M_0 [-]	2.44
v_0 [m/s]	1,239
P_t [kPa]	40.95
T_t [K]	622
ρ_t [kg/m³]	0.229

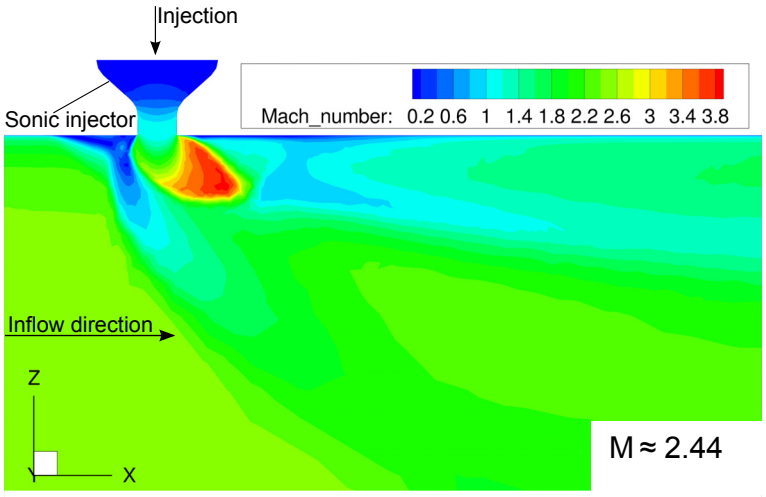

Fig. 4.16: Injection validation Mach number plot through the symmetry plane; enlargement of the injector area

Ten simulations were performed in perfect gas flow, five with non-viscous and five with viscous injection walls. The aim is to investigate the influence of the occurring boundary layer onto the injection mass flow rate.

Directly downstream of the injection, smaller boundary layer separations are formed, as shown in Fig. 4.16. These separations can be reduced by adapting the injector geometry. Added chamfered or rounded edges are leading to a more even inflow. According to Murray and Lewis (1975), these geometric adaptations have to be integrated at the intersection between the injector and the combustion chamber geometry. The influence of some injection geometry parameters will be investigated in Chapter 6. A detailed analysis of the ideal injector geometry would go beyond the scope of this research. However, the short analysis performed here will allow an estimate of the importance of an optimised injector design.

Please note that the evident coarse mesh in the combustion chamber is intentional as it reduces the computational effort and is sufficient to evaluate the mixture-ratio required to achieve combustion. The mesh resolution, both at the injection boundary and at the nozzle, is increased to resolve the influence of the injection flow onto the boundary layer and onto further occurring flow phenomena.

Table 4.7: Comparison of injection validation mass flows with non-viscous and viscous injection sidewalls

Configuration	Equivalence ratio [-]	$\dot{m}_{aim}$ [kg/s]	$\dot{m}_{result}$[kg/s]	Difference [%]
Perfect gas and non-viscous injection walls	0.15	4.209E-04	4.114E-04	-2.26
	0.2	5.613E-04	5.743E-04	-2.27
	0.25	7.016E-04	6.856E-04	-2.28
	0.3	8.419E-04	8.616E-04	-2.29
	0.35	9.822E-04	1.005E-03	-2.29
Perfect gas and viscous injection walls	0.15	4.209E-04	4.007E-04	-4.82
	0.2	5.613E-04	5.887E-04	-4.66
	0.25	7.016E-04	6.702E-04	-4.47
	0.3	8.419E-04	8.797E-04	-4.29
	0.35	9.822E-04	1.025E-03	-4.19

In Table 4.7, the expected calculated, the resulting mass flows, and the deviation between them are given for the ten investigated cases with perfect gas flow.

With Euler (inviscid) injection walls, the mass flow rate difference is nearly constant, within the considered range. When increasing the equivalence ratio from 0.15 to 0.35 the difference in the mass flow rate increases slightly from 2.26 % to 2.29 %, which is within the measuring and simulation tolerance. However, the source for the unexpected mass flow difference up to 2.29 % is not found. The non-viscous walls should lead to zero difference as no information, like the pressure within the combustion chamber can influence the boundary condition directly. Multiple reasons could lead to the found differences, whereas small differences in the used values for the gas constant or the heat capacity ratio could be one source of error. Another source may be found in the implementation of the boundary condition within the code where rounding errors could also lead to mass flow differences. Although, the mesh was refined multiple times, no further reduction in the mass flow rate could be observed, thus the mesh quality seems to be not the source for the differences. The findings of the differences will be discussed with the developers of the CFD-code to identify and solve the source of the difference. For this research study the found difference will be accepted but kept in mind during later usage of the boundary condition.

The simulations with perfect gas and viscous injection walls show a reduction of the mass flow rate difference with increasing equivalence ratio. When increasing the ratio from 0.15 to 0.35 the mass flow rate difference is reducing from 4.82 % to 4.19 %.

The results indicate that there is no significant difference in the injection mass flow rate accuracy with increasing equivalence ratio when using non-viscous walls. In contrast to that, in the case of

viscous walls it is shown that with an increasing equivalence ratio, which increases the mass flow rate and the flow velocity within the nozzle, the boundary layer effect is reduced. Therefore, lower differences between the required and the resulting mass flows can be explained when increasing the equivalence ratios. It is even possible to predict, based on the performed simulations, the rough mass flow differences for other equivalence ratio, the predictions are only valid for limited parameter combinations and only for the used and comparable geometries.

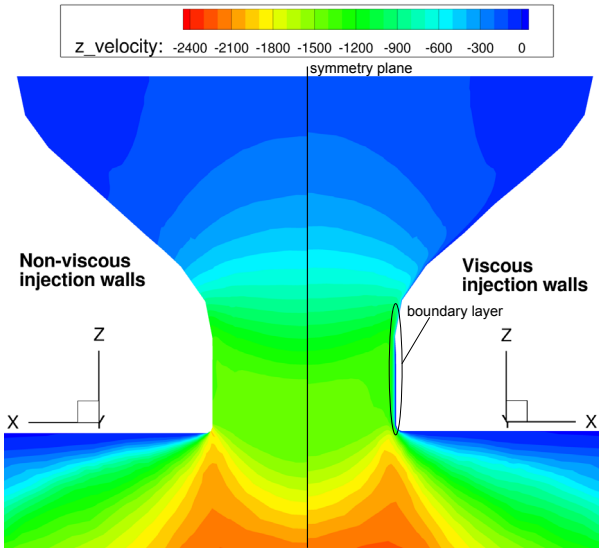

Fig. 4.17: Close-up of the injection geometry showing Z-velocity plots of the symmetry plane of the configuration with non-viscous (left) and viscous injection walls (right)

In Fig. 4.17 two *Z*-velocity plots of the injector area are shown. On the left side a mirrored half injector with non-viscous walls is shown, whereas on the right side the identical area is shown of the viscous walls, in original orientation. On the viscous wall, a thin boundary layer can be identified in the throat section. Besides the formation of the boundary layer, no large differences in the flow field are present. However, the formed boundary layer leads to the lower injection mass flow rate as it is reducing the actual injection area.

In conclusion of the mass flow injection validation, it can be stated that there exists a small difference between the required and the actual mass flow and that the differences are reduced with increased injector flow velocity. From the results, it is possible to derive, that the deviation increases, when the number of injectors is increased, while maintaining the total injection cross-section area, as this would increase the injector surface leading to increased boundary layer effects lowering the average injection velocity.

4.10 Preliminary Performance Analysis - Extraction versus Injection Shock Angle Control

Shock angle control by injection or extraction is both feasible. However, the efficiency varies significantly between the two methods. When controlling the shock angle by extracting, mass flow is extracted at a fraction of, or over the complete surface. This reduces the effective compression surface angle, which is mainly influencing the shock angle. Therefore, the flow deviation angle is also reduced by this (see Fig. 4.18).

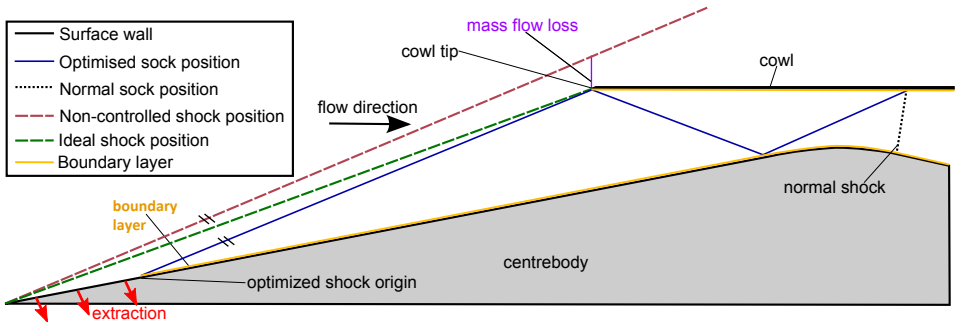

Fig. 4.18: Schematic of the extraction principle

An alternative to the extraction is the injection of mass flow. When injecting mass flow at the compression surface tip, a boundary layer thickening is produced, leading to a higher shock angle, as shown in the schematic in Fig. 4.19.

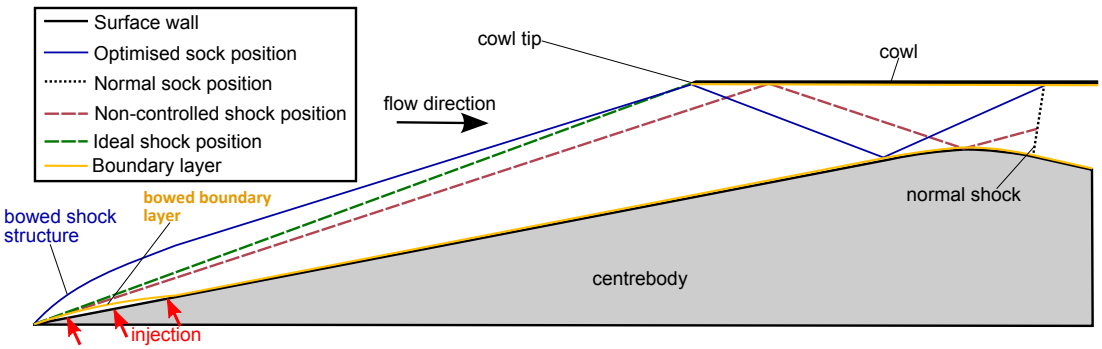

Fig. 4.19: Schematic of the injection principle

The predicted efficiency of the injection method is significantly higher than the efficiency of the extraction method (Fig. 4.18). This is reasonable, as the required mass flow, which has to be injected, is only a small fraction of the required mass flow rate when changing the angle by extraction (injection of 0.07 % leads to a shock angle increase of 3.88°, as shown below). Tan et al. (2007) injected 2 % of the captured mass flow to ensure shock-on-lip condition between Mach 5 and Mach 6.

Additional to the certainty that the mass flow rate of the injection method is smaller, the extraction of mass flow leads to further negative effects. During the extraction process, the captured air mass flow, which is available for the combustion process is reduced significantly (about 3 % for an angle reduction of 0.46°). This leads to a drastic reduction of the thrust producing capabilities of the engine, causing far-reaching efficiency reductions. These mass flow losses can only be countered when the inlet size is increased, or by compressing the extracted air in a separately driven compressor. Obviously, extraction would increase the total engine weight dramatically as an additional compressor would be required.

On the other hand, when increasing the shock angle by the injection of mass flow, only a small fraction of the captured mass flow is required to increase the shock angle. It is also feasible to use injection mass flow, which is fed, by an on-board carried tank. Then, the tank's mass would increase the inlet system weight. The use of on-board fluid for injection would reduce the demand for a larger inlet, as no mass flow is lost during injection; quite the contrary, mass flow is added with the potential to increase the produced thrust. However, carrying the injection mass flow in an on-board tank would lead then also to a big increase of the inlet system weight as the additional tank and the mass required for the injection would have to be carried.

When using mass flow from within the engine, the mass flow is preferably not taken from inside the combustion chamber because the gas temperatures are so high that the pipes used to transfer this fluid for injection would need to be cooled. As shown by Tan et al. (2007), the flow properties at the end of the inlet allow the direct use of the air for injection. The air is fed to the injection position and is used to control the injection mass flow rate by reducing the injection pressure with a pressure control valve. This would require a new inlet of slightly larger size as the mass flow (which is extracted from the inlet) is also injected, leading to a circulation of that mass flow. This argument highlights the advantages from the injection method over the extraction method. Therefore, shock angle control by mass flow injection is investigated in further detail.

Table 4.8: Extraction vs. injection simulation free-stream conditions

Parameter	Value
M_0 [-]	6.0
v_0 [m/s]	1,527
p_t [kPa]	2,000
T_t [K]	161.3
Re · 10^{-6}/m	6.0

In Table 4.9, the results of six CFD simulations are presented. In all simulations, a 7° half-cone angle was simulated at a freestream Mach number of 6. The detailed freestream conditions are given in Table 4.8. In the first case, denoted as Reference, no injection was performed at the ramp's foot point. In the injection cases, denoted as Inj.1 to Inj.5, injection was performed with the total pressure

and total density settings given in Table 4.9. For the injection validation, the boundary condition *reservoir-pressure inflow* is used.

Table 4.9: Simulation settings and results for determining the injection efficiency

	Reference values	Inj.1	Inj.2	Inj.3	Inj.4	Inj.5
$\dot{m}_{capt}$ [kg/s]	0.6409	0.6409	0.6409	0.6410	0.6411	0.6413
$\dot{m}_{inj} \cdot 10^4$ [kg/s]	0	0.637	0.985	1.48	2.82	4.46
$\dot{m}_{inj}/\dot{m}_{capt}$ [%]	0	0.01	0.015	0.023	0.044	0.07
$p_{t,\,inj}$ [Pa]	0	5,000	6,000	7,000	9,000	11,000
α (X=1m) [°]	12.10	12.86	13.41	13.93	15.00	15.99
Δα (X=1m) [°]	0	0.89	1.31	1.83	2.90	3.88
α (X=4m) [°]	12.10	12.07	12.09	12.10	12.13	12.10
Δα (X=4m) [°]	0	-0.03	-0.02	-0.01	0.03	0.00
$\frac{\Delta\alpha\ [°]}{\dot{m}_{inj}/\dot{m}_{capt}\ [\%]}$	0	8.96	8.49	7.90	6.58	5.58

The aim of this simulation is to determine a rough relation between injected mass flow rate and shock angle change (Δα) to compare the resulting injection efficiency ($\dot{m}_{inj}/\dot{m}_{capt}$) with the below discussed extraction efficiency. The shock angles (α) were measured at two X-positions at *X=1 m* and *X=4 m*, showing that the injection efficiency reduces significantly with increasing distance from the injection surface.

At *X=4 m*, the injection has, in the investigated setup, no significant effect on the shock angle, therefore the concentration lies on the measurement values at *X=1 m*. The maximum shock angle change was 3.88° with 0.07 % of secondary injected flow. This value will be taken for the purpose of comparison with the mass flow extraction.

For the evaluation of the extraction performance, the boundary condition *actuation* is used. The extraction settings, the resulting mass flows and shock angle changes are given in Table 4.10. As in the injection performance study, a 7° axisymmetric half-cone angle cone was simulated in a quasi-three-dimensional flow simulation. The injection performance study showed a significant shock angle change at a measuring position of 1 metre; therefore, the cone is shortened to a length of 1 m.

Table 4.10: Simulation settings and results for determining the extraction efficiency

	Reference	Extr.1	Extr.2	Extr.3
$\dot{m}_{extr} \cdot 10^4$ [kg/s]	0	7.56	1.91	0.477
$\dot{m}_{capt} \cdot 10^2$ [kg/s]	2.56	2.49	2.53	2.54
$\dot{m}_{extr}/\dot{m}_{capt}$ [%]	0	3.04	0.76	0.19
v_{extr} [m/s]	0	18.8	9.4	4.7
α (X=1 m) [°]	12.10	11.65	11.88	12.01
Δα (X=1 m) [°]	0	-0.46	-0.23	-0.10
$\frac{\lvert\Delta\alpha\rvert\ [°]}{\dot{m}_{extr}/\dot{m}_{capt}\ [\%]}$	0	0.15	0.30	0.51

Three simulations with different extraction settings were performed. In setting Extr.1, the complete mass flow rate is extracted, which would flow through the extraction surface as it would be an opening instead of a permeable wall. In the cases Extr.2 and Extr.3, about a quarter and a sixteenth part of the complete flow rate are extracted.

In the case were the maximum mass flow is extracted, in case Extr.1, the shock angle is reduced by 0.46° while it is extracting 3.04 % of the captured mass flow. In cases Extr.2 and Extr.3, the shock angle was reduced by only 0.23° and 0.1° while extracting 0.76 % and 0.19 % of the captured mass flow. These two cases show a higher efficiency as Extr.1, in terms of shock angle change per mass flow extraction ratio, $\frac{|\Delta\alpha|\ [°]}{\dot{m}_{extr}/\dot{m}_{capt}\ [\%]}$. Again, it can be seen that a lower angle change comes along with a higher efficiency, as seen in the performance study of the mass flow injection, too.

When comparing the two shock angle changing methods by injection and extraction with each other, it becomes clear that the injection is significantly more effective in terms of shock angle change per mass flow injection/extraction ratio. In detail, the extraction of the maximum mass flow rate leads to an angle reduction of 0.46° while extracting 3.04 % of the captured mass flow; in contrast to that, injection case Inj.5 leads to an angle increase of 3.88° with 0.07 % of injected captured mass flow.

This preliminary shock angle change performance study showed clearly the advantage of mass flow injection for shock angle change purpose, as significantly lower mass flows per change in angle is needed. In addition, the further application of the extracted mass flow is more complex as the mass flow supply in the injection case, which could be taken from within the inlet.
Thus, shock angle increase by mass flow injection is the method of choice for the further progression in this dissertation.

Summarizing this chapter, the computational fluid dynamic fundamentals are discussed, including the governing equations and a discussion about the simplifications as perfect gas flow is assumed in this studies simulations as no reacting flows or flows leading to high-temperature effects are investigated. This follows a discussion about numerical turbulence models. The Shear Stress Transport (SST) turbulence model is chosen as standard model for this study as it combines the advantages of the k-ε model in the freestream flow with the advantages of the k-ω model near solid walls. After that, the mode of operation of the used boundary conditions and the used software tools for mesh generation and adaptation and for the analysis and visualisation of the simulation results are described.

Finally, the extraction and injection boundary conditions are validated against wind tunnel studies. For the extraction validation, the extraction boundary condition is validated against two studies with increasing complexity. In the first, the extraction surface is within a flat plate with an impinging shock wave on the extraction surface. In the second study, the extraction is used to reduce the boundary layer heights at multiple positions and to stabilise a normal shock in a ramjet inlet, leading to an agreement with the data of 2 % in total pressure recovery. The validation of the injection boundary condition is performed in an analytical way, where the CFD mass flows are compared against the expected mass flows, that can be determined as the injection settings and the geometrical dimensions of the injector are known. This injection validation is leading to a deviation between the numerically determined and the expected result of 2.5 % at non-viscous injector walls and of 4.2 % at viscous injector walls. The validation showed for the extraction and the injection cases that the deviation is relative small, thus, the boundary conditions and the flow solver TAU-Code can be used for the following simulations in this research study.

In the final section of this chapter, a preliminary analysis is performed determining if shock wave angle variation through injection or extraction is more efficient. The simulations show clearly that shock wave angle increase is significantly more effective than shock wave angle reduction when rating on the change in mass flow angle per extracted/injected unit mass flow ratio.

In Chapter 5, the detailed numerical analysis of the shock angle control by injection is performed. These analyses include an evaluation of the injection efficiency mainly by means of the required injection mass flow rate over the shock angle change. This investigation leads to a preliminary understanding of the occurring flow effects when using injection to increase the shock angle, leading to the application of this method in an inlet in Chapter 6.

5 Injection Analysis

The goal of this research chapter is to stabilise the initial compression shock impingement point onto the cowl lip by controlling the compression shock angle through the injection of air at the compression ramp's base point. This, also called the shock-on-lip condition, is one requirement on the road to a high-speed inlet with maximum performance. To achieve this goal as efficiently as possible, a mass flow injection analysis is also performed. In this chapter, the effects are analysed when varying the injection parameters, total pressure and total density.

Additional to the analyses, the Mach number range in which the application of shock angle control is efficient will be discussed and a suitable inlet geometry is chosen for applying the obtained knowledge to it.

5.1 Quasi-Three-Dimensional Injection Parameter Sensitivity Study

In order to gain a preliminary feeling for the behaviour of the injection parameters, a sensitivity study is performed in this section. The focus lies on the change of the compression shock angle and not on optimising other performance parameters, like the increase of the total pressure recovery or the pressure distortion at the combustion chamber inflow plane. In Chapter 6, the influence of further injection settings is investigated, with concentration on the aforementioned performance parameters.

A one metre long axisymmetric three-dimensional cone section with a 7° half-cone angle is created, meshed so that the first structured boundary layer height is always set that a y^+ value close to $y^+ = 1$ results. In the following simulations with the TAU-Code, first small CFL-numbers around 0.01 are used until a stable convergence behaviour is recognisable, then it is increased in several steps to a value around 10. This approach ensures a stable starting of the simulation but also a fast convergence afterwards. The simulation settings are given in Tab. 5.1.

Table 5.1: Mach 6.05 wind tunnel and simulation reference conditions

Parameter	Value
M_0 [-]	6.05
v_0 [m/s]	1816
p_0 [Pa]	6873.7
T_0 [K]	224.4
ρ_0 [kg/m³]	0.1067
Re/m * 10^{-6} [-]	13.24

This study can be broken down into three groups of experiments: one group at a freestream Mach number of 6 and another group at freestream Mach 8, in both the total injection temperature

remains constant. In the third group of experiments, also at Mach 8, the injection density remains constant. During in-flight ramjet operation, in the chosen Mach number regime between Mach 6 and Mach 8, the density and the temperature of the injected mass flow are not constant. However, for this injection parameter study, constant values are assumed to ensure a good comparability of the results.

The expected shock angle for a 7° half-cone angle, at a freestream Mach number of 6, is nearly 12° (Ames, 1953) whereas at Mach 8 the shock-wave angle is expected to be 10.4°. The simulations discussed below have shock-wave angles of 12.38° in Mach 6 freestream flow and 10.55° in Mach 8 freestream flow. Both angles are higher by 0.38 and 0.15 degrees, possibly mainly resulting from viscous effects like the formation of the boundary layer and small separations, besides the numerical errors and uncertainties, like the mesh and the turbulence model used (see Section 4.3). It is also comprehensible that the differences between theory and simulation are higher in the Mach 6 case, than in the Mach 8 case, because flow at higher freestream Mach numbers over a flat plate or cone, lead to lower boundary layer heights. This is also reducing the differences between the theory and the simulation results.

Seven parameter combinations are tested in each group, giving a sum of twenty-one combinations. In both the first (see Section 5.1.1) and in the third group (Section 5.1.3) two sets of parameters are leading in each of them to supersonic inflow conditions. In the second group (Section 5.1.2), one set is leading to supersonic inflow. As the injection boundary condition is only validated for subsonic injection speeds, the five sets, which are leading to supersonic results, are neglected. Therefore, in total, sixteen parameter combinations are investigated. These injection sets lead to average inflow speeds between Mach 0.17 and Mach 0.62. This results in inflow mass flow ratios, $\dot{m}_{inj}/\dot{m}_{capt}$, between 0.5 % and 1.97 %, leading to shock angle changes up to 4.1°, where $\dot{m}_{inj}$ represents the injected mass flow rate and $\dot{m}_{capt}$ the captured mass flow rate.

The validated boundary condition reservoir pressure inflow, see Section 4.9, is used for the simulation of the injection surfaces. Total pressure and total density values have to be defined. The injection direction is optional and is set in this investigation to be perpendicular to the freestream flow, so the injected flow is at an angle of 83° from the wall, measured from the positive *X*-direction.

Fig. 5.1 shows a pressure plot with contour lines of the freestream *M=6* reference case without injection and two injection cases with total pressures of 10,000 Pa and 20,000 Pa leading to mass flow ratios, $\dot{m}_{inj}/\dot{m}_{capt}$, of 0.98 % and 1.97 %. The two pressures were set as they are leading to

a comparable mass flow ratio with which Tan et al. (2007) successfully influenced the shock structure. In Fig. 5.1, the contour lines are shown for a Mach number of 5.99 depicting the position of the compression shock.

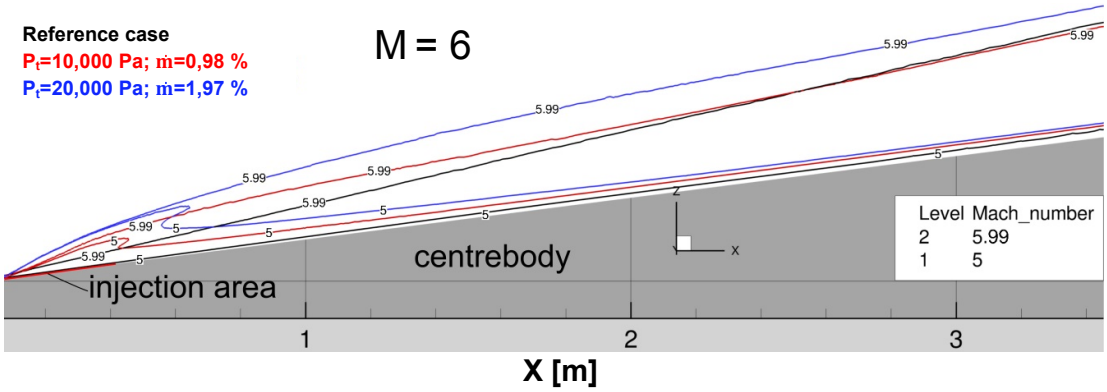

Fig. 5.1: Pressure plot of preliminary axisymmetric inlet

When regarding the injection case with a total pressure of 20,000 Pa the formation of a significantly thicker boundary layer is obvious. At an *X*-position of 0.6 m, the pressure gradient has a reversed S-shape, highlighted in the enlarged cut-out plot in Fig. 5.2. The flow injection leads directly to an increased thickening of the boundary layer, which significantly reduces its thickness at 0.6 m, at the S-shape, down to half of its former height and reduces even further with increasing distance from the injection position. The S-shape is caused by the pressure gradient, resulting from the high injection pressure, the low pressure through the expansion directly downstream of the injection, and the high pressure close to the formation of the bowed shock, generated at the inlet tip.

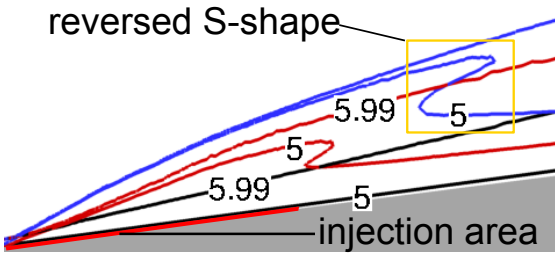

Fig. 5.2: Enlarged cut-out of Fig. 5.1 showing the Mach number contour lines close to the injection area

It is interesting to observe the dependency of the shock angle to the distance from the injection position. In non-controlled cases, the straight shock angle remains constant, independent of the distance to the compression ramp, or cone leading edge. However, when regarding the two controlled cases, the effective shock angle changes with its downstream distance from the injection position so that in such cases the shock cannot be understood as straight but more as a bow with a larger angle close to the injection point and a gradually reducing angle with increased downstream distance from the injection point.

This behaviour leads to a reduced effectiveness of the flow injection with increasing distance from the injection position. This becomes clear when regarding the shock progression of the case with a total pressure of 10,000 Pa as its shock angle is initially, close to the injection position, significantly

increased due to the injection but reduces constantly with increasing downstream distance. At a downstream distance of approximately 2.5 metres (from the injection point) the effective shock angle is identical to the non-controlled reference case as the shock contour lines intersect and thus have the identical distance between the shock and the cone surface. Resulting from this, at any position further downstream, the shock angle of the controlled case is lower than in the uncontrolled case.

5.1.1 Mach 6 Injection Analysis – With Constant Injection Temperature

In Fig. 5.3, the injected mass flow rate for the Mach 6 freestream case is shown compared with the corresponding change in the shock angle. In the simulation, the injection total temperature remains constant at 500 Kelvin, only injection total pressure and total density are varied.

The total pressure range (5,000 Pa to 11,000 Pa) is chosen due to experiences made in preliminary studies. For a parameter study, it would be ideal to have only one parameter varying per study. However, a variation in the starting values of any one of these parameters implies that only one of the total pressure, total density and total temperature can remain constant whilst the other two vary, assuming that the specific gas constant, R, remains the same. gives the wind tunnel and the simulation freestream reference conditions used. In Fig. 5.3, the applied total pressures, p_t, are presented together with the resulting injection mass flow rate, $\dot{m}_{\mathrm{inj}}$, over the shock wave angle change.

In this study the shock angle is often understood as the angle between a theoretical line from the shock origin and the position where the shock is at the cowl lip (z-)height. Therefore, the change of the shock angle is the angle difference of the actual shock angle to the shock angle of the shock impinging on the cowl lip at the inlet design Mach number. The findings of this chapter cannot be transferred directly into other inlet geometries as the shock angle change depends strongly on the distance inlet-tip-to-cowl-lip-tip and the cowl lip height.

The static pressures at the injection surfaces are at all measurement points between 273 and 308 Pa below the total pressure values. The comprehensive table, of the injection and the resulting values, is given in Table 5.2.

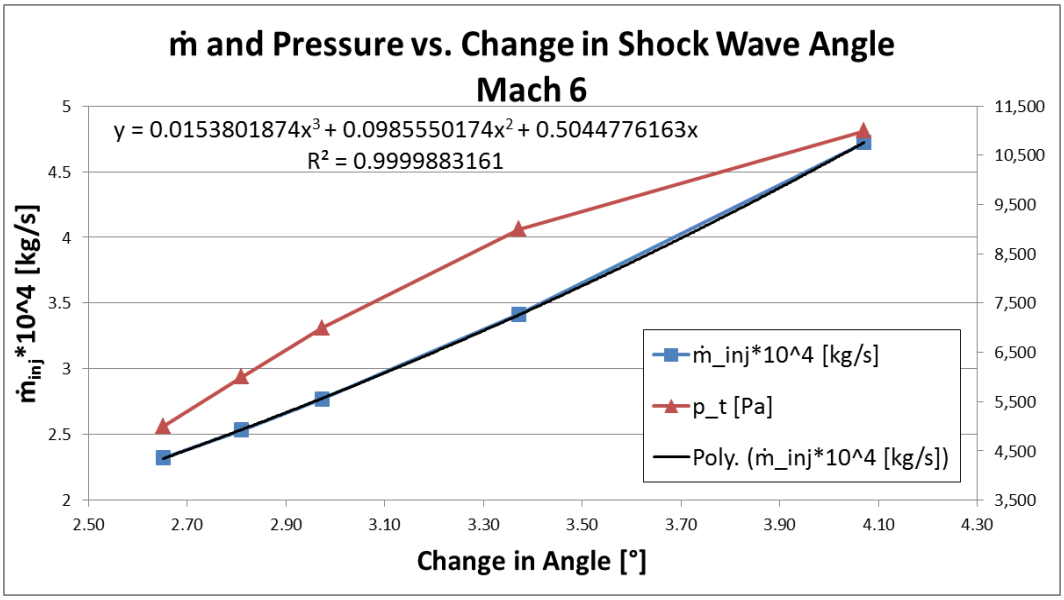

Fig. 5.3: Shock angle change in dependence of injected mass flow rate and injection pressure at *M = 6*

The results indicate a strong dependency between the applied total pressure and the shock angle change as the angle increases with increasing injected mass flow, which is increased with higher injection total pressure.

A line of best fit with an intersection point at the point of origin was included for the mass flow rate against angle of attack (Eq. 5.1). This allows the prediction by interpolation of the required injection mass flow rates, for a required shock angle change for a 7° half-cone angle geometry in a Mach 6 freestream flow:

$$\dot{m}_{inj,Mach6} = 0.0153(\Delta\beta)^3 + 0.0985(\Delta\beta)^2 + 0.5044\Delta\beta \qquad \textbf{Eq. 5.1}$$

where $\Delta\beta$ is the angle change. The coefficient of determination, R^2, at 0.999 is the best value possible for the investigated five configurations.

The former assumptions become increasingly apparent when considering Fig. 5.4, in which the injection mass fraction, $\dot{m}_{inj}/\dot{m}_{out}$, the shock angle change divided by the mass fraction and the impulse are shown over the shock angle change. The impulse is defined as mass times velocity change, whereas the mass is determined by the density of the injected mass flow times its volume.

The diagram shows clearly that a small injection mass fraction of 0.98 % is required to increase the shock angle by 2.65 degrees. This gives a ratio of 2.72 when dividing the shock angle change by the mass flow ratio in percentage. When increasing the shock angle by 4.07° the required injection mass flow ratio is 1.97 %, giving an angle change over injection mass flow ratio of 2.07, which is nearly 25 % lower than the first mentioned ratio. However, even smaller angle changes are realisable with a higher efficiency, if larger shock wave angle changes are necessary for

increasing the inlet performance, then lower efficiencies of the shock angle-change-mechanism have to be accepted.

The determination of the maximum possible angle change is of interest but not realisable with the chosen set up. The maximum angle is of interest, as it determines the application Mach number and altitude range of the alternative shock-angle control-method. For this determination, higher injection mass flows would be required, which would lead to unfavoured supersonic injection. Therefore, the geometry would have to be changed, allowing after meshing new simulations. Thus, these limits have to be determined in following studies, which are independent of this research study.

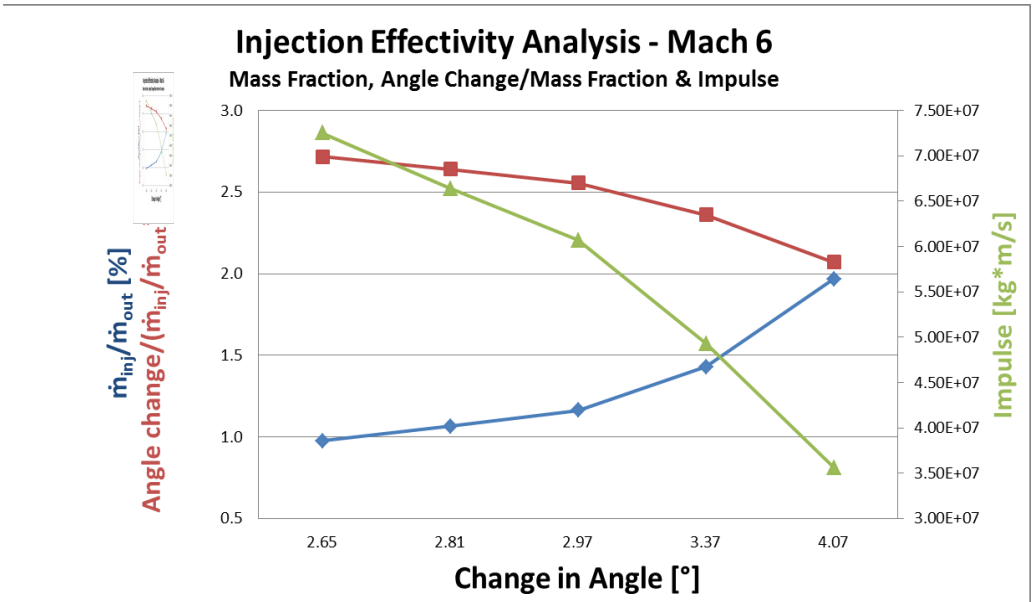

ṁ_inj/ṁ_out*100 [%]	0.98	1.06	1.16	1.43	1.97
Angle change/(ṁ_inj/ṁ_out	2.72	2.64	2.56	2.36	2.07
Impulse [kg*m/s]	7.25E+07	6.64E+07	6.07E+07	4.93E+07	3.56E+07

Fig. 5.4: Injection effectiveness analysis of mass rate fraction and injection impulse over shock angle change – Mach 6

The ratio between the shock angle change divided by the injection mass fraction and also the impulse, acting from the injection onto the flow field, are also shown in Fig. 5.4, emphasising the reduced effectiveness with increasing angle change, as the impulse and the injection Mach number are reducing continuously with increasing total pressure.

In Table 5.2, the five detailed injection parameters are listed, which are leading to subsonic outflow. Also included is the injection Mach number, which is constantly reducing with increasing total pressure. This behaviour can be explained by the corresponding increasing injection density, as the difference between the freestream and the injection densities is high and high injection Mach numbers occur. With increasing total pressure and total density the difference in the

densities reduces, leading to lower mass flows and thus to lower injection Mach numbers, required for higher changes of the shock angle.

Table 5.2: Detailed injection properties – Mach 6 with constant total temperature

Case	1	2	3	4	5
Change in Angle [°]	2.65	2.81	2.97	3.37	4.07
Mach number$_{inj}$ [-]	0.303	0.261	0.232	0.207	0.190
$\dot{m}_{inj}/\dot{m}_{out}$ [%]	0.98	1.06	1.16	1.43	1.97
p_t [Pa]	5,000	6,000	7,000	9,000	11,000
ρ_t [kg/m³]	0.0348	0.0418	0.0488	0.0627	0.0766
T_t [K]	500	500	500	500	500
p [Pa] (calc.)	4,692	5,722	6,742	8,736	10,562
ρ [kg/m³] (calc.)	0.0333	0.0404	0.0475	0.0614	0.0745
T [K] (calc.)	419.62	419.69	419.77	420.00	420.35

5.1.2 Mach 8 Injection Analysis – With Constant Injection Temperature

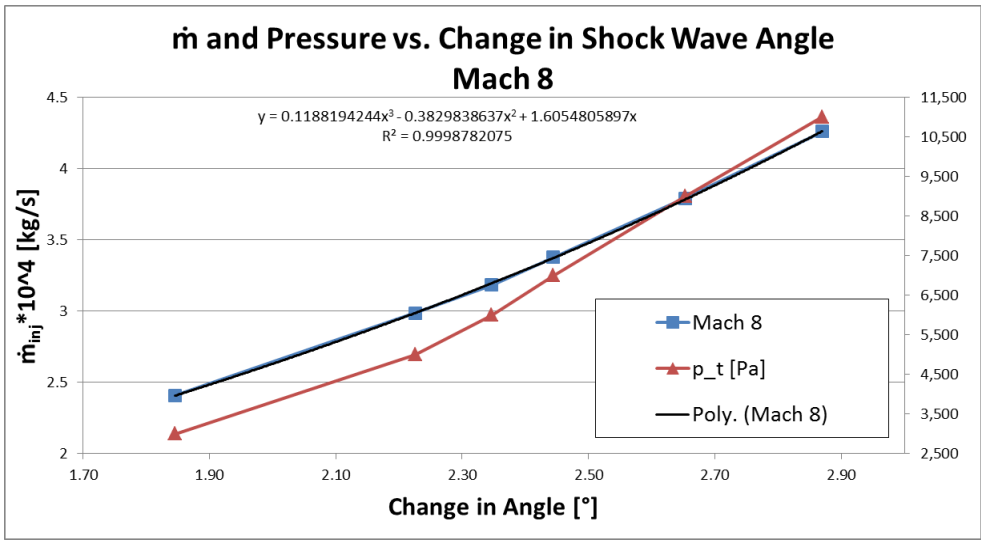

Fig. 5.5: Shock angle change in dependence of injected mass flow rate and injection pressure– Mach 8

In Fig. 5.5 and Fig. 5.6, the same diagrams as above in Section 5.1.1 are shown, but here for a cone section in a Mach 8 freestream flow, specified in Table 5.3.

Table 5.3: Mach 8 wind tunnel and simulation reference conditions

Parameter	Value
M_0 [-]	8
v_0[m/s]	1,347.54
P_0 [Pa]	327.21
T_0 [K]	70.61
ρ [kg/m³]	0.0161
Re/m · 10^{-6}	4.551

The total temperature also remains constant at 500 K in this case, thus only the total pressure and density are varied. The conclusions drawn above at the Mach 6 freestream case are also valid for this case, with the limitation that the difference between the total and the static pressure are higher in the Mach 8 case. This results from the average higher injection Mach numbers, which is also

explained by Eq. 4.25 giving the relation between the total and the static pressure in dependence of the Mach number.

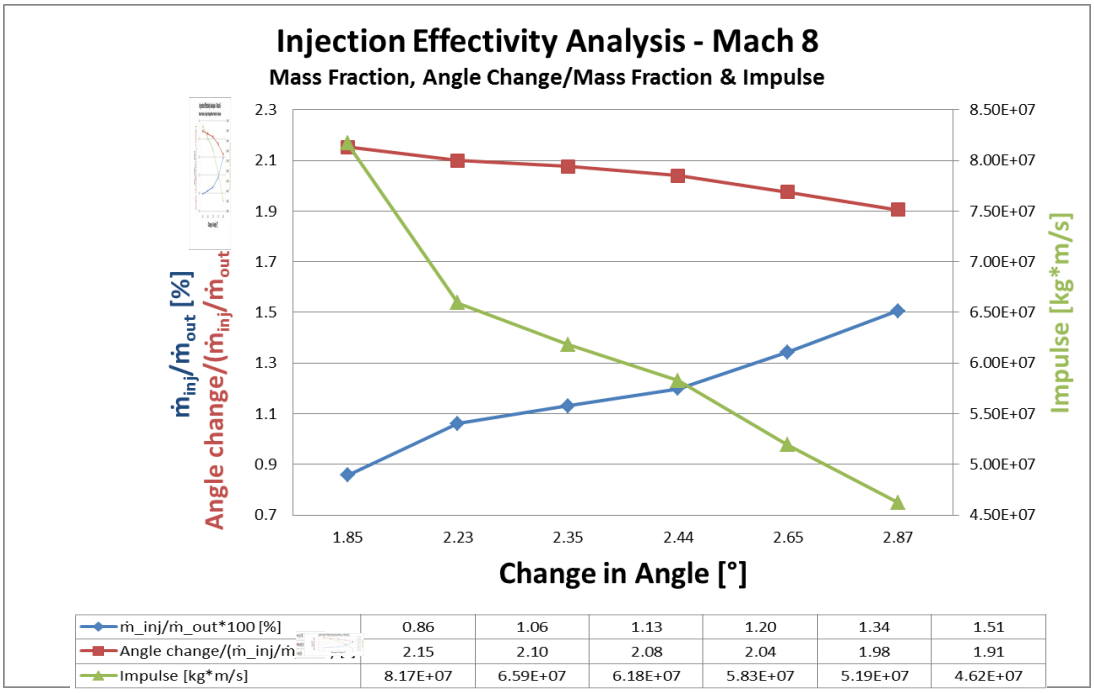

Fig. 5.6: Injection effectiveness analysis – Mach 8

Again, the strong linking between the set total pressure and the injection mass flow rate is obvious. The included line of best fit, with an intersection point at the point of origin, for the injected mass flow behaves quasi-linearly according to the following Eq. 5.2. This allows us to predict at least by interpolation and eventually by extrapolation the required injection mass flow rates for a specific angle change:

$$\dot{m}_{\mathrm{inj,Mach8,const.density}} = 0.1188\,(\Delta\beta)^3 - 0.3829\,(\Delta\beta)^2 + 1.6054\Delta\beta \qquad \textbf{Eq. 5.2}$$

The coefficient of determination, R^2, is with 0.999 the best value possible with the investigated six configuration points.

In Table 5.5, the detailed injection properties are listed for the sake of completeness. It shows also that the injection Mach number reduces with increasing total pressure and total density.

Table 5.5: Detailed injection properties – Mach 8 with constant total temperature

Case	1	2	3	4	5	6
Change in Angle [°]	1.85	2.23	2.35	2.44	2.65	2.87
M_{inj} [-]	0.62	0.42	0.37	0.33	0.26	0.23
$\dot{m}_{inj}/\dot{m}_{out}$ [%]	0.86	1.06	1.13	1.2	1.34	1.51
p_t [Pa]	17,182	17,568	17,379	17,047	16,220	15,517
ρ_t [kg/m³]	0.0174	0.0319	0.0345	0.0462	0.0606	0.0747
T_t [K]	500	500	500	500	500	500
p [Pa] (calc.)	2,314	4,427	4,579	6,495	8,580	10,617
ρ [kg/m³] (calc.)	0.0174	0.0319	0.0345	0.0462	0.0606	0.0747
T [K] (calc.)	418.48	418.76	418.83	418.83	418.94	419.08

5.1.3 Mach 8 Injection Analysis – With Constant Injection Density

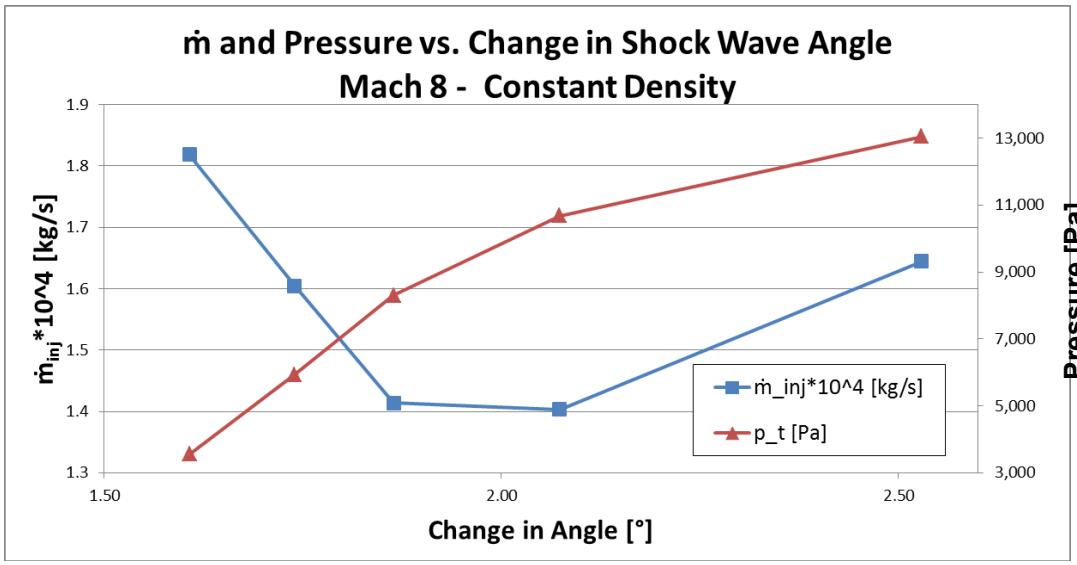

Fig. 5.7: Shock angle change in dependence of injected mass flow rate and injection pressure – Mach 8 with constant total density

The last set of diagrams in figures Fig. 5.7 and Fig. 5.8 are representing the case, in which the identical Mach 8 freestream conditions, as above in Section 5.1.2, are set but here the total density remains constant, whereas the total pressure and total temperature are changed.

In Table 5.6 the detailed injection properties are shown. The temperature and the density are increasing with increasing p_t, which is leading to strong expansions when the injected fluid is leaving the injection surface. The total density is constant but the static density rises with increasing total pressure and total temperature as the injection Mach number reduces. This density rise occurs mainly within the first three measurement points. After this, the static density rise is negligible, as the value of the total density is nearly reached. This static density rise and

stagnation are resulting, in combination with the total and static temperature rise, in the development of the mass flow injection shown in

Table 5.6 and in the diagram in Fig. 5.7.

In Fig. 5.8, the steadily increasing performance value is shown, which is the shock angle change over the injection mass flow ratio in percentage. It is possible to conclude, the higher the total pressure, total density and total temperature values are, the higher is the performance value. This indicates that for efficient shock angle change by injection, the primary impulse generated by the

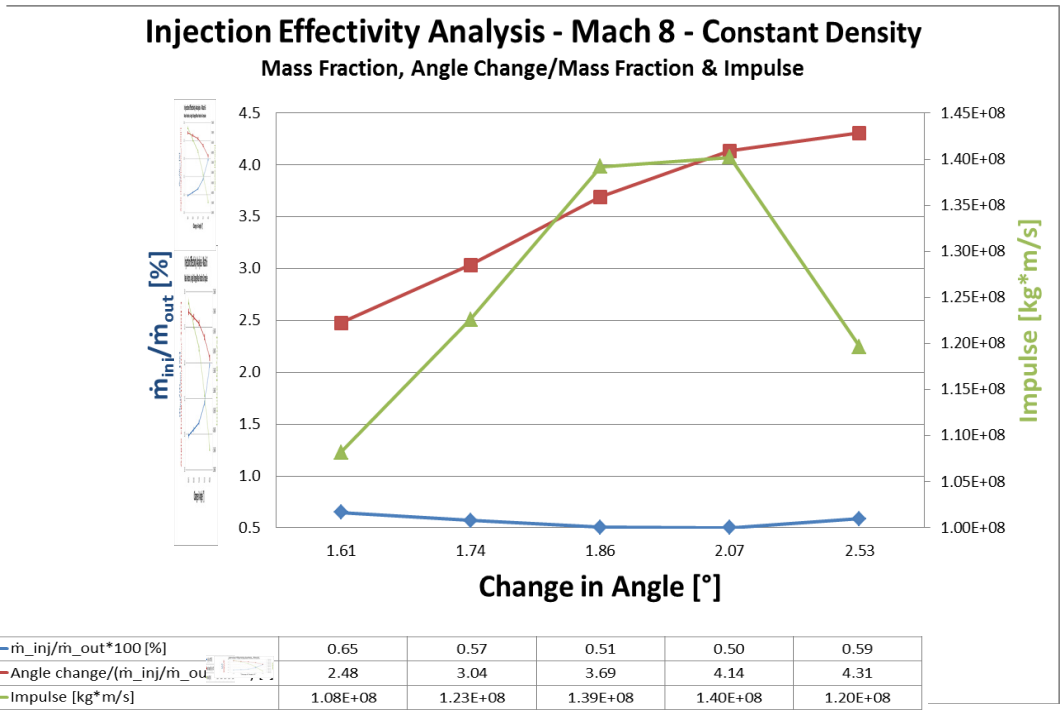

ṁ_inj/ṁ_out*100 [%]	0.65	0.57	0.51	0.50	0.59
Angle change/(ṁ_inj/ṁ_ou	2.48	3.04	3.69	4.14	4.31
Impulse [kg*m/s]	1.08E+08	1.23E+08	1.39E+08	1.40E+08	1.20E+08

Fig. 5.8: Injection effectiveness analysis – Mach 8 with constant total density

injection Mach number is significantly lower than the secondary impulse, coming from the strong expansions after the injected fluid passed the injection surface. Therefore, it is advantageous to maximise the static density and static temperature, which can be explained with Eq. 5.3 and Eq. 5.4, where a minimization of the injection Mach number, M_{inj}, leads to maximised static temperature and static density. From there follows, when maximising the static density and static temperature, the required mass flow rate for a specific shock angle change is minimised as the expansion capabilities of the injected fluid is maximised.

$$T = \left(1 + \frac{\gamma - 1}{2} M^2\right)^{-1} * T_t \qquad \textbf{Eq. 5.3}$$

$$\rho = \left(1 + \frac{\gamma - 1}{2} M^2\right)^{-\frac{1}{\gamma - 1}} * \rho_t \qquad \textbf{Eq. 5.4}$$

Table 5.6: Detailed injection properties – Mach 8 with constant total density

Case	1	2	3	4	5
Change in Angle [°]	1.61	1.74	1.86	2.07	2.53
Mach number$_{inj}$ [-]	0.547	0.348	0.245	0.186	0.175
$\dot{m}_{inj}/\dot{m}_{out}$ [%]	0.65	0.57	0.51	0.5	0.59
p_t [Pa]	3,559	5,931	8,303	10,676	13,048
ρ_t [kg/m³]	0.01357	0.01357	0.01357	0.01357	0.01357
T_t [K]	786	1,311	1,835	2,359	2,883
p [Pa] (calc.)	2,904	5,454	7,964	10,421	12,772
ρ [kg/m³] (calc.)	0.01173	0.01278	0.01317	0.01334	0.01336
T [K] (calc.)	658	1,097	1,536	1,976	2,417

5.1.4 Conclusion about the Injection Parameter Study

Analysis of the simulation data through diagrams and tables has allowed the formulation of preliminary assumptions, which are of high value for the following study. The data has also been used to provide predictive expressions for the values of the injection pressure and mass flow required to achieve a specific increase of the shock angle. This helps to understand the influence of the injection flow onto the main flow and the compression shocks.

The knowledge obtained here will be confirmed and enhanced during further studies in Chapter 6, as the influence of the injection parameters onto the inlet's performance will be investigated there in further detail.

This performance of the ramjet would not be enhanced by higher injection Mach numbers, as the trend clearly showed that low subsonic injection Mach numbers are more efficient than higher injection Mach numbers. Moreover, further increasing of the injection Mach numbers leads to supersonic injection speeds, for which the numerical boundary condition is not validated, thus using it would be an extrapolation on existing confirmed results.

When designing an injection system for shock angle increases, the injection with the lowest possible Mach number has to be favoured, as it is of higher efficiency than injecting with a higher Mach number. It can be assumed, when injecting with lower Mach numbers, that the injection area has to be larger, in comparison to injection with higher Mach numbers, to maintain the shock angle change in an identical inlet. The injection area increase ensures identical mass flow rates, while reducing the injection speed. However, due to limited amount of space inside an inlet a trade-off has to be found between a relatively large injection area and a relatively low injection Mach number, leading to a good overall inlet performance.

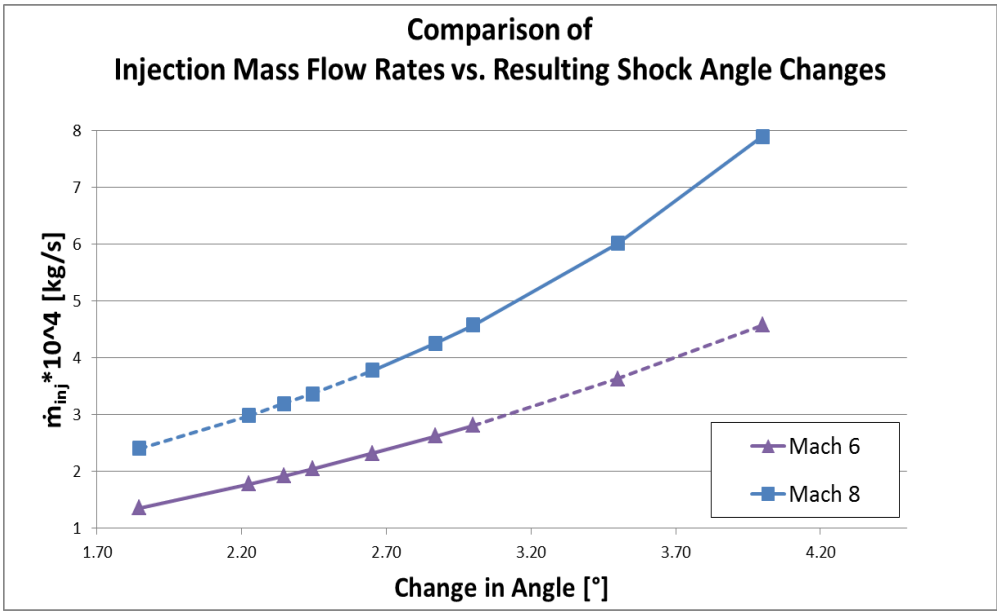

Fig. 5.9: Comparison of Mach 6 and Mach 8 injection mass flow rates against resulting shock angle change

In Fig. 5.9, the injection mass flow rate against the resulting shock angle change is shown. The solid lines represent the measured values, whereas the dashed lines are representing an extrapolation of the measured values. For the extrapolation, Eq. 5.1 and Eq. 5.2 are used for the Mach 6 and Mach 8 data extrapolation, respectively. The two graphs demonstrate, due to a comparable gradient (especially in the region with an angle change smaller than 3°), that a similar increase of the injection mass flow rate, leads to a roughly equal increase of the shock angle. From this it can be reasoned, that at other freestream Mach numbers, the change of mass flow rates is changing the shock angle in a comparable way. For this, only a few data points would have to be created, to predict the injection characteristics.

The previously created results of the Mach 6 freestream flow case show, according to NASA Ames (1953), that in the case of a Mach 4.5 axisymmetric-inlet with a 7° half-cone angle, the freestream Mach number could have been increased from about Mach 4.5 to Mach 6, whist maintaining the favoured shock-on-lip condition. From the investigated Mach 8 case, it can be followed, that the freestream Mach number of an inlet optimised for Mach 5.5 can be increased to Mach 8 with the given injection area and the identical distance between the cone tip and the cowl tip. Larger injection areas would probably allow even higher shock angle changes.

In conclusion, this study shows that the required mass flow rate to change the shock angle (to maintain the shock-on-lip condition) increases significantly with increasing shock angle changes. In addition, preliminary formulae, Eq. 5.1 and Eq. 5.2 are produced from analysing the results, predicting the required mass flow rate for a given shock angle change for the 7° half-angle cone case. This study also shows that the investigated injection leads to a resulting bent shock wave

structure, in which the effective shock angle decreases with increasing downstream distance to the injection surface.

In a ramjet inlet the cowl lip angle is designed to be equal to the angle of the shock impinging on it at the inlet design Mach number. At other Mach numbers, the angles are not identical and additional drag occurs through additional shocks or expansions. When changing the shock angle through mass flow injection, the impinging shock has a different angle to the shock at the design Mach number, leading additional drag which is not regarded in further detail.

Results from Section 5.1.3 imply that the injection Mach number should be minimised, whilst the static temperature and static density values are maximised. This ensures large expansion capabilities and results in the highest possible shock angle changes and by this, it is leading to the most efficient injection.

5.2 Determination of the Minimum Freestream Mach Number for the Efficient Application of the Shock Control Method

In Section 5.1, the approximate ratio between injected mass flow and the resulting shock angle change was discussed. That study showed that a significantly higher mass flow rate is required to increase the shock angle to every further degree (this is only true for the constant total pressures cases – the opposite is true for the constant total density case; see Section 5.1). This leads to a limitation of the efficient shock angle control range. Therefore, the minimum inlet entry Mach number has to be determined, from which the injection shock angle control method should be applied, to maintain the shock impingement point on the lip.

The propulsion system, which provides thrust from a standing position to the lowest working Mach number of the secondary propulsion system, is called the primary propulsion system, as its main purpose is the fast acceleration of the vehicle to allow the secondary propulsion system to work. The secondary system usually propels the vehicle over the largest trajectory range for which the vehicle system is designed.

The definition of the minimum Mach number is important, as it dictates the minimum efficient Mach number at which the respective inlet works under efficient conditions. This means, that the higher the minimum inlet efficiency Mach number is, the greater is the Mach number required to be reached by the primary propulsion system (often referred to as first stage). This leads to a more complex and heavier primary propulsion system (and vehicle, or to a lower pay load mass

fraction) with increasing minimum Mach number. If the minimum Mach number value is chosen too low, the effective shock angle control range is very small.

Based on these two assumptions, the minimum Mach number should be determined by the upper Mach number limit of a relatively efficient primary propulsion system. This excludes rocket engine systems, as they require carrying their oxidiser on-board, which significantly increases the total propulsion system weight, and by this reduces the efficiency of the whole vehicle, as a lower payload can be transported.

The three most promising propulsion systems are:

- A low-bypass ratio turbofan with afterburner. According to Nowicki (2004) this is capable of operating efficiently up to Mach numbers between 3.5 and 4 until the axially-symmetric compressor produces more drag than it increases the thrust through a pressure increase of the captured air.
- A turbine/constant volume combustion engine. In 2010, the American Defense Advanced Research Projects Agency (DARPA, 2010) began the second phase of the development of a full-scale turbine/constant volume combustion engine demonstrator. This engine should cover the Mach number range from zero up to about $M=4$.
- A pre-cooled turbojet-ramjet engine The Japanese Space Agency, JAXA, has been running the Hypersonic Technology Experimental vehicle (HYTEX) programme where a pre-cooled turbojet-ramjet engine capable of Mach 5 has been developed. In 2010, a first flight experiment flew successfully at Mach 2. The knowledge obtained is currently being used for further flight experiments and engine technology developments (Kobayashi et al., 2012).

Based on these promising technologies, the minimum Mach number for this study is chosen to be Mach 4. This marks a trade-off between a high minimum Mach number allowing a large shock angle control range, and using propulsion systems capable of accelerating a respective vehicle from a standing position up to the minimum Mach number, at which the secondary propulsion system, the ramjet system, can take over the thrust production.

5.3 Selection of a Suitable Experimental Inlet Geometry

As determined in Section 5.2, the minimum Mach number at which the flow control by injection starts is at a Mach number of $M=4$. Therefore, performance data of a Mach 4+ variable inlet geometry is required to evaluate the performance of an experimentally investigated variable

geometry inlet, against the performance of the numerically investigated inlet of the following studies.

The fundamental question is whether to proceed with a rectangular two-dimensional or an axisymmetric two-dimensional inlet. As discussed in Section 3.2, the rectangular inlet is easier to design and less sensitive to changes in the angle of attack, whereas the axisymmetric inlet leads to higher total pressure recoveries. When regarding the two inlet types from the numerical point-of-view, the practicability of the axisymmetric inlet is higher as occurring side wall effects in rectangular inlets are not present. Therefore, the numerical results obtained from any quasi-three-dimensional axisymmetric inlets can be scaled-up to three-dimensional inlets by maintaining the high degree of reliability of the results. This would be notably different in a rectangular inlet, in which the sidewall effects could cause separations in the corners leading to results, which are not transferrable from two- to three-dimensional, and not from small- to large-scale simulations.

The axisymmetric inlet, which is publicly best available with the most detailed documentation about the inlet and the experimental results, is NASA's Hypersonic Research Engine (HRE). The variable-geometry axisymmetric HRE was developed from 1964 to 1979. Initially the research project was focussed on a Mach 8 flight experiment of a large scale HRE mounted onto an experimental rocket propelled aircraft, the X-15A-2. The X-15 is shown in Fig. 5.10 on the ground and in Fig. 5.11 during a flight test shortly after separation from the B-51 with a mounted dummy of the HRE (highlighted in red) and two large external tanks with ablative coating.

Fig. 5.10: X-15A-2 Experimental rocket aircraft (Curry, 2002)

Due to NASA's reorganisation of its financial priorities, away from alternative high-speed propulsion systems, to a time-critical Moon mission, the continuation of the X-15 programme was cancelled. For this reason, the HRE research focus shifted away from flight tests to an extensive super- and hypersonic wind tunnel study.

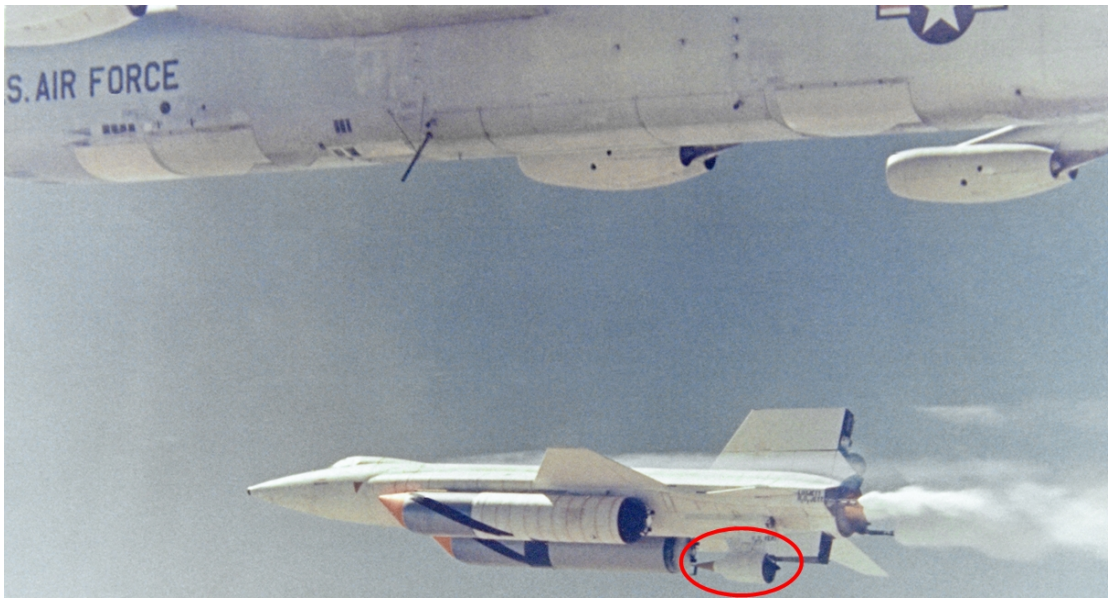

Fig. 5.11: X-15 after release from B-51 with mounted HRE dummy (Curry, 2002)

The HRE was designed to work from Mach 4 to Mach 8. The combustion is taking place at pure subsonic speeds between Mach 4 to Mach 5. Between Mach 5 and 6, the hydrogen injection positions were switched from sole combustion chamber injection to several further upstream positions, resulting in supersonic combustion. From Mach 6 to Mach 8, combustion was purely supersonic.

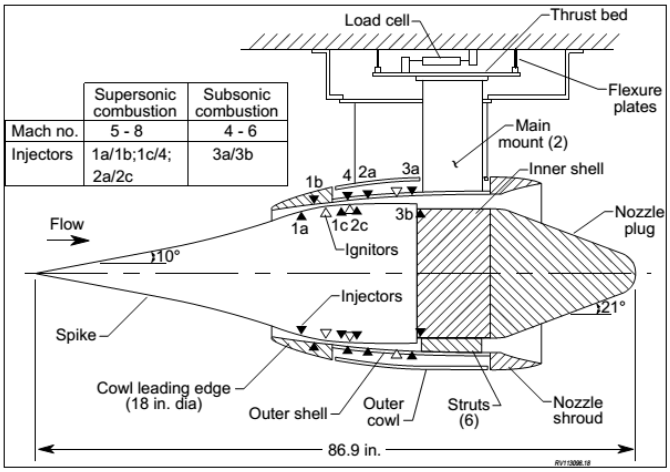

Fig. 5.12: Schematic of the HRE for wind tunnel testing (Voland et al., 1999).

As the HRE is a research engine, its performance properties cannot be compared at every working point with the performance of an engine designed to work as efficiently as possible at every trajectory point. This means that an engine for efficient flight would maintain over the complete trajectory the shock-on-lip condition to operate at a high performance. This condition is not fulfilled in the HRE inlet, shown as schematic in Fig. 5.12, between Mach 4 and 6, as its variable geometry is only capable of controlling the compression shock generated at the leading edge

between Mach 6 and 8. In the schematic, the mounting of the HRE within the wind tunnel is described, indicating the different injection locations for subsonic and for supersonic combustion. However, due to the limited availability of comprehensively documented experimental super-, or hypersonic inlets, the HRE inlet is chosen to serve as the inlet design, for evaluating the alternative shock control method. In the HRE data, pressure recoveries, pressure distortions, wall pressures and detailed geometry data are given, ensuring a broad base to compare against. The inlet description and its documentation are excellent, serving as the sound basis for the following injection analysis study. The shock control by injection will not be applied at the minimum starting Mach number of *M=4*, as determined in Section 5.2, but from Mach 6 as the variable geometry is only able to maintain the shock between Mach 6 to 8. However, the results are likely to be transferable to the lower Mach number, which could be investigated in a separate study.

The HRE inlet consists, as shown in Fig. 5.13, of three external compression half-cone angles with 10°, 15.82° and 22°. The distance from the cone tip to the cowl leading edge at 0.59 m is part of the non-controlled Mach number regime from Mach 4 to 6. This increases at a Mach number of 8 to a distance of 0.65 m due to the upstream translation of the centrebody to maintain the shock on lip condition. The cowl lip diameter is constant at 0.34 m. However, due to the 10° half-cone angle of the HRE inlet geometry, equations Eq. 5.1 and Eq. 5.2 cannot be applied to determine the necessary injection parameters, as they are only valid for a 7°-half-cone angle geometry. In general, it would be of advantage to determine the direct correlation of the injection parameters with the change of the shock angle, as in Section 5.1. However, due to the larger and more complex geometry of the HRE such an investigation would be time- and resource-consuming. Therefore, such a study could be performed within the framework of another project.

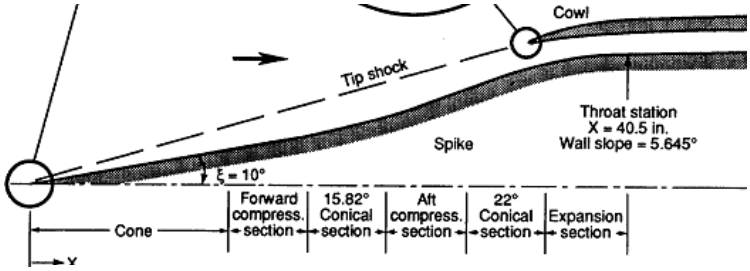

Fig. 5.13: Sketch of the HRE inlet (Pearson and Jilly, 1969)

In this chapter, it is proven that it is possible to increase the shock angle by injecting mass flow close to the tip of a compression ramp. A sensitivity study showed that small shock angle changes are more efficient then higher angle changes, in terms of injection mass flow rate to degrees shock angle changed. For a seven-degree compression ramp, at Mach numbers of six and eight, equations are determined which allow the prediction of a resulting shock angle change with a given injection mass flow rate. However, this prediction is only valid for the investigated

configurations, with changing injection geometry, freestream Mach number or compression ramp angle, the equations can only be used as a first estimate.

Additional to the sensitivity study, the minimum Mach number is determined from which a shock angle control mechanism through mass flow injection works efficiently. This determination is important as at low freestream Mach numbers the relative shock angle change per injected mass flow rate is lower than at higher freestream Mach numbers. The discussion leads to the result, that the minimum Mach number at which mass flow injection can be used efficiently is Mach 4. With this knowledge, a suitable inlet geometry is determined, that will be used for the following analyses. Based on these requirements, the variable geometry Hypersonic Research Inlet is chosen because of the large amount of available performance data between Mach 6 and Mach 8.

In the following chapters, first the Mach 6 and Mach 8 performance of the cases with shock-on-lip condition are investigated to ensure comparability between the experiments and the numerical axisymmetric solutions. After this, the Mach 6 geometry will be simulated in a Mach 8 flow with applied shock control method, ensuring that the shock impinges on the cowl lip. This controlled case will be investigated in detail with different mass flows and different injection directions. From that resulting data, an efficient injection method can be pointed out, serving as the basis for the modelling of preliminary quasi-three-dimensional injection geometry.

6 Application of Injection to Increase Shock-on-Lip range

In this chapter, NASA's axisymmetric inlet of the Hypersonic Research Engine (HRE) is investigated numerically. The aim of this chapter is to increase the shock-on-lip range with flow injection. Firstly, the clean Mach 6 and Mach 8 configuration of the inlet are simulated and analysed to compare the experimental with the numerical results and to get an impression of the inlet's critical flow phenomena.

Furthermore, in Section 6.1.3, the Mach 6 geometry is simulated in a Mach 8 freestream flow. This leads to large separations within the inlet, with dramatic effects on the inlet performance. To increase the initial shock angle, mass flow is injected close to the tip of the centrebody, which is discussed in Section 6.2.

6.1 Simulation of HRE Inlet at M=6 and M=8 without the Application of Shock Control Methods

6.1.1 Mach 6 Freestream Flow – Mach 6 Inlet Geometry

NASA's HRE inlet is simulated at a Mach number of 6.01 at a Reynolds number of 4.55 million per metre. Detailed experimental results from Pearson and Jilly (1969) are the basis for this quasi-three-dimensional CFD-investigation. The position of the cowl lip is at $X=0.5902\ m$.

The wall pressure CFD-results are shown in Fig. 6.2 for the shear stress transport (SST) and the k-ω (kw) turbulence model, which both were validated in Section 4. In addition, the theoretical and the experimental wall pressure results given as static pressure ratio values, which is the respective static pressure divided by the total pressure at the beginning of the compression ramp. The theoretical values were determined by Pearson and Jilly (1969), using the method-of-characteristics.

The experimental results were measured by wall pressure taps at seven longitudinal positions and at four different azimuthal angles (0°, 90°, 180° and 270°). In the considered case, the documented angle of attack is 0°, therefore a quasi-three-dimensional simulation, through a small stream-wise cone-piece section of the inlet is possible.

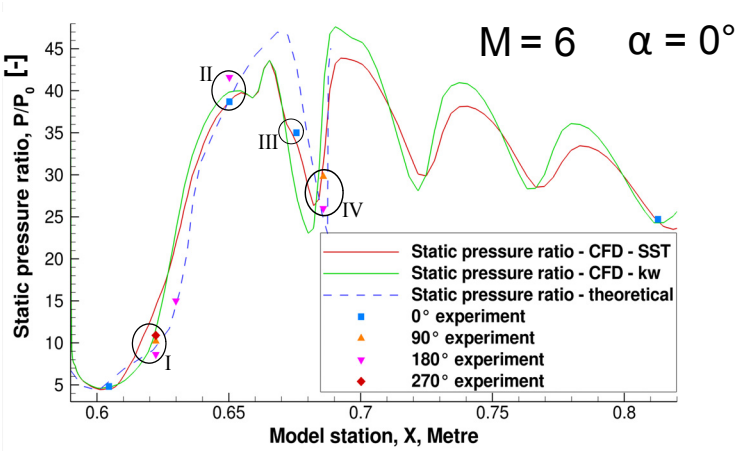

Fig. 6.2: Cowl wall pressure ratios vs. downstream position of HRE inlet at Mach 6

Interestingly, in the experiment there are up to three different pressure values for one longitudinal position indicating some degree of three-dimensional flow within the inlet, even when the chosen case is at zero degree angle of attack. As written above, in this chapter the CFD investigation is performed with a quasi-three-dimensional geometry. It allows simulating the flow around axisymmetric geometries when they are at zero angle of attack. A three-dimensional simulation would lead to the nearly identical results, though with a significantly increased numerical effort, which is often not worth the increased costs.

When comparing the CFD results with the corresponding experimental results, differences between the data sets are obvious. The position of the pressure peaks differ at most local extremes by about ten millimetres. This could arise from small changes in the shock structure, because of a small angle of attack due to non-symmetric freestream flow, when comparing the CFD with the experimental results. The exact reason cannot be reconstructed, as the experimental data and its documentation are not allowing further interpretations.

For the determination of the influence of the turbulence model, the two most commonly used turbulence models, SST and k-ω, were applied and the results are compared with each other. The position of the local static pressure ratio extremes of the SST solution, downstream of *X=0.67 m*, are shifted upstream to about 8.5 mm, when comparing with the k-ω solution. The k-ω static pressure ratio amplitude is higher, which is leading to larger boundary separations than the SST model. When evaluating CFD against the experiment, only in region I in Fig. 6.2 the k-ω turbulence model leads to a better accordance. In region III the SST model leads to better accord. In regions II and IV, both models are in comparable agreement to the experimental results.

Tian and Lu (2013) found during their investigation of nine turbulence models in 2D and 3D nozzle simulations, with mass flow injection through the sidewall of the nozzle allowing thrust vectoring,

that the *k-ε* model of Goldberg predicts the shock position well. Whereas, the one equation model of Spalart and Allmaras predicts the static wall pressure best. The SST turbulence model is leading to higher static wall pressures, which has the potential to overpredict the boundary layer separations. However, as the SST turbulence model is leading overall to a higher accordance to the experiment, its usage is confirmed again, additional to the above-mentioned intention to use it as Tan et al. (2007) also used it in their simulations, where it was leading to the most exact results. The averaged mass weighted total pressure recovery at the throat position in the experiment is 0.445 (0.456 at 0° and 0.434 at 90° - which is a difference of 5 %), whereas with the k-ω model in CFD an averaged mass weighted pressure recovery of 0.462 is determined. The numerically determined recovery is 3.7 % higher than the experimental value. However, this relatively small deviation is accepted at this point especially as there is a 5 % deviation in the experiment at two different angular measurement positions.

For the determination of the numerically averaged mass weighted total pressure recovery, it is essential that the mass weighted total pressure values are measured at the exact positions as they were measured in the experiment. In the experiment, pressure rakes were used to determine the pressure at eight positions at the throat. Four measurements were taken on the cowl rake and four were taken by the centrebody rake. The eight wall distances for the measurements from the cowl and the centrebody wall were identical with 0.73 mm, 1.45 mm, 2.18 mm and 2.91 mm. When determining the averaged mass weighted total pressure recovery by averaging not only the values determined at the given eight positions but at 500 equally distributed positions at the identical X-position, apparently the low total pressure values in the boundary layer lower the result significantly to a total pressure recovery value of only 0.394. This 15 % deviation between the two measurement methods highlights the sensitivity of the pressure recovery values and the position where they are measured. With this high sensitivity, variations in the flow like differences in the shock position and boundary layer thickness are influencing the total pressure values and thus the total pressure recovery significantly. This sensitivity and small deviations, resulting in a given degree of uncertainty, have to be accepted when comparing the experiment with the numerical simulation.

In only one other research study from Boon and Hillier (2006), the HRE inlet is numerically investigated in the identical speed regime on which the research focus of this investigation lies. They experienced comparable differences between their numerical and the experimental results from NASA. Fig. 6.3 shows the numerical results of Boon and Hillier (2006) together with the experimental values and the results of the SST-turbulence model CFD study (denoted as Buanga – turbulent). The diagram shows the cowl wall pressures in the area close to the cowl tip, having an

X-position of 0.5913 m. Boon and Hillier's inviscid results lead to the overall lowest wall pressure. The inviscid prediction at the cowl lip, at 0.85 m, agrees well with the results of their turbulent simulation and the author's turbulent simulation results. However, the second local maximum at 0.95 m indicates an overshoot in the inviscid result.

When comparing Boon and Hillier's (2006) turbulent results with the author's results, the agreement up to 0.94 m is both qualitatively and quantitatively close. Upstream of this, the author's results indicate pressures, which are significantly higher than the published paper's results. As they are 13 % higher than the experimental results, they are in an acceptable regime when regarding the large pressure differences in the experiment at other X-positions (the results follow the behaviour of the experimental measurements far closer than Boon and Hillier's results). At an X-position of 1.02 m the wall pressure ratio predicted by the author is 0.017 higher than the experimental value of 0.014 (interpolated). Downstream of *X=1.03 m*, up to *X=1.055 m*, the predicted values are at 0.027 more than twice the experimental values at 0.012. One explanation could be that there is a different shock structure within the inlet, which is producing different shock wave/boundary layer interactions downstream. This would maintain the shock position and with it the pressure peak at a comparable position by changing the peaks' heights. However, this assumption does not explain the large differences between the measured pressure at about 1.05 m and the corresponding pressure ratio of the simulation and should be investigated deeper in another study.

Differences occur between Boon and Hillier's (2006) and the author's results. They may be caused by different settings in the numerical set-up. For example, on the one hand, Boon and Hillier used a structured mesh and a *k-ω* turbulence model. On the other hand, the author used for his best results a several times refined hybrid structured/unstructured mesh with the SST-turbulence model.

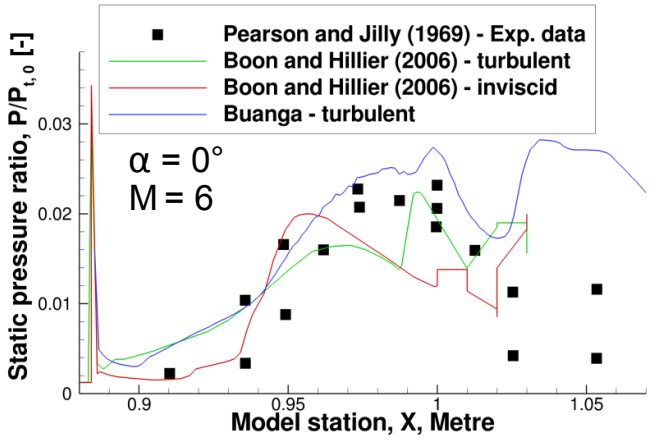

Fig. 6.3: Comparison with other CFD results – static pressure vs. downstream station

Summarising this simulation, the total pressure recovery between the experiment and the conducted numerical simulation are comparable, even the wall pressures tend to be on average higher than the experimentally determined values. The experimental results give no explicit value but up to three different ratio values at one axial station, indicating a high degree of three-dimensional flow inside the inlet and a high sensitivity of the total pressure recovery measuring method, making the interpretation of numerical results complicated. These asymmetric results also indicate potential deviations in the alignment of the wind tunnel model during the experimental set-up, or perturbances in the flow approaching the model.

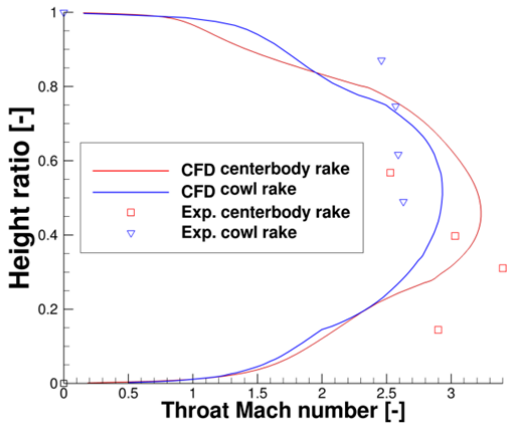

Fig. 6.5: M8 throat Mach number vs. height ratio

6.1.2 Mach 8 Freestream Flow – Mach 8 Inlet Geometry

In this section, the simulation of the Mach 8 geometry, with the cowl tip at an axial position of 0.6238 m downstream of the centrebody tip, at a freestream Mach number of Mach 8 and at 0° angle of attack, is being discussed. Due to the position of the cowl, the initial compression shock misses the cowl tip on the outside of the inlet, as can be seen in Fig. 6.4. Due to a reflection at the inner cowl wall a separation occurs on the centrebody surface downstream of the cowl tip.

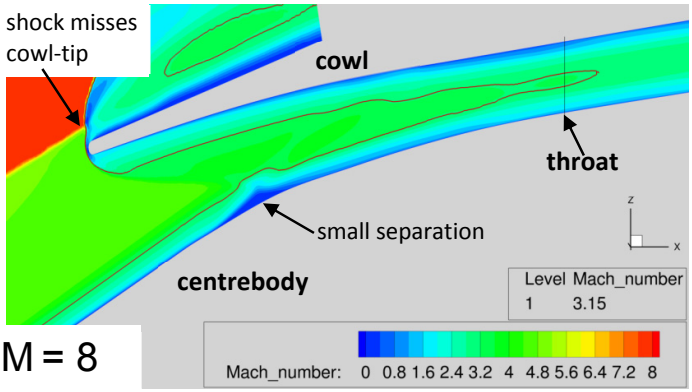

Fig. 6.4: Mach 8 freestream flow at Mach 8 inlet geometry

In Fig. 6.4, it can be estimated that the position of the maximum Mach number at the throat is slightly below the channel middle at a height ratio of about 0.48, whereas the height ratio is the normalised height measured verticals upwards from the centrebody to the cowl. This position is verified in the diagram in Fig. 6.5, in which the throat Mach number is shown against the channel height ratio. In the diagram, the CFD results are shown with the experimental results. The results of the centrebody are taken at the throat position (*X=0.6858 m*) and the cowl data from 36.6 mm downstream of the throat (*X=0.7224 m*). The centrebody rake was equipped with four pressure and three temperature probes; whereas the cowl rake was equipped with four pressure probes.

The experimental results indicate clearly that the maximum Mach number position is at a significantly lower position, around a height ratio of 0.35. However, the centrebody rake CFD result at the throat position indicates the maximum is closer to the channel middle at a ratio of 0.46. The maximum Mach number values correlates well with a difference of 4.6 %.

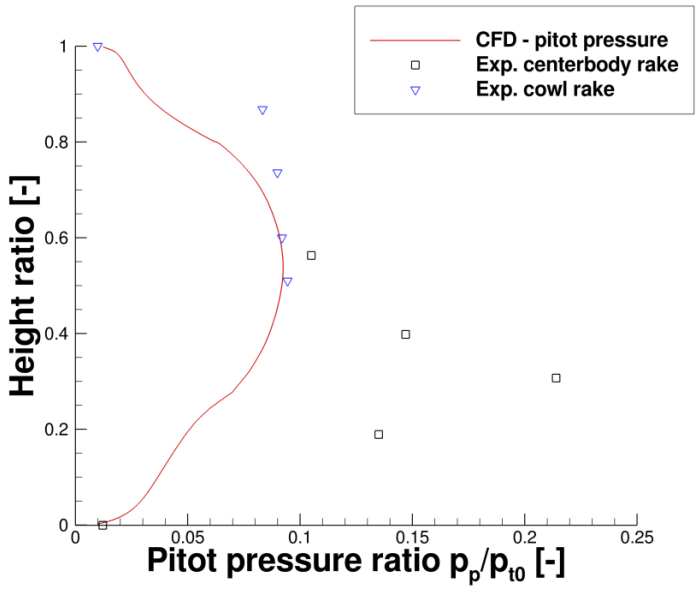

Fig. 6.6: Mach 8 throat pitot pressure ratio comparison vs. throat height ratio

The highlighted difference, in the maximum throat Mach number position, is not the sole discrepancy between the experimental and the numerical results. In Fig. 6.6, the pitot pressure ratio of the experiment and the numerical simulation are shown against the height ratio. The pitot pressure ratio is defined as the respective pitot pressure divided by the freestream total pressure. Two of the three pressure rakes are mounted at an angle of 90°, behind each other, and a third rake is mounted at the centrebody at an angle of 90° determining the three-dimensional uniformity of the flow. Again, there is a large difference between the height ratio positions of the maximum pressure ratio values. At the height ratio of 0.5, the numerical result has its pressure maximum and agrees within small tolerances with the experimental values. However, the experimental maximum pitot pressure in the throat is with a ratio of 0.214, at a height ratio of 0.31, at a position significantly closer to the centrebody and more than twice the pressure ratio of the CFD solution.

Pearson and Jilly (1969), the authors of the experimental study, were not able to explain the high degree of asymmetry in their results but mentioned that the cowl rake might be in the wake of the centrebody, with the potential of falsifying the results. However, they questioned also the proper working of their lower three centrebody pressure rake probes but further investigations showed that these probes were working, within the tolerances specified by the manufacturer. In

the end, they accepted that they could not find a definitive explanation for their results and advised that additional studies should be performed with pressure rakes at more than the two angular positions to determine the source of the asymmetric flow behaviour. As Pearson and Jilly (1969) have not specified in detail their total pressure determination, further uncertainties exist, like a possible small asymmetry in the experiment, resulting in different shock structure and different velocities, which is not modelled in CFD. The uncertainties are leading to a limited force of expression of the stated total pressure recoveries, when comparing to the current CFD simulations.

As mentioned in Section 6.1.1, two pressure rakes were used to determine the flow properties at the throat section (centrebody rake) and slightly downstream of it (cowl rake). Both rakes were mounted at an angle of 90°. A third rake was mounted at the centrebody at 0° angle to determine the three-dimensional uniformity of the flow.

As the experiment was performed at 0° AoA, one should expect axisymmetric flow behaviour, which is in this investigation not the case, as mentioned above in Section 6.1.1. When comparing the calculated mass flow averaged pressure recoveries at the two rake positions the high degree of asymmetry is visible. The total pressure recovery at zero angular angle, $\eta_{0°}$, is 0.363 considerably lower than $\eta_{90°}$ with a recovery of 0.526. The average value, $\eta_{ave,}$ of 0.444 cannot be taken as the reference when validating numerical simulations against that discussed experiment, as the discrepancies are too large. The numerically determined averaged mass weighted total pressure recovery, which is with 0.426 about 4 % under the experimental average but within the wide range of the experimental values. In section 6.1.1, the CFD total pressure recovery is 3.7 % higher than the experiment. Based on the two deviations of the CFD determined total pressure recovery in different directions, on higher and one lower of the experiment, it is not possible to formulate that all future numerical results are slightly lower or higher than the experiment. However, so far it can be formulated that the numerical results are in a range of ±5 % to the experimental result.

Therefore, the experimental values are used as guidance, offering a frame in which the numerical results should lie. The code is widely validated and the simulation of this Mach 8 case served the aim to retrieve the differences between the numerical and experimental investigation. However, as the reasons for the large differences within the experimental investigation are not explainable, it is the most productive way to continue, but further studies should concentrate on the tracing of these so far unexplainable asymmetric behaviours. A way to ensure that occurring vortices and their behaviour over time can be explicitly resolved in numerical simulations is the usage of a time

dependent method, like LES. This would then allow the visualisation and evaluation of time-dependent effects, like occurring vortices. The usage of a time-dependent method is only advantageous when important time-dependent flow effects are occurring and the usage of an averaging method is not sufficient. On the one hand, the differences between the numerical and experimental results in Fig. 6.6 should be analysed with a time-dependent method to determine if time-dependent phenomena occur. On the other side, it is just as important to understand and evaluate the flow in the experimental inlet completely to exclude other possible error sources, which could have led to asymmetric flow.

6.1.3 Mach 8 Freestream Flow – Mach 6 Inlet Geometry

In the previously presented results, the geometries designed for Mach 6 and Mach 8 were analysed in their respective freestream flows, Mach 6 and Mach 8. This leads to high inlet performance as the flow capture ratio and the pressure recoveries are maximised, as the shock impinges in both cases on the cowl lip.

In the following part, various effects are shown occurring in an inlet that is designed for Mach 6, but is in a Mach 8 freestream flow. In Fig. 6.7 an enlarged Mach number plot, including streamlines of the cowl area, is shown.

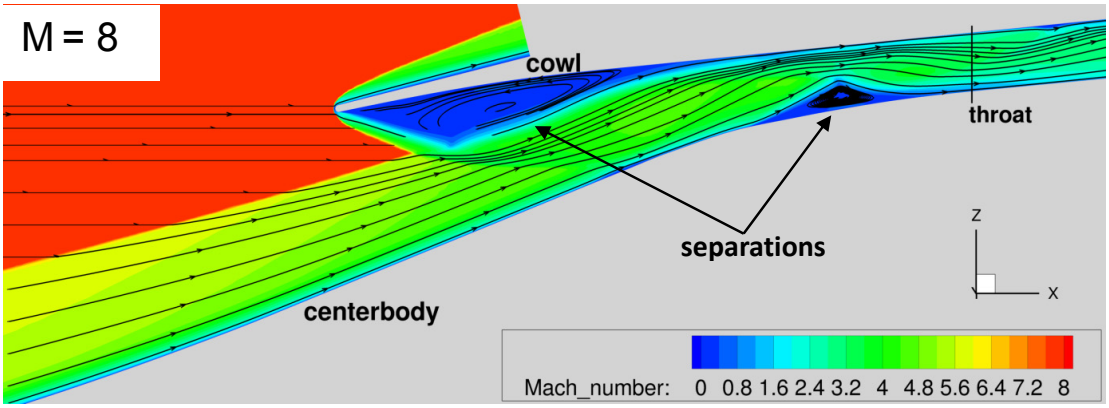

Fig. 6.7: Mach 8 freestream flow at Mach 6 geometry showing occurring separations in a Mach number plot – detail cut-out of cowl and throat area

As can be seen, the oblique compression shock generated at the centrebody tip is entering the inlet internal channel. The large adverse pressure gradient, from the shock impinging on the inner upper flow channel wall, results in the major upstream separation bubble. The shock is reflected at the upper wall and impinges on the lower surface, leading to a second separation bubble upstream of the impingement point. Below in Fig. 6.8, the red streamlines are indicating the two occurring large separations. The initial shock and its reflections are shown here in a density

contour line plot. The second separation lies close to the geometric inlet throat on the centrebody. This separation leads, as well as the first one, to an effective flow channel reduction, in the regarded case as 60 % of the geometrical throat.

The cause for the large first and second separation areas is the strong initial shock, which is ideally impinging on the cowl lip tip, leading to zero loss in captured air and establishing the first requirement to a high pressure recovery. The averaged mass weighted pressure recovery at the throat is 27.6 %, which is 18.6 % lower than the recovery in the former investigated case, where the freestream Mach number is appropriate to the designed Mach 6 geometry, see Section 6.1.2.

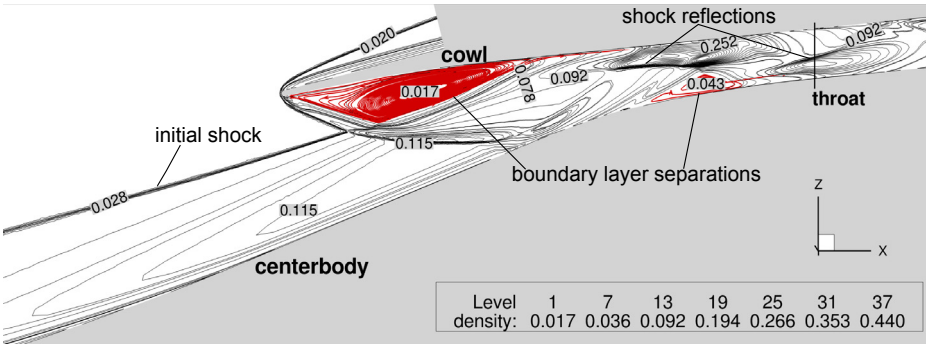

Fig. 6.8: Mach 8 freestream flow at Mach 6 geometry showing occurring separations in a density contour line plot (separations in red) – detail cut-out of cowl and throat area

6.2 Applied Flow Control at HRE at Mach 8

The efficiency of the flow control method can be evaluated against the total pressure recovery. To enhance the knowledge about the performance influencing parameters and the best combination of them, the injection angle variation effects on the performance of the HRE are investigated in the following Section 6.2.1.

6.2.1 Mach 8 Freestream Flow – Mach 6 Inlet Geometry with Injection - Injection Angle Variation Study

For analysing the effects on the shock position and the inlet's performance with a varying injection angle, a parameter study is conducted. In this study, flow is injected at five different angles through a reservoir pressure boundary condition located close to the centrebody tip. The injection surface length is 0.08 m in the *X*-direction from the end of the nose cone radius. The injection angles and parameters, including resulting mass flows, are specified in Table 6.1. Each parameter set leads to the shock-on-lip condition ensuring comparability among the test cases.

In Fig. 6.10 the contour lines of the initial shock of four different configurations are shown together in one plot. Besides the case without injection, three other configurations are shown, in which the injection angle is at 20°, 90° and 180° to the freestream flow. The injection directions are shown against the inflow direction in Fig. 6.9. Fig. 6.10 shows clearly the relocation of the initial shock with the different investigated injection angles. The injection parameters of the individual simulations are varied until the initial shock is located onto the cowl tip, whereas the individual total pressure and the total density either are increased or lowered proportional to each other.

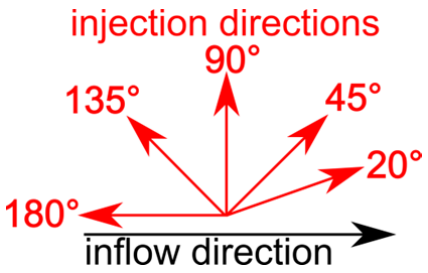

Fig. 6.9: Illustration of the injection directions, plotted against the inflow direction

It is not possible to increase the initial shock position of the 20° injection case above the shown position within the given restrictions, which are subsonic injection and the identical injection area as in the other four configurations. Higher total pressures and densities lead to supersonic injection, for which the boundary condition is not validated.

Interestingly in Fig. 6.10 the shock positions of the cases in which flow is injected perpendicular (denoted as 90°) and contrary to the flow (135° and 180°) the shock progression up to the cowl tip is nearly identical. At the perpendicular injection case, 14 % more mass flow is injected. However, the contrary injection leads to significantly higher boundary layer separations and this reduces the effective channel height more than in the other cases. The shock positions of the remaining two injection angles lie between the 20° and the 90° cases but are not shown to maintain the clearness of the discussed diagram.

In this study, the research focus is lying mainly on the initial shock that is created at the centrebody tip. The injection effect onto the shock position at the second and third compression ramp are not analysed, see Section 5.3 for a detailed discussion of the geometry features.

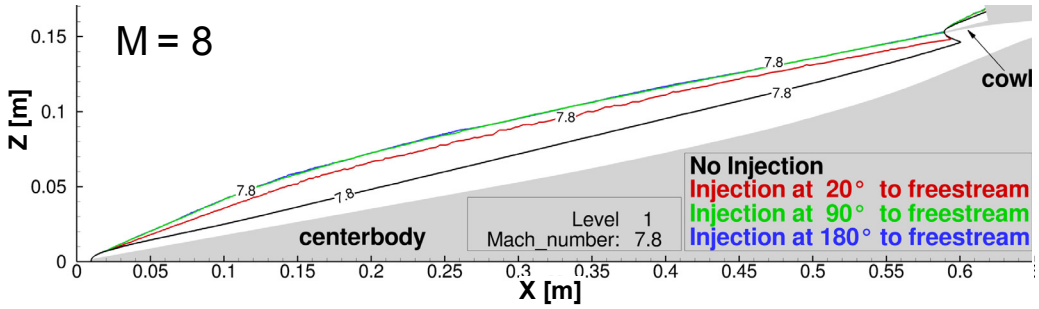

Fig. 6.10: Comparison of the effect of injection angle variation on the shock position

As noted above, at all injection angles the initial shock is located onto the cowl lip by maintaining the total density, and adjusting, with the respective total pressure, the shock position. This leads to zero mass flow loss to the atmosphere and that the strong initial shock is not impinging within the internal flow channel, leading to increased boundary layer separations.

Fig. 6.11 depicts contour lines of the 45° and 180° injection cases in the area downstream of the cowl. The Mach 3 contour lines are reflecting an estimation of the boundary layer height, whereas the Mach 0.2 contour lines are used to represent the rough size of the separation bubble. The considered separation bubbles have one Mach 0.2 outer line and one Mach 0.2 bubble. The flow at the line closer to the channel centre is streaming downstream whereas the flow in the virtual bubble is streaming at its flow-wise side upstream and at its wall-wise side downstream, as illustrated by the arrows in Fig. 6.11.

The differences in the flow are not big but still clearly visible. When regarding the Mach 0.2 boundary layer separation sizes downstream of and close to the cowl, it is obvious that the injection at 180° (highlighted with red contour lines) leads to a separation bubble, which is longer than the 45° separation (highlighted with black contour lines). In contrast to the 45° separation bubble, its beginning is 0.01 m further upstream while having almost the same reattachment position. This leads to a displacement of the shock, which is formed upstream at the separation. Also, the boundary layer at the cowl is slightly thicker.

The second interesting flow feature is located further downstream on the centrebody. As result of the impinging shock, which is formed through the above discussed flow separation, a second separation area is formed. The height of the separation of the 180° injection angle case is 1.5 times the height of the 45° injection case. This is then leading to a higher boundary layer height of 0.02 m, a significant reduction in the effective flow channel height.

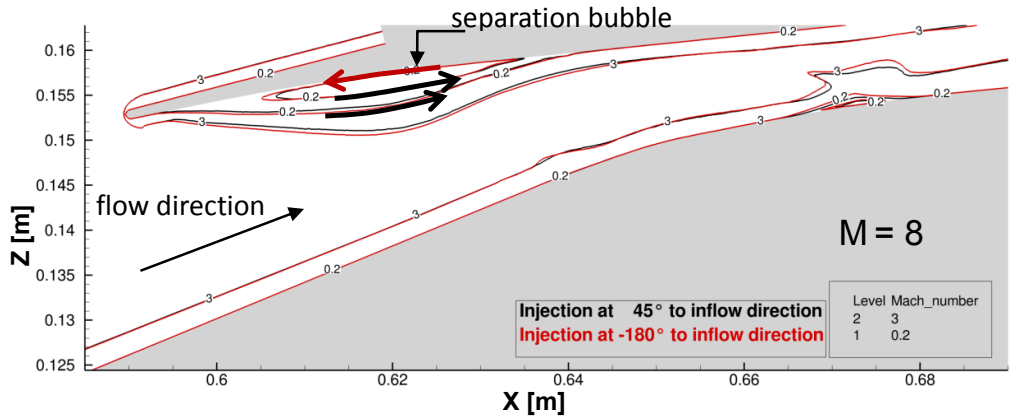

Fig. 6.11: Flow analysis of the internal flow of the 45° and the 180° injection case

To summarize the injection angle parameter study, all investigated angles except the 20° injection angle, are leading to a shock wave structure with the initial shock located on the cowl lip. However, for achieving this goal different injection settings were used, leading to different internal shock wave structures and different separation area sizes. The differences in the separation sizes and heights are leading to different effective flow channel sizes, influencing the generated turbulence and with it the losses.

To evaluate the performance of the various injection angles, the effective flow channel height can be taken as a performance parameter. It should be as large as possible, offering then the highest safety factor to prevent a choking of the inlet. When rating on this parameter, the 45° injection angle case leads to the highest performance with the consequence that this injection angle will be used for all following shock wave control analyses.

In flight, a pilot could increase the injection angle gradually from 0° to 45° allowing a smooth start of the injection and to allow a "fine-tuning" of the injection allowing to establish the shock-on-lip condition. As there are no sharp changes in the behaviour between the injection angles, this procedure should be safe.

Table 6.1: Analysis of injection angle influence onto the inlet's performance

Injection angle [°]	**$M8_{noInj}$**	**180**	**135**	**90**	**45**	**20**
$p_{t,inj}$ [Pa]	-	3,850	3,850	3,800	3,900	3,800
$\rho_{t,inj}$ [kg/m³]	-	0.0697	0.0697	0.0697	0.0696	0.0697
$\dot{m}_{inj}$ [kg/s]	-	4.14E-05	4.13E-05	4.11E-05	4.69E-05	3.43E-05
$\dot{m}_{inlet\ out}$ [kg/s]	4.45E-03	4.48E-03	4.47E-03	4.47E-03	4.48E-03	4.48E-03
Impulse **[kg·m/s]**	-	1.81E+07	1.82E+07	1.83E+07	1.60E+07	2.20E+07
Averaged mass weighted total pressure recovery η [-]	0.2764	0.3164	0.3172	0.3087	0.3141	0.2728
Effective channel height (normalised by 45° result) [%]	-	0.77	0.81	0.96	1	n/a

The different injection angles have a noticeable effect on the separation sizes. The separation just upstream of the throat leads to an effective flow channel size reduction of 23 %, when comparing the case with the smallest and the largest separation area. The lowest separation occurs during the 45° injection, but the largest occurs when injecting directly in the upstream direction (180°). This shows that the separation height is dependent on the injection angle and the injection parameters, as a higher mass flow is required at a lower injection angle, leading to larger separations.

Table 6.1 shows the differences from the remaining injection angles, which lie in between of the discussed ones. The values shown are normalised to the 45° injection channel size. In the case of the 20° injection no continuous Mach 3 flow in the channel exists, therefore no qualitative analysis is possible.

This study shows also that, when the initial shock is impinging onto the cowl lip, the injection angle influence on the averaged mass weighted total pressure recovery at the throat is small but not negligible. The individual recovery differences for the cases with fulfilled shock-on-lip condition, differ by 2.8 % from each other. To find the best and most economical injection angle, the decision which angle is used for further injection simulations, is met based on the total pressure recovery values in combination with the effective flow channel size. Whereas, the latter has the higher weighting (especially when the recoveries are in a comparable range), the effective channel height is critical as any blockage of the whole inlet has catastrophic consequences on the whole engine performance. Because the 45° injection angle leads to a relative high total pressure recovery and as it has the largest effective flow area, the following injection research studies are undertaken with this promising 45° injection angle.

It is also shown that mass flow injection at the centrebody tip has the capability to increase the incoming shock, leading to an advantageous internal shock structure with lower separations in the flow field. In this study, the mass flow injection leads to an absolute increase by 3.8 %, which is a relative increase of 13.8 %, when comparing the non-controlled case with the 45° injection angle controlled case. These values are promising and will be revised in Chapter 7 when investigating three-dimensional simulations.

In general, a mass flow rate safety margin should be available in any shock control system, allowing countering perturbations in the inflow, ensuring a stable shock-on-lip condition.

6.2.2 Injection Mechanics Analysis

To understand the mode of operation of the shock angle increase through injection, the area close to the injection is investigated in detail. For this purpose, the position of the contact surface between the injected and the freestream flow has to be determined. It turns out that with the two variables: density gradient and total pressure, the progression of the contact surface can be depicted well.

In Fig. 6.12, a density gradient contour plot is shown together with one total pressure contour line at 315,000 Pa. The contact surface between the injected and the freestream flow is represented by the total pressure contour line. The assumption that the contact surface is at roughly the determined position is confirmed by the local density gradient maximum around the contour line.

From the density gradient behaviour, it can be reasoned that the contact surface is not an infinitesimally small layer but more area region with a given thickness of 1.4 mm, which is the height of the plateau of the density gradient in Fig. 6.13, as highlighted. Further mesh adaptations have no significant influence onto the height of the contact area. The vertical dashed lines I - VIII mark the positions at which the shock angle and contact surface angle are measured from the centrebody tip, these data is given in Table 6.2. The maximum density gradient represents the progression of the strong main shock generated at the centrebody tip, as highlighted.

In Fig. 6.13, the total pressure and the density gradient are shown against the *Z*-position at an *X*-position of 0.05 m. The total pressure is shown on a logarithmic axis. At a *Z*-value of about 0.0177 m, the density gradient has a local maximum, localising the potential position of the contact surface. At the same height, the total pressure has a value of about 315,000 Pa. Within a *Z*-height of 0.0168 m to 0.0197 m, the total pressure rises constantly from 90,000 Pa to 890,000 Pa, mainly due to the increasing Mach number with increasing distance to the wall surface. During this constant total pressure increase, the position of the contact surface cannot be seen in the behaviour of the total pressure values. However, when comparing the progression of the 315,000 Pa total pressure contour line with the local density gradient maximum close to the contour line, the assumption can be formulated that the contact surface follows in this case the 315,000 Pa total pressure contour line. The total pressure variable is one amongst other variables with which the contact surface can be depicted in this case with a high degree of accuracy. Other possible variables are, for example, the turbulent Mach number, the density gradient and the velocity in Z-direction. However, the accord between the 315,000 Pa total pressure positions and the resulting shock angle (see Table 6.2) is better than with the other mentioned variables.

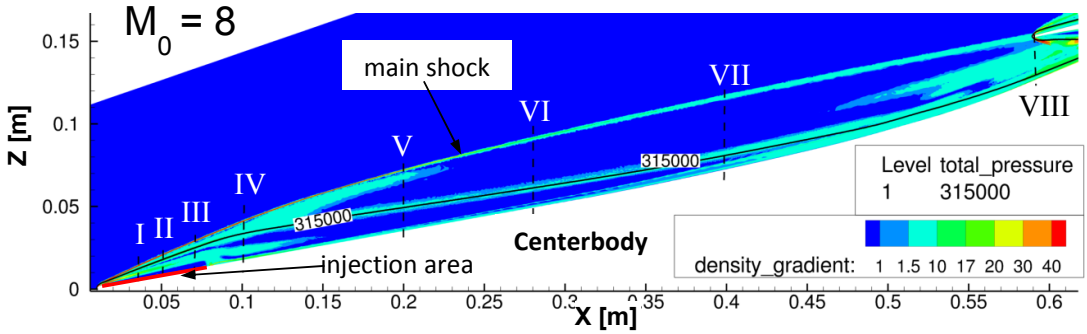

Fig. 6.12: Density gradient contour plot with one total pressure contour line depicting the contact surface

At the measurement positions downstream of the injection area, the density gradient is not clearly indicating the position of the potential contact surface. Therefore, other methods for its visualisation have to be found.

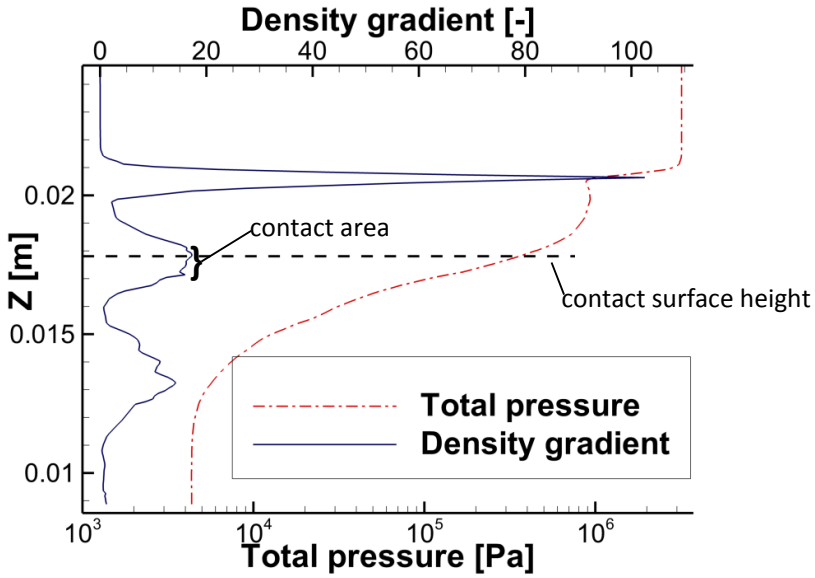

Fig. 6.13: Total pressure and density gradient progression versus Z-position at an X-position of 0.05 m

When assuming that the contact surface is at the position of the 315,000 Pa total pressure contour line, indicated in Fig. 6.12, then the shock angle should be matching the angle of the contact surface.

Zumwalt and Tang (1963) found that the relationship of a pressure coefficient on a cone, across conical shocks, is independent of the freestream Mach number, as it is only a function of the cone angle. They showed also with equation Eq. 6.1 that the approximate shock wave angle β (in degrees) could be determined, when the freestream Mach number M and the half-cone angle θ (in degrees) are known:

$$sin^2\,\beta = \frac{1}{M^2} + 0.038\left(\frac{\theta}{10}\right)^{1.87} \qquad \textbf{Eq. 6.1}$$

As viscosity is taken into account, the shock angle is predicted with a high precision. The predicted and the CFD-determined shock angle in the non-injection case differ by only 0.22° from each other. Other shock angles from former simulations also show comparable agreement between the analytical and the numerical methods. Thus, due to the good agreement, Eq. 6.1 is used for the prediction of shock wave angles around cones.

In Table 6.2, the measured shock angles, contact surface angle and calculated shock angle (using Eq. 6.1), assuming that the above defined contact surface acts similar to an inviscid wall, are shown for multiple *X*-position locations, which are highlighted in Fig. 6.12. The stated difference is the measured shock angle minus the calculated shock angle, based on the contact surface angle in degrees.

In Table 6.2, the assumption is confirmed that the shock angle matches well to the contact surface angle. The agreement of the contact surface and the shock position is good during the first straight contact surface segment up to an *X*-position of about 0.09 m, just downstream of the injection area. But with increasing X-position the agreement between the expected shock and the measured shock reduces significantly. However, in the region with high agreement between the measured and the calculated angle, the difference between these angles is less than 0.15°. Downstream of the straight contact surface region, the difference increases rapidly, as at measuring position IV the difference is 0.61° and at position V the difference is 2.72°. The increasing difference in the area downstream of the injection area can be reasoned, on the one hand, with the bow-like structure of the shock, which is resulting from the missing injection downstream of the injection area. On the other hand, the expansion of contact surface normal to the wall is increasing with increasing distance to the injection position. Firstly, the contact surface can be understood as thin contact layer, whereas with increasing downstream position, in this case, downstream of measurement position III the thickness of the layer is increased and it can be understood as the contact area.

Measurement point VII is shown for reference only as it cannot be used for the understanding of the progression of the bowed shock as the cone angle has changed ($\Delta\boldsymbol{\theta}$). Further studies would have to be performed in order to be able to predict the bow-shock angle downstream of the straight shock close to the injection area.

Table 6.2: Comparison of shock angle change due to contact surface formation

	no injection	I	II	III	IV	V	VI	VII ($\Delta\theta$)
X-position [m]	0.109	0.036	0.050	0.070	0.102	0.202	0.287	0.401
Contact surface angle (CFD) [°]	18.29	19.08	19.47	19.48	18.55	13.89	12.35	11.46
Measured shock angle (CFD) [°]	20.97	22.07	22.52	22.57	22.28	19.76	17.92	16.24
Calculated shock angle to contact surface [°]	21.40	22.21	22.60	22.61	21.66	17.04	15.57	14.73
Difference [°]	0.22	0.14	0.08	0.04	-0.61	-2.72	-2.35	-1.51

Fig. 6.14 shows a magnification of the injection area with active injection. The injection settings are similar to the 45° case of Section 6.2.1. A Mach number plot with streamlines is presented in order to give a better visualisation of the flow topology around the injection surface. The streamlines can be considered as indicating the progression of the shock wave due to the injection, both highlighted in Fig. 6.14.

The Mach number plot shows the low Mach number close to the injection surface and the thick boundary layer just downstream of it. The injected mass flow is increasing the displacement thickness of the boundary layer. Therefore, the contact surface, depicted by the 315,000 Pa contour line, acts as a barrier and is causing the incoming flow to form a shock wave with a higher angle than without injection. The contact surface separates the high-speed freestream flow from the injected low Mach number flow. However, there is a mixing of these two flows due to the large Mach number gradient between them. As mentioned above, the progression of the shock is a straight line when in the *Z*-direction above the injection area, but its angle lowers downstream of the injection area. This behaviour has also been seen and discussed in Section 6.2.1. As highlighted in the figure, the injection leads to a small boundary layer separation.

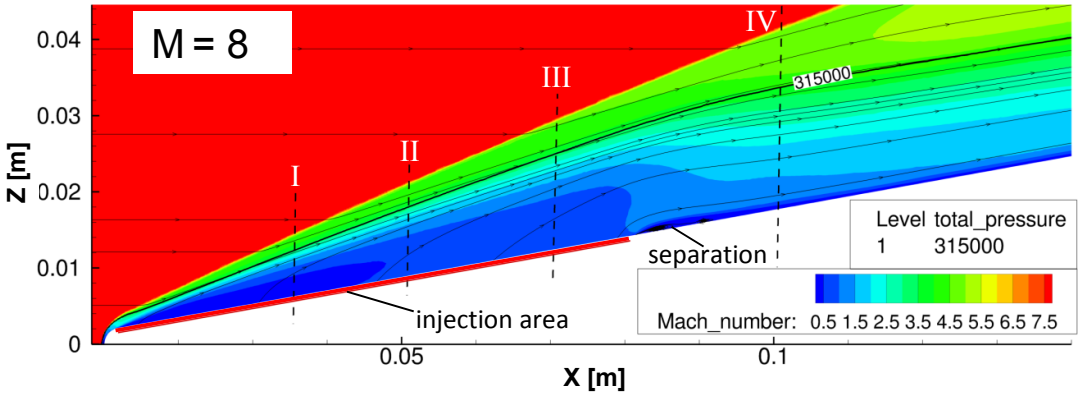

Fig. 6.14: Mach number plot with one contour line at M=8 freestream flow with injection – detail

In Fig. 6.15, a pressure plot shows the expansion of the injected air. The pressure has its maximum under the compression shock close to the centrebody tip and is gradually reducing with increasing downstream direction. Due to the compression through the shock, the pressure just downstream of the shock is significantly higher than at flow layers closer to the surface wall. At the downstream end of the injection is a concentrated expansion fan, as highlighted. It is formed through the pressure difference of the region with the high pressure, above the injection area, and the lower pressure above the surface downstream of the injection area.

In the region close to the injection area, the boundaries between some of the pressure contour lines are unclear, one example position is highlighted in Fig. 6.15. This phenomenon can be caused by oscillations within the flow during the expansion, or a too coarse resolution of the grid, even if one focus during the mesh creation and adaptation was lying on the area close to the injection area. At the regarded region close to the injection surface, multiple aerodynamically highly relevant flow features occur. These are the mass flow injection with a high total pressure, the expansion of the injected flow and the formation of a compression shock. These flow influencing features are leading to a probable not fully uniform expansion. Therefore, a time-

dependent simulation should be performed in a further study to investigate this behavior in a higher detail and to determine the strength of the oscillation.

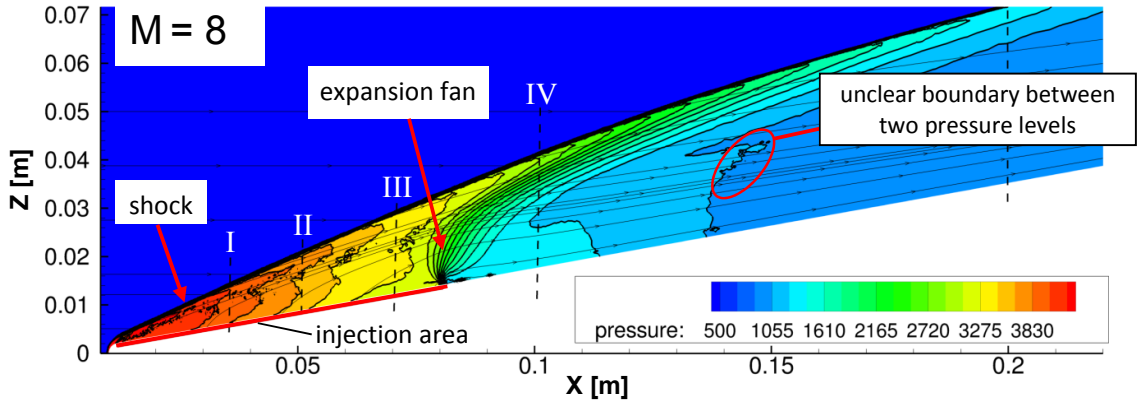

Fig. 6.15: Pressure plot with pressure contour lines – detailed injection area

Fig. 6.16 and Fig. 6.17 are shown for completeness. In Fig. 6.16, a Mach number plot of the complete flow field from the centrebody tip up to the cowl lip is shown, including the 315,000 Pa total pressure contour line, indicating the contact surface. In Fig. 6.17, the centrebody tip section of the simulation without injection is shown, presenting the progression of the total pressure contour line in the non-controlled case.

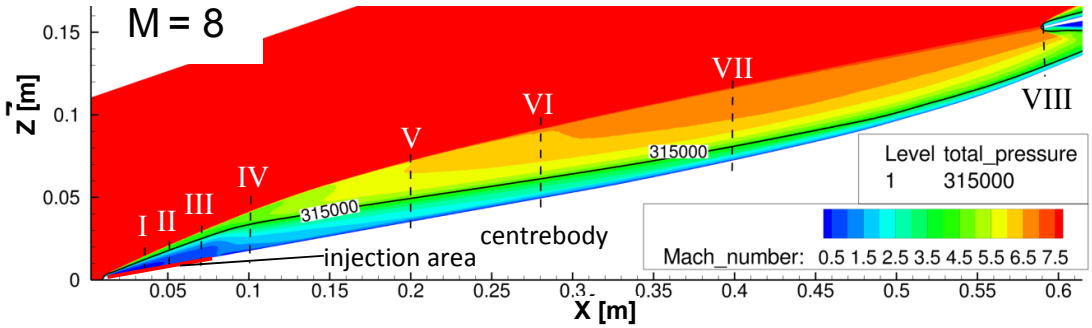

Fig. 6.16 Mach number plot with one contour line at *M=8* freestream flow with injection – overview

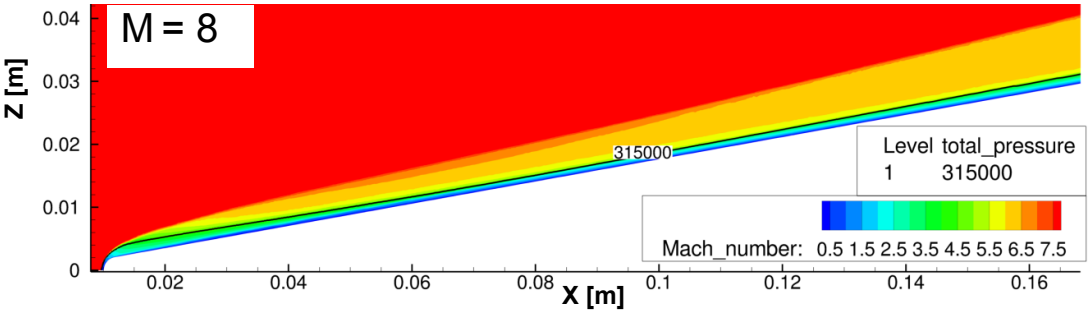

Fig. 6.17: Mach number plot with one contour line at *M=8* freestream flow without injection – close-up

In conclusion, the shock angle increase through mass flow injection comes about, because the injected mass flow increases the boundary layer displacement thickness close to the injection area. This increased displacement thickness acts like a wall for the incoming freestream flow, leading to an increase of the shock wave angle. As the displacement thickness decreases with

increasing downstream distance to the injection surface, the shock is bowed downstream of the injection area, where the formed compression shock has a constant angle. This knowledge forms a stable background for the following three-dimensional investigations.

When increasing the injection mass flow rate from zero, the flow behaviour changes in a continuous fashion, which is enabling this approach to be considered as a practical application to an aircraft engine, to maintain in-flight a shock-on-lip condition. This would be successful for both long-term and transient flow conditions, i.e. for slow changes in Mach number due to the required trajectory profile, and for any shorter-term disturbances or anomalies in the freestream during flight. Two sensors are needed, one detecting turbulences and perturbations upstream of the inlet and one at the cowl tip, detecting the precise position of the impinging shock. With this information, a computer should be able to predict the required injection mass flow to counter the perturbations, maintaining in the shock-on-lip condition. This would result in a fast reaction fine-tuning control system, increasing the efficiency of the inlet without variable geometry and would prevent possible engine unstarts, or other non-smooth abnormal engine operation, through blocked inlets. For the very short-term usage, which is understood as injection for just a moment, additional studies should be performed. The aim should be the determination of short-term injection possibilities as it is unclear what time it takes until a steady flow pattern has formed.

In Section 7, the inlet that was analysed in quasi three-dimensional flow in the current section will be analysed in three-dimensional flow. Shock control studies will be performed at zero angle of attack and at an angle of attack investigating the possibility to control shocks in an asymmetric flow field.

7 Three-Dimensional Inlet Analyses

In this chapter, the previous obtained knowledge about flow control through mass flow injection is applied to a three-dimensional inlet analysis. In Section 7.1, the known HRE Mach 6 inlet is investigated at a Mach number of 8 without and with applied flow control. There follows in Section 7.2, a Mach 8 study of the same inlet geometry but at an angle of attack and asymmetric injection at the centrebody tip.

7.1 Mach 8 Freestream Flow at Mach 6 Inlet

In Section 6.2, it is shown that in quasi-three-dimensional simulations the method of mass flow injection can be used efficiently to increase a compression shock angle. Based on the obtained knowledge from those investigations, a half-model will be simulated here to examine the flow in full three-dimensional simulations. The aim of this research is the confirmation of the presumption that the quasi-three-dimensional results correlate to the symmetrical three-dimensional results at 0° angle of attack. Furthermore, in Section 7.2, the identical inlet will be investigated at a non-zero angle of attack, allowing the examination of the occurring asymmetric flow around the inlet and the possibility of increasing the performance at an angle of attack.

Investigated is the HRE geometry as described in Section 5.3. Its two-dimensional contour is rotated for 180° around the *X*-axis, leading to a half-model geometry. Eight different injection surfaces were constructed at the centrebody tip with the same stream-wise dimension as the injection surface in Section 6.2.1. This allows a variation of the injection parameters of the individual surfaces, which is required to investigate an asymmetric mass flow injection in Section 7.2.

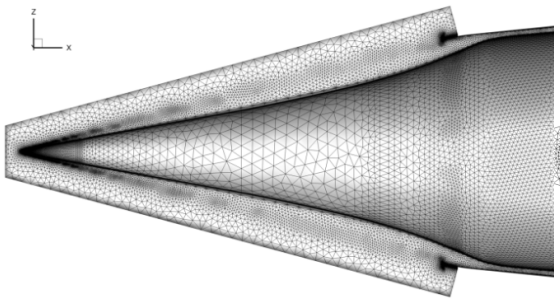

Fig. 7.1: Original mesh with 2.71 million points

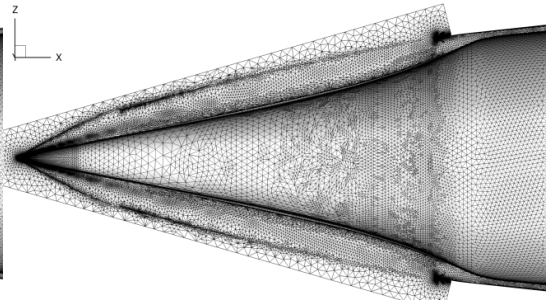

Fig. 7.2: Mesh after 11 adaptations with 4.99 million points

Fig. 7.1 and Fig. 7.2 show three-dimensional meshes. The original mesh with 2.71 million points (Fig. 7.1) is shown in comparison with the final mesh (Fig. 7.2) after eleven mesh adaptations using the TAU-Code mesh adaptation tool. With each adaptation step, the total number of mesh nodes increased gradually to 4.99 million. The adaptation methodology ensured that the additional mesh points were positioned in the areas where large density, pressure and Mach number gradients occur. Due to the usage of a source during the meshing process the progression of the primary bow shock from the centrebody tip to the cowl tip is refined, enhancing the accuracy of the original mesh. Therefore, in the adapted mesh (Fig. 7.2), the adaptations lead to an increase of the resolution mainly in the area of occurring shocks. In addition, the progression of the reflected shock structure can be estimated when developing the mesh.

Careful usage of the adaptation settings allowed a reduction of mesh points in areas where they are not required, while still obtaining a detailed result. The adapted mesh is coarsened in areas with small variable gradients, for example in the farfield. The mesh adaptations progress during the solving of the flow equation. For this case, after eleven mesh adaptations, the flow solution can be regarded as converged because not only is the density residual converged but also, and more importantly, the mass flow rates are converged at the injection surfaces as well as the outflow planes. In addition, multiple solutions from different adaptation steps are compared with each other. In the eleventh adapted mesh and solution, the position and the size of occurring flow phenomena are constant. These phenomena are the compression shock angles but also the boundary layer separations, which are significantly more sensitive to the mesh resolution and the progression of the simulation.

Fig. 7.3 shows Mach number contour lines of the HRE geometry at which the cowl position is designed for Mach 6 flow at zero degrees angle of attack, as stated by Pearson and Jilly (1969). Depicted are the contour lines of two cases, without injection (black line colour) and with mass flow injection (red line colour). The freestream Mach number is *M=8* which leads to a lower compression shock angle of the shock, generated at the centrebody tip. Therefore, the bow shock formed at the tip is not impinging on the cowl tip but on the inside cowl surface, within the inlet, leading to the formation of a boundary layer separation (shown with black contour lines). In the injection case (red contour lines), the shock angle is increased in a comparable behaviour as in the former quasi-three-dimensional analysis (see Section 6.2).

The *M=7.9* contour line depicts the compression shock progression. In the injection case, the maximum shock angle is located close to the injection area. With increasing downstream distance to it, the shock angle is decreasing. The *M=4* contour lines are shown to illustrate the approximate

boundary layer height. The *M=4* contour line was chosen, as it allows an interpretation of the low Mach number flow behaviour in Fig. 7.3, than a lower Mach number contour line, which behaves comparable but closer to the wall. However, the *M=4* contour line cannot be understood as boundary layer height.

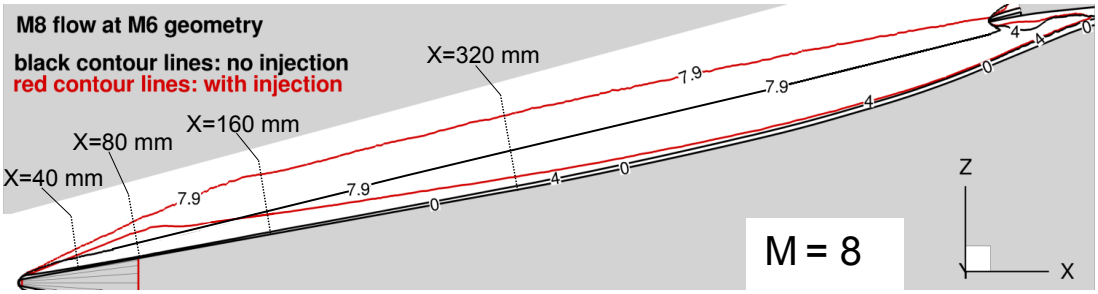

Fig. 7.3: Mach number contour lines depicting the shock progression without and with mass flow injection

The *M=4* contour lines show that the height of the lower Mach number region on the centrebody surface, in the case without injection, is increasing gradually downstream. In the case with active injection, the boundary layer is thickened strongly due to the injection so that the maximum boundary layer height is close to the downstream end of the injection area. With increasing downstream position, the boundary layer height reduces continuously, as discussed below, based on Fig. 7.6. This is leading to a nearly comparable but still slightly higher boundary layer height on the centrebody and downstream of the cowl, when comparing the injection case with the case without injection. As result of the non-impinging compression shock on the inner cowl side, a significantly smaller boundary layer separation is caused.

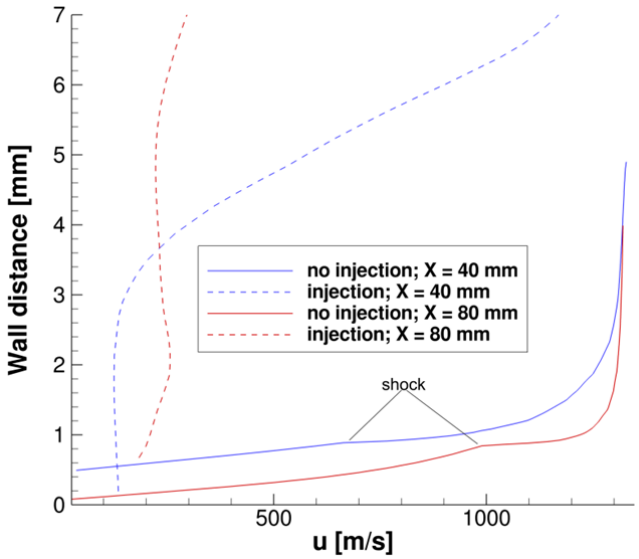

Fig. 7.4: Velocity profile versus the normal distance to the wall at two *X*-positions: 40 mm and 80 mm

In addition to Fig. 7.3, velocity profiles at *X*-positions of 40 mm and 80 mm, indicated in Fig. 7.3, are shown in Fig. 7.4. In total, four profiles are shown, at both positions, one profile for the case without and another for the case with injection. The 40 mm profile is taken normal to the surface at the middle of the injection surface, whereas the 80 mm profile is taken right at the end of the injection surface, as shown in Fig. 7.5. When comparing in Fig. 7.4 the non-injection cases with each other (red and blue solid lines), one can see that in both cases the speed above the boundary layer is about 1,340 m/s, which is the freestream velocity. However, when determining the boundary layer thickness from the position where the velocity is 99 % of the freestream velocity, the boundary layer thickness at 40 mm has a height of 3.64 mm, and at 80 mm, it is 1.86 mm thick. The boundary layer at 40 mm is thicker than the boundary layer at 80 mm. This, unexpected behaviour, can be probably explained through the geometry as the rounded cone tip is leading to a small bowed shock and also to a thicker boundary layer close to the tip.

When regarding the two injection cases, the profiles differ strongly from each other. The velocity close to the wall of both injection cases is significantly lower than in the non-injection cases. At 40 mm, fluid is injected with a velocity of 130 m/s, with increasing distance to the wall it is slowing continuously down to 115 m/s at a wall distance of 2.4 mm. At the 40 mm profile, the injection middle, the velocity is lower than at the 80 mm position, up to a wall distance of about 3.6 mm. At higher wall distances, the fluid accelerates continuously up to the next shock before the freestream condition. The velocity of the 80 mm profile is close to the wall about 180 m/s. With increasing distance to the wall, the flow accelerates up to 250 m/s, which can be explained through the expansion at the downstream end of the injection surface (see Fig. 7.5).

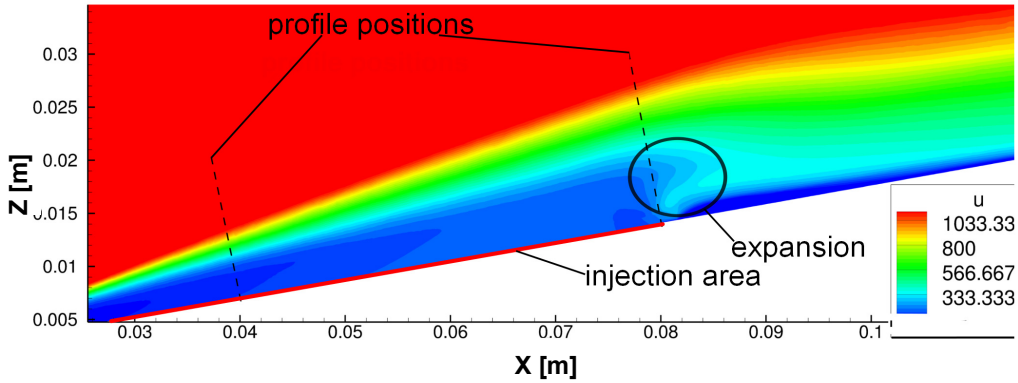

Fig. 7.5: Velocity plot, showing the two positions of the velocity profiles of Fig. 7.4

Fig. 7.6 shows also four velocity profiles, taken normal to the surface, through the boundary in a wall distance – velocity plot at two *X*-positions. When comparing the non-injection profiles at 160 mm and at 320 mm with each other, one can see that the boundary layer at *X=160 mm* has a thickness of 2.3 mm, whereas the boundary layer at *X=320 mm* is with 3.1 mm significant thicker

as the first regarded one. This qualitative behaviour is expected, as the boundary layer thickness should increase with increasing downstream position.

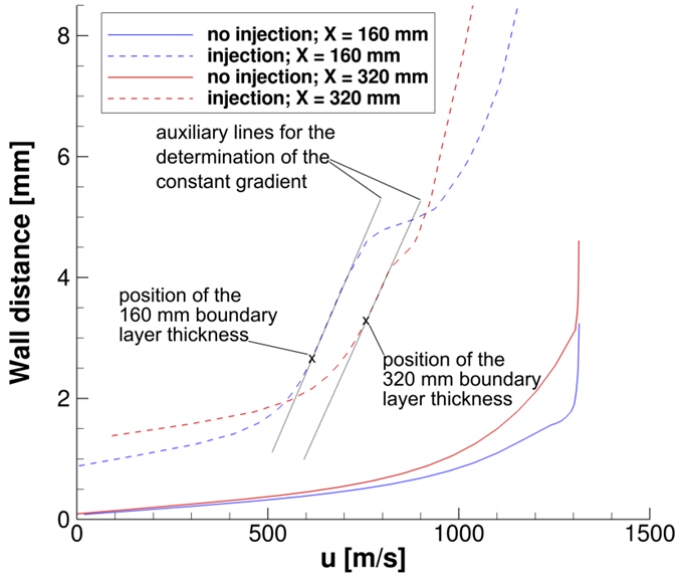

Fig. 7.6: Velocity profile versus the normal distance to the wall at two *X*-positions: 160 mm and 320 mm

When regarding the injection cases, the velocity profiles are not allowing the determination of the exact boundary layer thickness as the velocity is not accelerating, with increasing distance to the surface, with the same characteristics as in the cases without injection. In detail, with injection, the velocity is not accelerating with constantly increasing gradient, and converges then to the one freestream velocity value. Rather, the velocity accelerates through the boundary layer before it is increasing with a higher and constant gradient above the boundary layer. Therefore, it is possible to determine the rough boundary layer thicknesses, when using the velocity gradients. To simplify the determination of the boundary layer thickness, it is assumed that the boundary layer thickness can be determined from the position where the velocity increases with a constant gradient (as indicated in Fig. 7.6).

Based on the above presented method to determine the boundary layer thicknesses of the injection cases, the boundary layer thickness at an *X*-position of 160 mm is 2.6 mm with a velocity of 610 m/s. Whereas, the boundary layer of the profile at 320 mm is 3.3 mm thick with a velocity of 765 m/s.

These values indicate that the boundary layer thickness increases with increasing X-position (i.e. increasing downstream position). When determining the thickness with the method discussed above, it can be stated that the velocity above the boundary layer increases with increasing *X*-position. This finding represents well the actual behaviour of the flow close to the wall, when regarding the flow behaviour at stations downstream of the injection position.

In Fig. 7.7, the cowl area is shown in an enlarged cut-out. It is depicting contour lines for both investigated cases. In this and the previous Fig. 7.3, the significantly larger boundary layer separation on the inner cowl side can be observed. Through the injection, the height of the separation is reduced from 0.0048 m to 0.0015 m which is a reduction of 68 % when regarding the separation area with flow below the speed of *M=1.5*. When regarding the area in which the flow is lower than *M=4*, then the separation height at the inner cowl area is reduced from 0.0093 m without injection to 0.0038 m with mass flow injection which is a reduction of 60 %. Due to this, the effective channel height at the separation position is increased from 0.008 m to 0.012 m, an increase of 50 %, which is ensuring stable working of the inlet by avoiding inlet channel blockage caused by boundary layer separation due to a serve shock wave/boundary layer interaction.

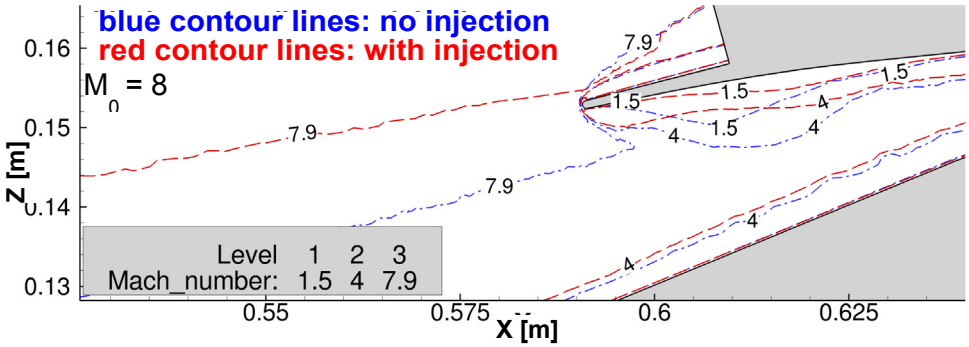

Fig. 7.7: Mach number contour lines plot in the upper cowl area cut-out in the symmetry plane to compare inlet flow without and with injection

In Fig. 7.8 the static pressure at the inner cowl wall is shown against the X-position for both cases, without and with injection. The cowl tip is at 0.587 m, leading to the static pressure maxima in the graph. In the case without injection, the maximum wall pressures are with 28,550 Pa at *X=0.66 m* and 21,540 Pa at *X=0.69 m* about 7 % higher than the wall pressures of the injection case. Higher wall pressures have the potential of leading to the formation of larger boundary layer separations. The local maxima and minima of the two comparing static pressure curves are at nearly identical positions, with a deviation of +/- 0.006 m in *X*-direction.

The analysis of these graphs shows that the introduced injection has no big influence on the position of the local pressure maxima but the injection is reducing the maxima leading to smaller separations and lower losses of the total pressure recovery.

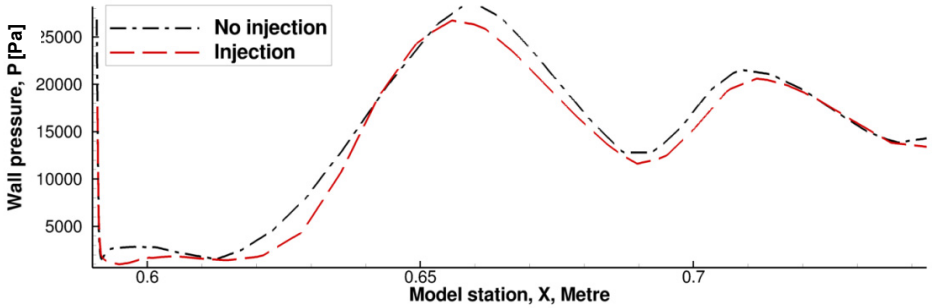

Fig. 7.8: Static wall pressure at inner cowl wall against *X*-position from two simulations, without injection and with injection

In Fig. 7.9 and Fig. 7.10, the throat height ratio against the throat Mach number and the total pressure recovery at the throat of the simulation are presented in two diagrams. A height ratio of zero is indicating the centrebody wall, respective, a height ratio of one is indicating the inner cowl wall. The progression of the Mach number with the height ratio of the simulation with active mass flow injection shows that the average Mach number is higher than in the non-injection case. Thus, more kinetic energy is at this position in the flow. This allows a higher compression for a more efficient combustion, or allows combustion at higher velocities, leading to higher speeds in the nozzle and to a bigger thrust production. The maximum Mach numbers are at different height ratios. The maximum in the non-injection case is close to the throat centre at a height ratio of 0.58, whereas, the injection case maximum is at a height ratio of 0.82, significantly closer to the cowl wall. The variation in the position of the pressure maximum results from the reduced boundary layer separation and the changed shock structure within the inlet.

The progression of the Mach numbers at a height ratio range from 0 to 0.12 are for both investigated cases nearly identical. From that, it can be concluded that the boundary layer growth and its height are almost identical. This shows that the introduced symmetric mass flow injection is not leading to significantly higher boundary layer heights within the inlet, as long as the regarded position is far enough downstream of the injection position.

Within the height ratio range from 0.12 to 0.42, the Mach number of the case with injection is slightly lower than in the case without injection. However, in the height ratio range above 0.43, the injection is leading to a significantly higher Mach number. This results from the reduction of the boundary layer separation at the inner cowl surface downstream of the cowl tip. Overall, the stream-thrust averaged Mach number of the non-injection case is $\bar{M} = 2.852$ and of the injection case it is $\bar{M} = 2.973$, which is 4.2 % higher compared with the non-controlled case. The stream-thrust averaging conserves mass, momentum and energy and allows to determine from a three-dimensional data one-dimensional data. The stream-thrust averaging is giving a higher accuracy

then simple averaging of the Mach number over the height. DeBonis et al. (1999) give the equation for the determination of the stream-thrust averaging and more details to it.

In the three-dimensional simulations, the focus is on a high resolution of the injection area and the main shock, forming at the tip and impinging at the cowl. Due to limited resources, a lower resolution at other positions had to be accepted. The relative sharp changes in Fig. 7.9 and Fig. 7.10 are caused by the grid resolution at the throat position, not degrading the validity of these figures.

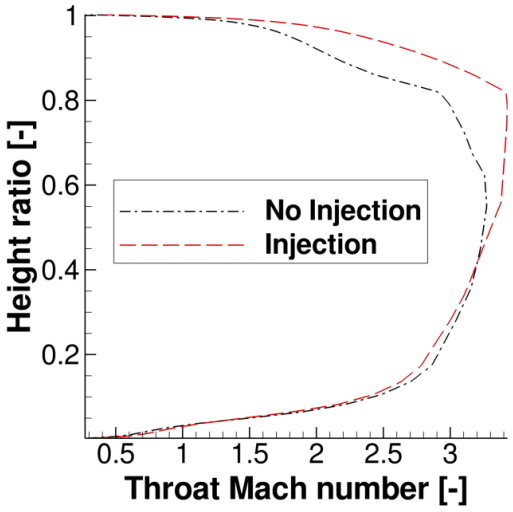

Fig. 7.9: Throat height ratio vs. Mach number

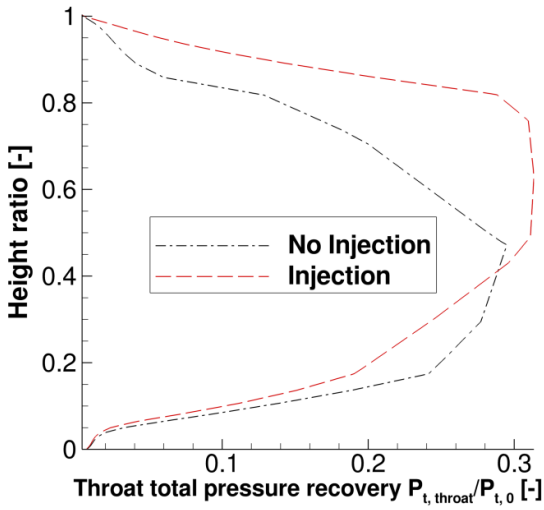

Fig. 7.10: Height ratio vs. total pressure recovery

The higher average throat Mach number has the potential of leading to higher total pressure values in the throat, as depicted in Fig. 7.10. The maxima of the total pressure recoveries are for both investigated cases not identical, too. The maximum of the non-injection case is at a height ratio of 0.38, whereas the maximum of the case with injection is at 0.6. The differences are caused by the identical reasons, which were leading to a variation in the maxima of the throat Mach number.

In the height ratio region below 0.42, the total pressure recovery of the simulation with active injection is lower than the total pressure recovery of the non-injection case. This is caused by the displacement of the total pressure maximum in the height ratio, due to a variation of the shock reflection structure. Above the height ratio of 0.42, the total pressure is significantly higher than the case with active injection. This results on the one hand from the higher throat Mach number in that region (see Fig. 7.9) but on the other hand also from a higher static pressure. The higher static pressure can be reasoned to be due to identical Mach numbers of both cases, above a height ratio of 0.96, which would result in identical total pressure recovery. If the static pressures

would be identical, the total pressures would be identical, too. However, as the total pressure of the injection case is higher, the static pressure has to be higher as well.

When comparing these results with the study presented by Tan et al. (2007) in Section 3.3.2.2, differences between the required secondary flow amounts are noticeable. Tan et al. determined a secondary flow height of 15 % in their numerical setup, whereas, in this study the thickening of the boundary layer and the resulting increase in the captured inlet flow area can be neglected. These differences can be traced back to variances in the geometrical setup and the freestream Mach numbers in which the inlets are investigated. Tan et al. were also injecting at two ramps, not only at one, which could have a significant effect on the boundary layer height as at the second injection position a boundary layer is approaching, which is likely to increase its height strongly, when flowing over an injection surface.

Table 7.1: Comparison of quasi-3D and 3D results with experimental results

	M6 geometry M6 flow	**M8 geometry M8 flow**	**M6 geometry M8 flow**	
η	experiment	experiment	quasi-3D-simulation	3D simulation
$\left(\frac{P_{t,CC}}{P_{t,0}}\right)_{not\ controlled}$	0.445	0.444	0.276	0.291
$\left(\frac{P_{t,CC}}{P_{t,0}}\right)_{controlled}$	n/a	n/a	0.314	0.325

When comparing the three-dimensional results, given in Table 7.1, with the quasi-three-dimensional results from Section 6.2 (also given in Table 7.1), the averaged mass weighted total pressure recovery, at the eight identical measurement positions, of the uncontrolled case is with 0.276 about 5.2 % lower than the 0.291 in this three-dimensional analysis. Comparing both injection cases with each other, the differences are significantly lower as the quasi-three-dimensional result, with its total pressure recovery of 0.314, is 4.4 % lower than the three-dimensional result with 0.325. However, the sources of these variations could not be determined. Therefore, further studies have to be performed to study whether the differences arose from very different meshes, from different simulation settings, the boundary condition or from something else. It is important to highlight the high relevance of the measurement positions and the averaging method. For the comparison between the experiment and the numerical result, the averaged mass weighted total pressure recoveries have to be taken at the identical positions, ensuring comparable results.

Overall, the averaged mass weighted total pressure recovery of the three-dimensional non-injection case is $\frac{\overline{P_{t,CC}}}{P_{t,0}} = 0.291$. The injection is leading to a total pressure recovery of $\frac{\overline{P_{t,CC}}}{P_{t,0}} = 0.325$ which is 11.2 % higher as in the non-controlled case. Overall, the total pressure recoveries of the cases with active injection are not as high as in the experiments with variable geometry, given in . Tan et al. (2007) experienced a total pressure reduction of 7.5 % of the variable geometry to the shock angle control case, where they simulated a geometry designed for Mach 5 in a Mach 6 freestream flow. In the present research, the difference between the design (*M6*) and the freestream Mach number (*M8*) is *M=2*, not only a difference of *M=1* as in the case Tan et al. (2007). Therefore, no comparison with other studies is possible, and thus, the relatively low total pressure recoveries have to be accepted.

Continuous operation with such low total pressure recoveries does not lead to high efficiency but short-term operation at a Mach number higher than the design Mach number seems feasible. One possible field of operation could be a supersonic interceptor plane having a low design Mach number at which it is standing by or flying back to its home base and a higher Mach number to intercept other planes. At the higher Mach number, the shock-on-lip would be ensured by mass flow injection, above the design Mach number. Detailed trade-off and feasibility analyses have to be performed prior to the design of inlets in which the shock waves are controlled by mass flow injection, as it has the potential to be used for maximising the overall performance of an inlet, when regarding the complete aircraft mission.

7.1.1 Injection Sensitivity Analysis on the Inlet Performance

To gain knowledge about the sensitivity of the injection parameters to the performance of the inlet, the injection parameters: total pressure and total density, are varied about the optimum parameter settings determined in Section 7.1.

Six sensitivity simulations are performed allowing an investigation of the influence when increasing and decreasing the injection parameters by 2.5 %, 5 % and 10 %. In Table 7.2, the injection parameters are listed for the individual factors, with which the optimised injection parameters are multiplied. In addition, the resulting total pressure recoveries and captured mass flow rates are presented.

Table 7.2: Sensitivity study injection parameters and performance values

Factor [-]	0.9	0.95	0.975	$1_{optimised}$	1.025	1.05	1.1
$p_{t,inj}$ [Pa]	3,240	3,420	3,510	3,600	3,690	3,780	3,960
$\rho_{t,inj}$ [kg/m³]	0.0627	0.0662	0.0679	0.0696	0.0714	0.0731	0.0766
$p_{t,0}$ [Pa]	3.19E+06	3.19E+06	3.19E+06	3.19E+06	3.19E+06	3.19E+06	3.19E+06
$p_{t,throat}$ [Pa]	7.18E+05	7.29E+05	7.35E+05	7.36E+05	7.37E+05	7.21E+05	6.52E+05
$\frac{\overline{p_{t,throat}}}{p_{t,0}}$ [-]	**0.3166**	**0.3225**	**0.3239**	**0.3253**	**0.3250**	**0.3179**	**0.2882**
$\dot{m}_{capt}$ [kg/s]	**7.936E-01**	**7.939E-01**	**7.936E-01**	**7.923E-01**	**7.905E-01**	**7.836E-01**	**7.442E-01**
$\dot{m}_{inj}$ [kg/s]	5.620E-03	6.357E-03	6.767E-03	7.180E-03	7.598E-03	8.464E-03	1.028E-02
$\dot{m}_{inj}/\dot{m}_{capt}$[-]	**7.081E-03**	**8.007E-03**	**8.527E-03**	**9.074E-03**	**9.611E-03**	**1.080E-02**	**1.381E-02**

As shown in Table 7.2, the total pressure is varied from 3,240 Pa up to 3,960 Pa, while the total density is varied from 0.0627 kg/m³ to 0.07665 kg/m³. Again, it would be ideal to have only one parameter varying per study. However, a variation in the starting values of one of these parameters implies that only one of the total pressure, total density and total temperature can remain constant whilst the other two vary, assuming that the specific gas constant, R, remains identical. In the optimised case, the set injection parameters are $p_{t,inj} = 3{,}600\ Pa$ and $\rho_{t,inj} = 0.0697\ kg/m^3$.

As in the previously investigated cases, the mass weighted total pressure values measured at the throat position are used for the determination of the averaged mass weighted total pressure recoveries. The captured mass flow rate, $\dot{m}_{\mathrm{captured}}$, is the actual measured value minus the injection mass flow rate to obtain the adjusted correct comparable value.

As it can be seen, when regarding the rates of the captured mass flows of the simulations with the factors 0.9, 0.95 and 0.975, the captured mass flow rates are nearly identical, whereas the averaged mass weighted total pressure recovery, $\frac{\overline{p_{t,throat}}}{p_{t,0}}$, increases gradually with increasing multiplier.

The optimised version, labelled with a factor of 1, has a slightly lower mass flow rate as the cases with the reduced injection total pressure and total density. In the optimisation process, the focus was on the optimisation of the total pressure recovery and not on the captured mass flow.
With increasing multiplier, the captured mass flow rate decreases, as mass flow is lost to the atmosphere. The loss of mass flow is also leading to a reduction in the total pressure recovery.

Overall, it is shown that the variation of the injection parameters is influencing the resulting inlet performance strongly. When comparing the configurations with the factors 0.9, 1 and 1.1, it becomes apparent that the shock has to be kept inside of the inlet if possible, as long as it is not causing a blockage of the inlet. If it is kept inside, the total pressure recovery reduces slightly, but the captured mass flow rate remains constant. If the shock misses the cowl completely, the mass flow rate and the total pressure recovery are significantly reduced.

In Fig. 7.11, a Mach number line plot is shown on the upper half of the symmetry plane in which the above regarded cases with factors 0.9 (the *Reference * 0.9*), 1 (*Reference*) and 1.1 (*Reference * 1.1*) are shown for comparison. In Table 7.2, the configuration, which is denoted with $1_{optimised}$, is defined as the Reference case with a total pressure of $p_{t,inj} = 3{,}600\ Pa$ and a total density of $\rho_{t,inj} = 0.0696\ kg/m^3$. The contour lines for three Mach number levels are shown, Mach 7.9 which represents the position of the main shock, Mach 4 is representing the lower Mach number behaviour and Mach 1 for indicating boundary layer separations.

The progression of the strongest shocks, indicated through the Mach 7.9 contour lines, show clearly that the increased injection values, with a factor of 1.1, are leading to a shock angle increase and that the cowl is missed. The shock angle of the configuration with factor 1.1 is higher than for the other two cases. The higher angle value extends over the complete length of the inlet, starting at the injection surfaces. The same applies for the low Mach number region height, depicted with the Mach 4 contour line, which is larger than the heights of the cases with lower injection total pressures.

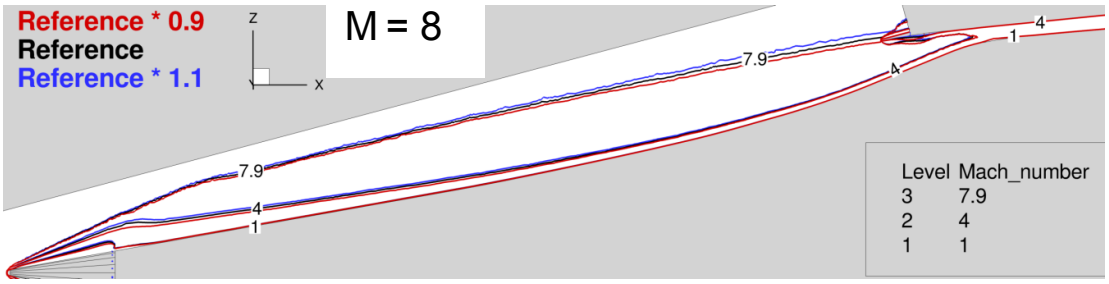

Fig. 7.11: Sensitivity study comparison of three different configurations – overview

Below in Fig. 7.12, a cut-out of Fig. 7.11 is shown with the identical Mach number contour lines showing the cowl area. In it, the progression of the shocks at the cowl and the occurring boundary layer separations can be evaluated. Above the centrebody, the height of the lower Mach number region, depicted through the Mach 4 contour line, differ only slightly from each other. The heights are increasing with increasing injection total pressure and density. However, on the inner cowl side, the boundary layers deviate explicitly from each other and the behaviour is partly contrary to the boundary layer behaviour on the centrebody. In detail, the Mach 4 contour line heights are

decreasing with increasing injection total pressure. In the case with the highest injection total pressure, here depicted as *Reference * 1.1*, the shock is missing the cowl outward of the inlet. Due to this, the mass flow is reduced within the inlet, which also reduces the surface pressure values. The reduction of surface pressure leads to lower boundary layer separation heights, and sizes. As in the optimised "Reference" case, the main shock generated at the centrebody tip is missing the cowl tip also to the inlet outside. In this case, the boundary layer separation is smaller as in the *Reference * 0.9* case but still higher than the *Reference * 1.1* case.

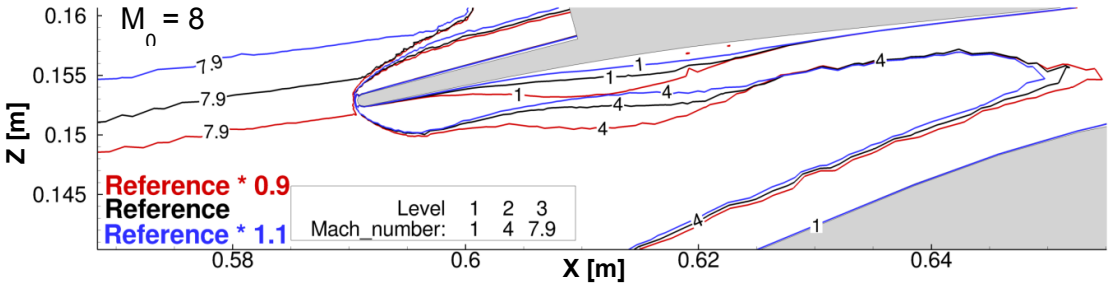

Fig. 7.12: Sensitivity study comparison of three different configurations – enlarged throat area

Fig. 7.11 and Fig. 7.12 show that maximising the averaged mass weighted total pressure recovery does not automatically lead to a maximised mass flow rate, as the second parameter is only close to a maximum when the first is optimised. This shows that optimising an inlet based on the total pressure recovery, the mass flow rate is also almost optimised. However, a trade-off study has to be performed, determining the importance of both parameters when regarding the overall engine performance to decide on which parameter should be prioritised during optimisation.

7.2 Mach 8 Freestream Flow at Mach 6 Inlet at 3° Angle of Attack

In the last section it was proven, using the quasi-three-dimensional simulations that shock angle variation due to mass flow injection is feasible. In this section, asymmetric injection is applied onto the known HRE design at an angle of attack of 3° at a Mach number of 6. Here, asymmetric injection is understood as injection with different mass flows at different angular injection surface positions.

3° angle of attack is chosen as this angle does not lead to any excessive mass flow spillage and it is lower than the cruise maximum angle of attack for other supersonic cruising aircraft systems. For the Mach 3.2 SR-71 Blackbird this was between 4° and 7° at cruise (Anon, 1987) and between 4.5° and 5.5° for the Mach 6 European hypersonic ramjet powered transport system, ATTLAS 2 (Dittrich, 2011). It is unlikely that the engines are fixed at zero relative angle of attack against the mean aerodynamic chord axis as this would cause excessive drag during cruise phase and reduce

its thrust producing capabilities. Rather, the engines are at a small relative angle to the chord axis to optimise the thrust acting direction and to reduce any avoidable drag. Due to the likely presence of a relative angle of attack the chosen three degrees are in a realistic region.

The maximal occurring g-forces at the flown angle of attack are, according to calculations performed for the trajectory of ATTLAS 2, at all times below 1.5 times the acceleration due to the gravity of the Earth and are therefore not harming passengers or cargo (Dittrich, 2011). Therefore, the 3° angle of attack is a safe choice in this aspect, too.

In this section, the identical inlet geometry of Section 7.1, (i.e. optimised for a freestream Mach number of 6), is simulated in Mach 8 freestream flow at an angle of attack (AoA) of 3°. Due to the symmetric freestream flow at 0° AoA, the injection is in Section 7.1 symmetric as well. However, the integrated eight injection segments allow variations in the injection settings for each segment. This means that asymmetric injection is possible and efficiency is investigated in this section at one example configuration.

When an axisymmetric inlet with a geometry optimised for a certain Mach number is at any AoA, the cone shaped shock, generated at the centrebody tip, is missing the cowl to the inlet outward side partially, when below or at the optimised inlet Mach number. Therefore, mass flow is lost to the atmosphere and spillage drag occurs, due to the creation of the shock and the compression of the air, which cannot be used in the thrust producing process. To avoid this spillage drag, an optimised inlet geometry for Mach 6 is analysed at a freestream Mach number of 8 at 3° AoA with asymmetric injection to control the shock position.

In Fig. 7.13 a Mach number line plot is presented, showing the contour lines on the symmetry plane for the identical three Mach number levels as in Section 7.1 for two configurations, without injection and with injection. The injection takes place through the indicated injection surface, which is in contact to the symmetry plane at the bottom side of the figure.

When regarding the shock progression of both cases, the shocks at the lower inlet side, see Fig. 7.15, are further inside of the inlet at the cowl position than the shock at the upper cowl position in Fig. 7.14. These shocks, impinging at the cowl inside, lead to boundary layer separations. As can be seen in Fig. 7.14, the active injection through the lowest injection surface is not influencing the shock wave at the cowl position. The shock progression is only changed for the first two-thirds of the length of the centrebody-tip to cowl-tip distance; therefore, no improvement through the

injection is achieved in terms of the boundary layer reduction, when comparing with the non-injection case.

The injection through the lower surface leads to a small global increase of the shock cone angle. At the lower inlet side, where the mass flow injection takes place, the shock is not increased over the complete inlet length. On the lower cone side, where the injection is active, the changes of the shock angle have only local effects, close to the injection. Thus, they are not influencing the shock angle at the cowl position. Whereas on the top side of the cone, in opposition to the injection, the injection increases the shock angle globally, over the full cone length with a constant angle from the tip to the cowl. In Fig. 7.13, the described constant shock angle increase on the upper inlet side can be clearly seen, when comparing the injection case with the non-injection case. Fig. 7.14 shows the upper inlet cowl area. When comparing the Mach 7.9 contour lines (top and bottom) it is obvious that the flow at the cowl position is influenced by the injection through the lower centrebody tip injection surface. With active injection, the shock wave is not impinging within the inlet as in the non-controlled case, which shows that the angle of the shock cone is increased. Therefore, the separation size of the boundary layer on the inner cowl surface is reduced, but mass flow is lost, too.

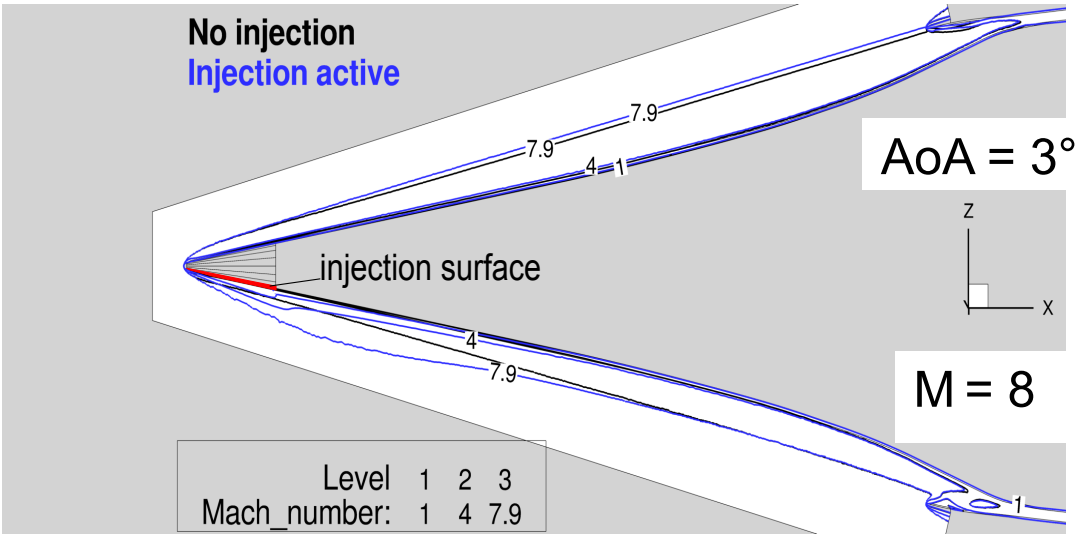

Fig. 7.13: Mach number contour line plot comparing two cases, without and with injection at an inlet at 3° AoA

In Table 7.3, the injection parameters, the resulting averaged mass weighted total pressure recoveries at the throat and the mass flow rates are presented for four different cases: without injection, and with injection through one, three and five injection surfaces. Above, in the contour lines plots of Fig. 7.13 to Fig. 7.15 the configuration with only injection through *surface I* is shown because the inlet performance of this configuration is superior to the others. However, in Table 7.3, the injection total pressures and total recoveries of all investigated cases are shown. When

comparing the captured mass flows and the total pressure recoveries with each other, it is obvious that the injection has no positive effect on the performance criteria. In detail, with increasing activated injection surfaces the captured mass flow rate decreases. The same trend can be regarded for the total pressure recovery, which decreases with increasing injection mass flow rate, too.

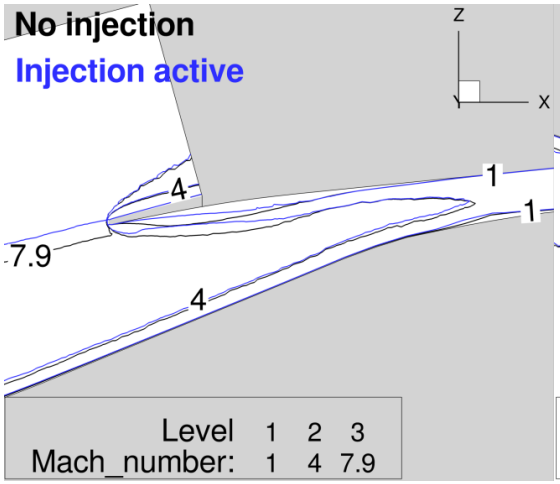

Fig. 7.14: Enlargement of the upper cowl region – comparing two cases, without and with injection at 3° AoA

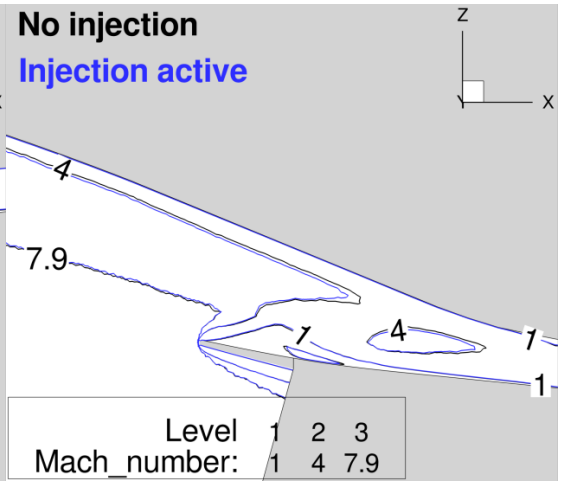

Fig. 7.15: Enlargement of the lower cowl region – comparing two cases, without and with injection at 3° AoA

The injection total pressure is chosen for the individual injection surface to be as high as possible, but ensuring still subsonic inflow. Therefore, the maximum injection Mach number through the injection surfaces is M≈0.95, ensuring maximum shock angle change capability. No further simulations with additional activated injection surfaces are performed, as the negative trend with increasing injection surfaces is noticeable.

Table 7.3: Injection and performance results from asymmetric injection

Case	Unit	no injection active	Injection I active	Injections I - III active	Injections I - V active
$p_{t,freestream}$	[Pa]	3.19E+06	3.19E+06	3.19E+06	3.19E+06
$p_{t,inj,I}$	[Pa]	0	3,000	3,000	3,000
$p_{t,inj,II+III}$	[Pa]	0	0	2,700	2,700
$p_{t,inj,IV+V}$	[Pa]	0	0	0	2,100
$\dot{m}_{inj}$	[kg/s]	0	8.28E-04	1.72E-03	2.53E-03
$\dot{m}_{captured}$	[kg/s]	9.89E-01	9.87E-01	9.84E-01	9.80E-01
$\dot{m}_{inj}/\dot{m}_{captured}$	[-]	0	8.35E-03	1.75E-03	2.58E-03
$\overline{p_{t,throat}}$	[Pa]	1.02E+06	9.97E+05	9.93E+05	9.84E+05
$\frac{\overline{p_{t,throat}}}{p_{t,0}}$	[-]	0.3192	0.3125	0.3112	0.3084

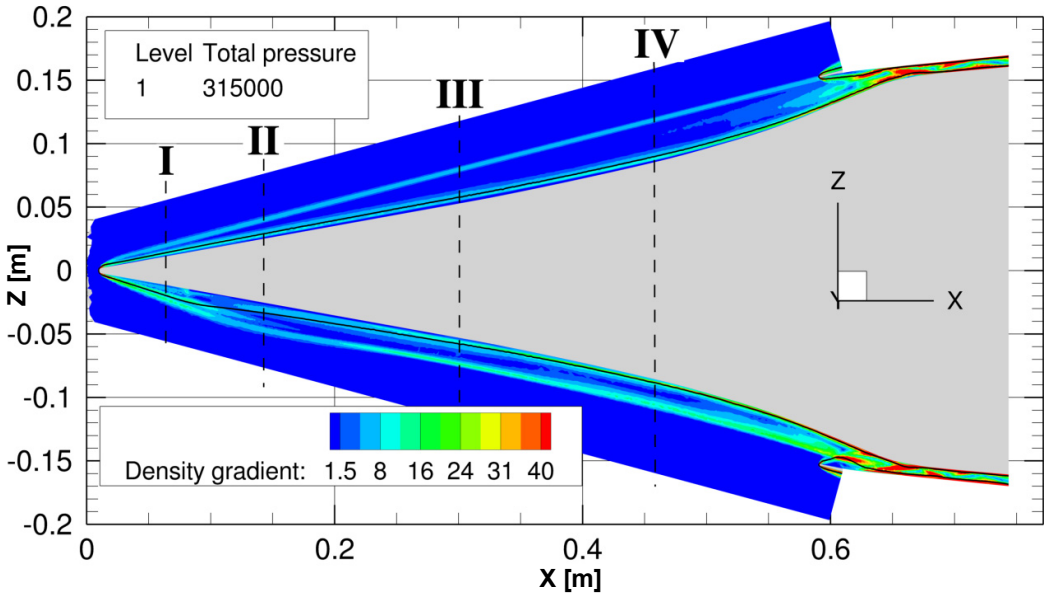

Fig. 7.16: Density gradient contour plot with one total pressure contour line depicting the contact surface; slice extraction positions (see Fig. 7.17) are highlighted

In Fig. 7.17, a density gradient plot with one total pressure contour line of 315,000 Pa is shown. As described in Section 6.2.2, with the total pressure contour line the progression of the contact surface, between the injected and the freestream flow, is illustrated. Due to the angle of attack at which the simulation takes place and the asymmetric injection at the bottom side of the centrebody tip, the contact surface is not symmetric at any X-position. The four slice positions are numbered with the Roman numerals I-IV.

These numbered slices are shown in Fig. 7.17 in the *Y-Z*-plane, depicting the asymmetric contact surface behaviour. In the figure, the Mach number is shown in a contour plot, whereas the total pressure contour line of 315,000 Pa is depicting the rough position of the contact surface.

In slice I and II the contact surface is at the bottom side of the centrebody, significantly further away from the surface than on the upper side. In slice III, the contact

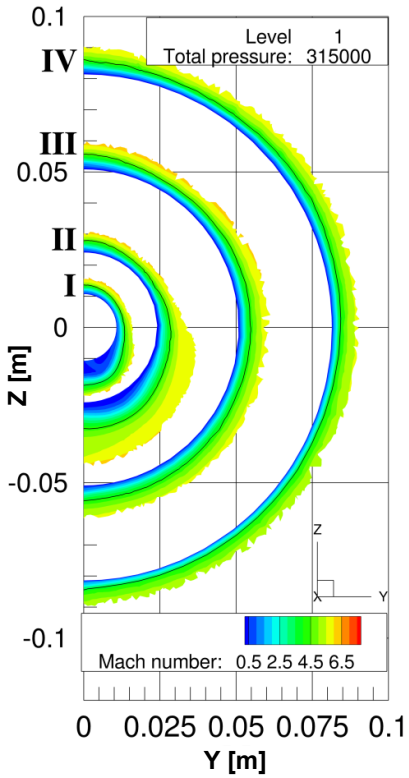

Fig. 7.17: Mach number contour plot with one total pressure contour line of four slices depicting the different progressions of the contact surface

surface progression is nearly symmetrical as its distance to the surface is reduced. Finally, in slice IV the distance at the bottom centrebody side reduced further, leading to a smaller distance between the solid surface and the contact surface at the bottom side than at the lower side. The injection influence can clearly be seen in slices I and II in the low Mach number regions on the bottom cone side. For the other slices, III and IV, which are further downstream of the injection position, the injection has no significant influence on the boundary layer. This shows that the asymmetric injection does not lead to a permanent thickening of the boundary layer as the injection influence reduces continuously with increasing distance from the injector. This leads to the hypothesis that a longer injection area in the *X*-direction would increase the downstream influence area of the injection, with benefits for the shock position at the lower cowl area. When the shock impinges on the lower cowl lip, the separation size would be significantly reduced, leading to lower total pressure losses. However, the realisation of this would go beyond the scope of this research study.

As presented in this section, a positive effect of asymmetric shock angle control could not have been proven in the performed investigation. However, this study shows that injection on the lower injection surface influences the flow and the conical shock angle around the complete inlet. This effect and knowledge can eventually be used for flow control at other positions of an aircraft, but it is not leading to improvements in the regarded flow topology of a hypersonic inlet, at an angle of attack, within this study.

8 Conclusions and Recommendations for Further Work

8.1 Conclusion of the Findings of this Dissertation

Supersonic aircraft are still demanded by the market, even though currently there are no civil supersonic transport aircraft in service. Concorde was a great innovation offering for the first time commercial supersonic passenger flights. However, mainly due to economic reasons, partly caused by a low efficiency, its service was terminated. The inlet efficiency has the biggest influence on the engine and overall performance of aircraft. Therefore, this study was set out to explore possible alternatives of supersonic flow control mechanisms in supersonic engine inlets.
With the classical variable geometry approach, the compression shock and flow topology can be controlled in an efficient way. However, the main downside of this method is the high weight fraction of the variable inlet mechanics. Alternative flow control methods were investigated in this study to improve the inlet efficiency while avoiding variable geometry mechanics and their downsides. Through this, they offer the capability to improve the whole aircraft's performance.

In search of possible supersonic flow control alternatives, a promising concept, which was not investigated further, was found in the literature (Tan et al., 2007) about shock angle increase by mass flow injection at the inlet tip. In that case, the main principle is the increase of the shock angle when the shock, created at the inlet tip, impinges on the inner cowl surface, because of higher freestream Mach numbers than the inlet's geometry optimal Mach number. The shock impingement on the cowl surface inside leads to a strong shock wave/boundary layer interaction, which results in boundary layer separation. This boundary layer separation causes additional losses and has the potential of leading to a blockage of the flow channel, degrading the complete inlet flow. To avoid this, mass flow is injected at the inlet's-tip, which increases the shock angle. This leads to a reduction of the boundary layer separation size and an increase in the total pressure recovery, a performance value in inlet evaluation.

To broaden the understanding of the injection onto the flow and shock topology, several quasi-three-dimensional studies were performed with the DLR TAU-Code flow solver, investigating the injection on a two-ramp axisymmetric geometry and finally on an axisymmetric inlet geometry. For this purpose, two available boundary conditions for the simulation of mass flow extraction and injection in the TAU-Code were validated. For the inlet geometry, the extensively investigated NASA Hypersonic Research Engine inlet was chosen due to the availability of the detailed performance data at various freestream conditions. The influence of the individual injection

parameters onto the inlet performance could be derived and it turned out that best performance could be achieved when injecting with an angle of 45° to the freestream flow direction. Additionally, it was pointed out that the total pressure, with which the mass flow is injected through the injection surface, strongly influences the shock angle change. Furthermore, it could have been pointed out that subsonic injection is more efficient, for shock angle change, than supersonic injection. The preliminary investigation was finalised by a study to determine the optimal injection settings, ensuring that the shock, created at the centrebody tip, impinges on the cowl tip at a freestream flow of Mach 8 at a geometry optimised for Mach 6.

Based on the knowledge obtained, three-dimensional simulations of the identical inlet were performed to verify the quasi-three-dimensional results and allowing simulations at an angle of attack to study the non-symmetrical flow and its effect onto the inlet's performance. The three-dimensional simulations at 0° angle of attack showed comparable results to the quasi-three-dimensional calculations. To ensure the shock angle impinges on the cowl tip and that the total pressure recovery is maximised, 0.9 % of the total captured mass flow rate is injected at the centrebody tip. This leads to an increase in the total pressure recovery of 5.2 %, in comparison with the non-controlled case.

The adjacent conducted parameter sensitivity study showed clearly that further small increases of the shock angle, due to higher injection total pressures, lead to bigger performance losses (which can be understood and seen as the pressure ratio decreases). With increasing shock angle, the shock is not impinging on the cowl tip anymore but misses it to the outside of the inlet. Thus, mass flow is lost to the atmosphere with a dramatic impact on the pressure recovery. A reduction of the shock angle reduces the performance, too, as it leads again to boundary layer separations. However, as long as the boundary layer separation is not causing a blockage of the inlet, a reduction of the shock angle is preferred over an increase.

The last part of this study was the simulation of the already extensively investigated Mach 6 inlet geometry at an angle of attack of 3°. This angle of attack value causes an asymmetric flow topology with a large separation at the lower inner cowl side. Due to the flow asymmetry, the separation size decreases with increasing distance to the lower inlet position. The concept was to control the asymmetric shock progression by asymmetric injection through eight injection surfaces around the centrebody tip. Unfortunately, effective shock angle control was not possible with the given setup. The maximum injection through the lowest injection surface led to a regional shock angle increase. Nevertheless, at a length of two-thirds of the centrebody tip to cowl tip distance, the injection effect was almost unnoticeable on the lower inlet side. The injection was neither leading to lower separation sizes, nor to an increased inlet performance. The performance was not only decreased, but the injection even led to a decrease in the total

pressure recovery. Interestingly, the injection through the lower centrebody surface influenced the flow topology around the complete inlet. It increased the boundary layer thickness and by this the shock angle at every inlet position which is not directly influenced from the injection.

The main novelties of this research are the extensive quasi-three-dimensional and three-dimensional CFD studies, determining the performance gains through injection at one existing inlet geometry. The study shows that it is possible, within certain restrictions, to control compression shock wave angles efficiently. By this, the injection is influencing the flow topology, leading to smaller separation sizes within the inlet and to higher inlet performances above design Mach number, without the need of a variable geometry inlet.

The novelty and the contribution of this work to the research field can be summarised under the following bullet points:

- The comprehensive literature survey is summarising the state-of-the art in flow control methods, acting also as fundament for this thesis.
- The validations of the mass flow extraction and mass flow injection boundary conditions are ensuring their usage in this study and are allowing future reliable CFD simulations with the TAU-Code with these now validated boundary conditions.
- The conducted parameter study, determining the influence and sensitivities of the injection parameters onto the shock angle is the most comprehensive study in this area.
- This study is the first investigation and publication of three-dimensional injection for shock angle change at inlet at an angle of attack.

When shock angle control through mass flow injection is used in real engine applications, the shocks can be controlled by injection instead of variable geometry. This method is less effective in terms of total pressure recovery. However, using symmetric mass flow injection instead of a variable geometry may offer advantages in applications where only a short time a higher flight Mach number than the design inlet Mach number is required. Additional to that, this study is acting as basis for future asymmetric injection studies in which further injection configurations should be investigated. Parts of the gained knowledge of this study about shock angle controlling could be transferred into other flow control studies, like the thrust vector control in rocket engine valves.

With this work, the formulated research objectives were achieved. On the one hand, as effective flow control method, mass flow injection for shock angle control was identified in the literature. On the other hand, this method was investigated and evaluated that it is an alternative flow control method allowing effective and efficient shock angle increases.

8.2 Recommendations for Further Work

Due to the limitations of the applied boundary conditions, the inflow properties had to be controlled in order to control the inflow mass flow rate. For the next research phase, a new boundary condition has to be developed, which allows the exact definition of the injection mass flow rate and the injection flow properties. A modification of an existing or the development of a new injection boundary condition was not feasible in the given period of this study. Therefore, the existing and sufficiently good working boundary conditions were used.

However, with the newly developed boundary condition, a study should be performed, increasing the knowledge about the constraints of injection as flow control method. This comprehensive investigation should have the aim to build up a database leading to a global understanding of the relationship between the shock angle change, the compression ramp angle, the injected mass flow rate and the injection settings, whereas the focus should lie on the injection pressure. Using this database, general valid assumptions and predictions can be formulated, which can be expressed in a set of equations that can be used in future flow control design processes.

This numerical investigation should be performed in an automated way, as a large number of simulations have to be performed to create a comprehensive database. The automation of this labour intensive and computer-time-consuming optimisation research lowers the required labour costs.

Although, a validation of the used numerical tools was carefully performed, the results have to be verified in wind tunnel or flight experiments. In this study, the injector geometry was investigated only marginal; therefore, further research studies should evaluate the effect of the injector size and the injection position.

Finally an all-embracing simulation should be performed. This should include the simulation of a complete inlet, mass flow injection (to increase the shock angle), a normal shock and mass flow extraction (to allocate the required injection mass flow rate and to stabilise the normal shock). This would lead to a concluding comprehensive impression how the mass flow injection flow control mechanism is influencing all relevant inlet performance criteria, like the total pressure recovery, the total pressure distortion, the distortion of the flow and the captured mass flow rate. An automatic optimiser should be used to change the injection settings automatically to find the optimum. With such an optimiser other injection and extraction positions could also be identified which may also lead to an enhancement of the pressure recovery.

Furthermore, a performance analysis between the shock and flow control methods, the mass flow injection and the variable geometry, should be performed. Shock angle increase by injection showed to be effective in the investigated configurations, however, a cost-benefit analysis has to be performed to determine potential gains through lower engine masses. Even a combination of both methods is imaginable to combine the advantages of both.

To confirm the findings, another turbulence model should be used, especially as the SST model has the discussed potential to over-predict the static wall pressure and with it, the boundary layer separation sizes. The *k*-*ε* model should be the first choice as proposed by Tian and Lu (2013) and gives good shock wave and separation point positions, even if Tan et al. (2007) recommended the SST-turbulence model. The *k*-*ε* turbulence model could lead than to a better accordance between the experiment, in Section 6.1.1, and the new performed simulation.

So far, all simulations were performed in steady state, as the numerical effort for time-dependent large eddy, or detached eddy simulations would have gone beyond the means of this study. However, time-dependent simulations are the next logical step to increase the understanding of the working principle of shock angle increase by the injection of mass flow. In detail, the time-dependent simulations capture the behaviour and the sizes of time-dependent vortices in boundary layer separations within the inlet and at the injection position. This would significantly broaden the knowledge and understanding of flow control by mass flow injection.

References

AIAA (1998) *Guide for the Verification and Validation of Computational Fluid Dynamics Simulations [online]*. Report number: AIAA G-077-1998. Reston, US-VA: AIAA. Available from: https://www.aiaa.org/StandardsDetail.aspx?id=3853 [Last accessed 20 March 2015].

Ames Research Staff (1953) *Equations, Tables, and Charts for Compressible Flow [online].* Report number: NACA 1135. NASA: Available from: http://www.grc.nasa.gov/WWW/BGH/Images/naca1135.pdf [Last accessed 20 March 2015].

Anderson, B., Anderson, R., Håkansson, L., Mortensen, M., Sudiyo, R. and Wachem, B. (2012) *Computational Fluid Dynamics for Engineers*. Cambridge: Cambridge University Press.

Anderson, J. D. (1995) *Computational Fluid Dynamics – The Basics with Applications*, Columbus, US-OH: McGraw-Hill Education.

Anderson, J. D. (2004) *Modern Compressible Flow*, 3rd ed. Columbus, US-OH: McGraw-Hill Education.

Anderson, J. D. (2006) *Hypersonic and High-Temperature Gas Dynamics*, 2nd ed. Reston, US-VA: American Institute of Aeronautics and Astronautics, Inc.

Anderson, J. D. (2011) *Fundamentals of Aerodynamics*, 5th ed. Reston, US-OH: McGraw-Hill Education.

Anderson, W.E. and Wong, N.D. (1970) *Experimental Investigation of a Large Scale, Two-Dimensional, Mixed-Compression Inlet System – Performance at Design Conditions, M=3.0.* Report number: NASA TM X-2016. Moffet Field, US-CA: NASA Ames Research Center.

Andren, J., Gao, H., Yano, M., Darmofal, D., Gooch, C. and Wang, Z.J. (2011) A Comparison of Higher-Order Methods on a Set of Canonical Aerodynamics Applications, In: 20th AIAA Computational Fluid Dynamics Conference. Honolulu, Hawaii, 27-30 June 2011. Reston, US-VA: AIAA, pp. 1-13.

Anon (1987) *SR-71A Flight Manual* [online] Available from http://www.sr-71.org/blackbird/manual/ [Last accessed 20 March 2015].

Bangert, L.H., Santman, D.M., Horie, G. and Miller, L.D. (1982) Some Effects of Cruise Speed and Engine Matching on Supersonic Inlet Design, *Journal of Aircraft*, 19 (1), pp 58-64.

Bardina, J.E., Huang, P.G. and Coakley, T.J. (1997) *Turbulence Modeling Validation, Testing, and Development. Report number: NASA TM 110446*. Moffet Field, US-CA: NASA Ames Research Center.

Bogard, D.G. and Thole, K.A. (2006) Gas Turbine Film Cooling. *Journal of Propulsion and Power*, 22 (2), pp. 249-270.

Boon, S. and Hillier, R. (2006) Hypersonic Inlet Flow Analysis at Mach 5, 6, And 7. In: *44th AIAA Aerospace Sciences Meeting and Exhibit*. Reno, US-NV, 9-12 January 2006. London: Imperial College London, pp. 1-12.

Bowditch, D.N. (1973) *Some Design Considerations for Supersonic Cruise Mixed Compression Inlets*. Report number: NASA TM X-71460 Cleveland, US-OH: NASA Lewis Research Center.

Brändle, S. (2011) *In anderthalb Stunden nach New York [German] [In one and a half hours to New York]* [online]. Available from: http://www.stuttgarter-zeitung.de/inhalt.flugschau-in-anderthalb-stunden-nach-new-york.aca7125d-8d73-4082-b2cf-8b6eee907933.html [Last accessed 01 June 2015].

Bräunling, W.J.G. (2009) *Flugzeugtriebwerke [German] [Aeroplane Engines].* 3rd ed. Berlin, Germany: Springer.

Cain, T. (2010) Ramjet Intakes, Report number: AVT-185 RTO AVT/VKI. In: *Lecture Series*, Rhode St. Genèse, Belgium, 13-16 September 2010. NATO Science and Technology Organization, pp. 1-30.

Candel, S. (2004) Concorde and the Future of Supersonic Transport. *Journal of Propulsion and Power.* 20 (1), pp. 59-68.

Curry, M. (2002) *NASA Photo Collection [online].* Available from: http://www.dfrc.nasa.gov/Gallery/Photo/X-15 [Last accessed 20 March 2015]

CentaurSoft (2013) *CENTAUR from CentaurSoft - Mesh (Grid) Generation for CFD and Computational Simulations* [online]. Available from: https://www.centaursoft.com/ [Last accessed 20 March 2015].

DARPA (2010) *Vulcan Phase II - Turbine/Constant Volume Combustion Engine Demonstration Program* [online]. Available from: www.fbo.gov/utils/view?id=2d724e6a4f6a39937 f857ef8f75863 c0 [Accessed 14 March 2012].

Debonis, J.R., Trefny, C.J. and Steffen Jr., C.J. (1999) *Inlet Development for a Rocket Based Combined Cycle, Single Stage o Orbit Vehicle Usind Computational Fluid Dynamics*. Report number: TM-1999-209279. Moffet Field, US-OH: NASA Glenn Research Center.

Dittrich, R. (2010) Digital Microsoft Word and Excel documents were given from Robert Dittrich to Björn Buanga, 14 May.

Dittrich, R. (2011) Attlas flight trajectory Microsoft Excel data sheets were given from Robert Dittrich to Björn Buanga, 20 September.

Dittrich, R., Longo, J.M.A., Carrier, G., Duveau, P., Salah El Din, I. and Thepot, R. (2008) *Multi-Disciplinary Analysis and Optimisation of Hypersonic Transport Aircraft.* In: 6th European Symposium on Aerothermodynamics for Space Vehicles, 3-6 November 2008, Versailles, France, pp. 1-8.

DLR (2011) *User Guide of the DLR TAU-Code Release 2011.2.0.* Braunschweig, Germany : DLR.

DLR (2012) *Technical Documentation of the DLR TAU-Code Release 2012.1.0.* Braunschweig, Germany: DLR.

Dolling, D.S. (2001) *Fifty Years of Shock-Wave/Boundary-Layer Interaction Research: What Next?*, AIAA, 39 (8), pp 1517-1531.

Dujardin, A. Gülhan, A. Longo J.M.A. and Mack, A. (2001). *Numerical/Experimental Investigation of a Wedge-Compression Corner with Gap-Flow under Cold-Hypersonic Gas Conditions*, In: Harris, R.A. (2002) 4th Symposium on Aerothermodynamics for Space Vehicles, Capua, Italy, 14-18 October 2001. ESA, pp. 717-729.

EADS (2011) *EADS presents high-speed transport concept study at Le Bourget* [online]. Available from: www.airbusgroup.com/int/en/news-media/press-releases/Airbus-Group/Financial_Communication/2011/06/20110621_eads_zehst.html [Last accessed 20 March 2015].

ESA (2013) *ESA Test opens way to UK Spaceplane Engine Investment* [online]. Available from: http://www.esa.int/Our_Activities/Technology/ESA_test_opens_way_to_UK_spaceplane_engine_investment [Last accessed 20 March 2015].

Falempin, F. and Kuentzmann, P. (2009) *Ramjet, Scramjet & PDE an Introduction* [online]. Available from: http://www.onera.fr/sites/default/files/ressources_documentaires/cours-exposes-conf/ramjet-scramjet-and-pde-an-introduction.pdf [Last accessed 20 March 2015].

Falempin, F., Goldfeld, M.A., Semenova, Y.V., Starov, A.V. and Timofeev, K.Y. (2008) Experimental study of different control methods for hypersonic air inlets. *Thermophysics and Aeromechanics*, 15 (1), pp.1-9.

Farrukh, S. (2009) *Microjet creation and control of shock waves*, US patent, US2009/0288711 A1.

Fry, R.S. (2004) A Century of Ramjet Propulsion Technology Evolution. *Journal of Propulsion and Power*, 20 (1), pp.27-58.

Galle, M. (1999) *Ein Verfahren zur numerischen Simulation kompressibler, reibungsbehafteter Strömungen auf hybriden Netzen [German] [A method for the numerical simulation of compressible viscous flows on hybrid grids]*. Report number: DLR-FB 99-04. Cologne, Germany: DLR.

Gally, T. and Campbell, D. (2002) Constrained Aerothermodynamic Design of Hypersonic Vehicles, *AIAA Journal*, Reston, US-VA: AIAA, pp. 1-7.

Genias Graphics (2013) *Tecplot 360* [online]. Available from: ftp://ftp.tecplot.com/pub/doc/tecplot/sdk/tpum.pdf [Last accessed 20 March 2015].

Gerhold, T., Hannemann, V. and Schwamborn, D. (1999) *O*n the Validation of the DLR-TAU Code. In: Nitsche, W., Heinemann, H.-J. and Hilbig, R., eds. (1999) *New Results in Numerical and Experimental Fluid Mechanics, Notes on Numerical Fluid Mechanics,* Vol. 72. Wiesbaden, Germany: Vieweg, pp. 426-433.

Gestis Stoffdatenbank [German][Gestis material database] [online]. Available from: http://gestis.itrust.de/nxt/gateway.dll/gestis_de/000000.xml?f=templates$fn=default.htm$vid=gestisdeu:sdbdeu$3.0 [Last accessed 20 March 2015].

Goldsmith, E.L. and Seddon, J. eds. (1993) *Practical Intake Aerodynamic Design*. Oxford, United Kingdom: Blackwell Scientific Publications.

Hannemann, V. (1997) *Numerische Simulation von Stoß-Stoß-Wechselwirkungen unter Berücksichtigung von chemischen und thermischen Nichtgleichgewichtseffekten [German] [Numerical Simulation of shock-shock-interactions under consideration of chemical and thermal non-equilibrium]*. Report number: DLR-1997-07. Cologne, Germany: DLR.

Hannemann, V., Schnieder, M., Reimann, B. and Eitelberg, G. (1999) Bow shock disturbance due to shear layer instability in hypervelocity shock wave interaction. In: *22nd International Symposium on Shock Waves*. London, 18-23 July 1999. London: Imperial College London, pp. 1-9.

Haselbacher, A. and Blazek, J. (1999) Accurate and Efficient Discretization of Navier-Stokes Equations on Mixed Grids. *AIAA Journal.* 38 (11), pp. 2094-2102.

Haws, R.G., Noall, J.S. and Daines, R.L. (2001) Computational investigation of a method to compress air fluidically in supersonic inlets. *Journal of Spacecraft Rockets*. 38 (1), pp. 51-59.

Hermann R. (1956) *Supersonic Inlet Diffusers And Introduction To Internal Aerodynamics.* Minneapolis, US-MO: Minneapolis-Honeywell Regulator Company.

Holden, H.A. and Babinsky, H. (2005) Separated Shock-Boundary-Layer Interaction Control Using Streamwise Slots, *Journal of Aircraft*, 42 (1), pp 166-171.

Ierotheou, C.S., Forsey, C.R. and U. Block (1995) Parallelisation of a novel 3D hybrid structured-unstructured grid CFD production code. In: Hertzberger, B. and Serazzi, G. (1995) *High-Performance Computing and Networking - Lecture Notes in Computer Science.* Vol. 919. Berlin/Heidelberg, Germany: Springer, pp. 831-836.

Kantrowitz, A. and Donaldson, D. (1945) *Preliminary Investigation of Supersonic Diffusers*. Report number: NACA ACR No. L5D20. NASA.

Karl, S. (2009) ITLR Combustion chamber engineering drawing was send by Sebastian Karl to Björn Buanga, 10 December.

Karl, S. (2011) *Numerical Investigation of a Generic Scramjet Configuration* [online]. PhD, Technische Universität Dresden [German] [Dresden University of Technology]. *Available from:* http://nbn-resolving.de/urn:nbn:de:bsz:14-qucosa-68695 [Last accessed 20 March 2015].

Kobayashi, H., Taguchi, H. and Sato, T. (2012) Performance analysis of Mach 5 hypersonic turbojet developed in JAXA, In: *18th AIAA/3AF International Space Planes and Hypersonic Systems and Technologies Conference*. Trours, France, 24-28 September 2012. Reston, US-VA: AIAA, pp. 1-11.

Krause, M. and J. Ballmann (2007). Enhanced Design of a Scramjet Intake Using Two Different RANS Solvers. In: Hannemann, K. ed. (2007) in: *26th International Symposium on Shock Waves*, Göttingen, Germany. 15-20 July 2007, pp. 589-594.

Laitone, E.V. (1955) Limiting Velocity by Momentum Relations for Hydrofoils near the Surface and Airfoils in Near Sonic Flow. In: Naghdi, P.M. ed. (1954) *Proceedings of the Second U.S. National Congress of Applied Mechanics.* New York, US-NY: ASME, pp. 265-273.

Landis, J.A. and Bowman, W.J. (1996) Numerical Study of a Transpiration Cooled Rocket, In: *32nd AIAA, ASME, SAE, and ASEE, Joint Propulsion Conference and Exhibit*, Lake Buena Vista, US-FL, 1-3 July 1996, Reston: US-VA: AIAA, pp. 1-12.

Liebhardt, B., Luetjens, K. and Gollnick, V. (2011) Estimation of the Market Potential for Supersonic Airliners via Analysis of the Global Premium Ticket Market. In: *Aviation Technology, Integration, and Operations Conference 2011*. Virginia Beach, US-VA, 20.-22. Sept. 2011. Reston, US-VA, pp. 1-9.

Loth, E., Geubelle, P., White, S., Tortorelli, D. and Dutton, C. (2000) Smart Mesoflaps for Aeroelastic Transpiration for SBLI Flow Control Air Force Research Laboratory Dayton, US-OH

Mack, A. and Hannemann, V. (2002) *V*alidation of the Unstructured DLR-TAU-Code for Hypersonic Flows. In: *32nd AIAA Fluid Dynamics Conference*. St. Louis, US-MO, 24-27 June 2002. Reston, US-VA: AIAA, pp. 1-9.

Mahoney, J.J. (1990) *Inlets for Supersonic Missiles*. Washington, D.C., US-WA: AIAA.

Mattingly, J.D. (1996) *Elements of Gas Turbine Propulsion*. Singapore, Republic of Singapore: McGraw-Hill Book Company.

Melber, S., Rudnik, R and Ronzheimer, A. (2000) 3D RANS Structured and Unstructured Numerical Simulation in High-Lift Aerodynamics. In: *Proceedings of Workshop on EU-Research on Aerodynamic Engine/Airframe Integration for Transport Aircraft*, Braunschweig, Germany, 26-27 September 2000. Braunschweig, Germany: DLR, pp. 1-13.

Menter, F. (1993) Zonal Two Equation k-ω Turbulence Models for Aerodynamic Flows, In: *24th Fluid Dynamics, Plasmadynamics, and Lasers Conference.* Orlando, US-FL, 6-9 July 1993. Reston, US-VA: AIAA, pp. 1-21.

Miller, D.N. and Catt, J.A. (1995) Conceptual development of fixed-geometry nozzles using fluidic injection for throat area control, In: *31st ASME, SAE, and ASEE, Joint Propulsion Conference and Exhibit*. San Diego, US-CA, 10-12 July 1995. Reston, US-VA: AIAA, pp. 1-14.

Murray, A.L. and Lewis, C.H. (1975) *Supersonic turbulent Boundary-Layer flows with Mass Injection Through Slots and/or porous wall* [online]. Report number: NASA-CR-2587. NASA. Available from: http://ntrs.nasa.gov/archive/nasa/casi.ntrs.nasa.gov/19750022408.pdf [Last accessed 20 March 2015].

Nagashima, T. (2007) *The Effects of Intake Modification on a Ramjet Engine* [online]. Available from: http://www.mame.mu.oz.au/~jpmont/CompressibleFlow/JAP/Ramjet-PaperNagashima.pdf [Accessed 30 March 2009].

NASA (2010) *Dryden Historical Aircraft Photo Collection [online].* Available from: http://www.dfrc.nasa.gov/Gallery/Photo/ [Last accessed 20 March 2015].

Nichols, R.H. (2008) *Turbulence models and their application to complex flows (Rev.4.01) [online].* Available from: http://people.nas.nasa.gov/~pulliam/Turbulence/Turbulence_Guide_v4.01.pdf [Last accessed 20 March 2014].

Nowicki, M. (2004) *The Space Shuttle and Its Replacement.* Available from: http://www.csa.com/discoveryguides/newshuttle/overview.php [Accessed 14 March 2012].

Oertel jr., H. and Laurien, E. (2003) *Numerische Strömungsmechanik [German] [Numerical fluid dynamics].* 2nd ed. Braunschweig/Wiesbaden: Friedr. Vieweg & Sohn Verlagsgesellschaft mbH.

Oertel jr., H., Böhle, M., Ehrhard, P., Etling, D., Müller, U., Sreenicasan, K. R. and Warnatz, J., (2008) *Prandtl - Führer durch die Strömungslehre: Grundlagen und Phänomene [German][Prandtl – Guide through fluid mechanics]. 12th ed. Wiesbaden: Vieweg + Teubner Verlag.*

Oswatitsch, K. (1947) *Pressure Recovery for Missiles with Reaction Propulsion at High Supersonic Speed – The Efficiency of Supersonic Diffusers*. Report number: NACA TM-1140. Langley Field, US-VA: Langley Memorial Aeronautical Laboratory.

Park, I.-O., Ananthkrishnan, N., Tahk, M.-J., Vineeth, C.R. and Gupta, N.K. (2011) Low-Order Model for Buzz Oscillations in the Intake of a Ramjet Engine. *Journal of Propulsion and Power*, 27 (2), pp.503-506.

Pearson, L.W. and Jilly, L.F. (1969) *Hypersonic Research Engine Project. Phase 2A: Inlet Program Final Technical Data Report* [online]. Report number: NACA-CR-66797. NASA. Available from: https://ia700507.us.archive.org/16/items/nasa_techdoc_19760065953/19760065953.pdf [Last accessed 20 March 2015]

Petit, J.-P., Geffray, J. and David, F. (2009) MHD hypersonic flow control for aerospace applications. In: *16th AIAA/DLR/DGLR International Space Planes and Hypersonic Systems and Technologies Conference.* Bremen, Germany, 20-22 October 2009. Reston, US-VA: AIAA, pp. 1-19.

Ran, H. and Mavris, D. (2005) Preliminary Design of a 2d Supersonic Inlet to Maximize Total Pressure Recovery. In: *AIAA 5th Aviation, Technology, Integration, and Operations Conference.* Arlington, US-VA, 26–28 September 2005. Reston, US-VA: AIAA, pp. 1-11.

Reaction Engines, Ltd. (2011) *Reaction Engines LTD – Space Propulsion Systems* [online]. http://www.reactionengines.co.uk [Accessed 29 June 2011].

Saunders, J.D., Slater, J.W., Dippold, V. and Lee, J. (2008) *Inlet Mode Transition Screening Test for a Turbine-Based Combined-Cycle Propulsion System*., Cleveland, US-OH: NASA Glenn Research Center.

Schindel, L. and Driftmyer, R. (1992) Surface Cooling by Transpiration of a Freezing Liquid, *Journal of Thermodynamics*, 6 (1), pp 158-159.

Schulte, D. (2001) *Beeinflussung viscoser Stömungseffekte in Hyperschall-Einläufen [German] [Influencing of Viscous Flow Effects in Hypersonic Inlets]*. Aachen, Germany: Shaker Verlag.

Schulte, D. and Henckels, A. (1996) *Studie zur Anordnung der Absaugung bei stoßinduzierter Ablösung einer Hyperschall Grenzschicht [German] [Study about the Bleed Layout for a Hypersonic Boundary Layer Separation].* Cologne, Germany: DLR.

Schulte, D. Henckels, A. and Schell, I. (1996) Boundary Layer Bleed in Hypersonic Inlets. In: *Contributions to the 10th AG STAB/DGLR Symposium.* Braunschweig, Germany, 11-14 June 1996. Braunschweig, Germany: DLR, pp. 296-303.

Schwamborn, D., Gerhold, T. and Heinrich, R. (2006) The DLR TAU-CODE: Recent Applications in Research and Industry. In: Wesseling, P., Onate, E. and Periaux, J., eds. *European Conference on Computational Fluid Dynamics (ECCOMAS) CFD 2006.* Delft, The Netherlands: TU Delft, pp. 1-25.

Slater, J.W. (2008) *Uncertainty and Error in CFD Simulations [online].* Available from: http://www.grc.nasa.gov/WWW/wind/valid/tutorial/errors.html [Last accessed 20 March 2015].

Slater, J.W. and Saunders, J.D. (2008) *Modeling of Fixed-Exit Porous Bleed System*, Report number: NASA TM-2008-215178. Cleveland, US-OH: NASA Glenn Research Center.

Sorensen N.E. and Smeltzer, D.B. (1968) *Investigation of a Large Scale Mixed-Compression Axisymmetric Inlet System Capable of High Performance at Mach Numbers 0.6 to 3.0.* Report number: NASA TM X-1507. Moffet Field, US-CA: NASA Ames Research Center.

Tan, H.J., Sun S. and Yin Z.L. (2009) Oscillatory Flows of Rectangular Hypersonic Inlet Unstart Caused by Downstream Mass-Flow Choking. *Journal of Propulsion and Power.* 25 (1), pp. 138-147.

Tan, H.J., T., Chen, Z. and Li, G.S. (2007) A new concept and preliminary study of variable hypersonic inlet with fixed geometry based on shockwave control. *Science in China Series E-Technological Sciences.* 50 (5), pp. 644-657.

Tian, C. and Lu, Y. (2013) Turbulence Models of Separated Flow in Shock Wave Thrust Vector Nozzle. *Engineering Applications of Computational Fluid Mechanics.* 7 (2), pp. 182–192.

Versteeg, H.K. and Malalasekera, W. (2007) *An Introduction to Computational Fluid Dynamics*. 2nd ed. Essex: Pearson Education Limited.

Voland, R.T., Auslender, A.H., Smart, M.K., Roudakov, A.S., Semenov, V.L. and Kopchenov, V. (1999) CIAM/NASA Mach 6.5 Scramjet Flight and Groud Test. Orlando, US-FL, In: *9th International Space Planes and Hypersonic Systems and Technologies Conference*, 1-5 November 1999. Reston, US-VA: AIAA, pp.1-9.

Wada, Y. and Liou, M.-S. (1997) An Accurate and Robust Flux Splitting Scheme for Shock and Contact Discontinuities. *SIAM J. Sci. Comput.*, 18(3), pp. 633–657.

Waltrup, P.J., White, M.E. Zarlingo, F. and Gravlin, E.S. (1997) History of Ramjet and Scramjet Propusion Development for U.S. Navy Missiles. *John Hopkins APL Technical Digest*, 18 (2), pp. 234-243.

Wang, X. Jiang, G. and Zhou, C. (2008) Optimisation Design for the Two-Dimensional Contour of the Ramjet Engine Inlet. In: *Asia Simulation Conference 2008 - the 7th International Conference on System Simulation and Scientific Computing*. Chengdu, China, 17-19 October 2008. pp. 1197-1200.

Warwick, G. (2008) *DARPA Lifts the Covers on Vulcan Engine.* Available from: http://www.aviationweek.com/aw/blogs/defense/index.jsp?plckController=Blog&plckBlogPage=BlogViewPost&newspaperUserId=27ec4a53-dcc8-42d0-bd3a-01329aef79a7&plck PostId=Blog%3a27ec4a53-dcc8-42d0-bd3a-01329aef79a7Post%3a6adbffb4-6533-460f-b531-62f7dd64ea61&plckScript=blogScript&plckElementId=blogDest [Accessed 14 March 2012].

Widhalm, M. and Rossow, C.-C. (2002) Improvement of upwind schemes with Least-Square method in the DLR TAU-Code, In: Breitsamter, C., Laschka, B., Heinemann, H.-J. and Hilbig, R., eds.

(2004) *Notes on Numerical Fluid Mechanics and Multidisciplinary Design*, Vol. 87. Munich, Germany: Springer, pp. 398-406.

Wilcox, D.C. (2006) *Turbulence Modeling for CFD*. *3rd ed.* La Canada, US-CA: *DCW Industries.*

Williams, R. G. and Vittal, B.R. (2002) Fluidic Thrust Vectoring and Throat Control Exhaust Nozzle. In: *38th AIAA/ASME/SAE/ASEE Joint Propulsion Conference and Exhibit.* Indianapolis, US-IN, 7-10 July 2002. Reston, US-VA: AIAA, pp. .

Willis, B.P. and Davis, D.0. (1996) *Boundary Layer Development Downstream of a Bleed Mass Flow Removal Region.* In: *32nd AIAA/ASME/SAE/ASEE Joint Propulsion Conference and Exhibit.* Lake Buena Vista, US-FL, 1-3 July 1996. Reston, US-VA: AIAA, pp. 1-16.

Willis, B.P., Davis, D.O. and Hingst, W.R., (1995) *Flowfield Measurements in a Normal-Hole-Bled Oblique Shock Wave and Turbulent Boundary Layer Interaction*. In: 33rd Aerospace Sciences Meeting and Exhibit, Reno, US-NV, 9-12 January 1995. Reston, US-VA: AIAA, pp. 1-16.

Zucker, R.D. and Biblarz, O. (2002) *Fundamentals of Gas Dynamics,* 2nd ed. Hoboken, US-NJ: John Wiley & Sons, Inc.

Zumwalt, G. W. and Tang, H. H. (1963) Mach Number Independence of the Conical Shock Pressure Coefficient. *AIAA Journal – Technical Notes and Comments*. 1 (10). pp. 2389-2391.

Copyright Information